Circuits and Systems
Mekelweg 4,
2628 CD Delft
The Netherlands
http://ens.ewi.tudelft.nl/

CAS-MS-2013-05

M.Sc. Thesis

Imaging of Cracks and Weak Spots in Steel and Aluminium Plate Rolls

J.H.F. van Gemert B.Sc.

Abstract

Because of several - sometimes extreme - complications caused by cracks and weak spots in a metal industry roll, it is of great importance to detect these defects in time. Measurements on rolls with artificial- and natural defects have been performed. An imaging operator is introduced, which uses the measurement data to depict the correct locations of the scatterers in the roll. Even when almost 95% of the original measurement data is discarded, the defects in the roll can still be detected. This thesis shows how these imperfections cause deviations in the eddy current measurement setup and presents how the deviations can be used to locate these defects in the steel. The roll is modeled as a conductive half space after which the inhomogeneous Helmholtz equation will be solved to find the electromagnetic fields inside the steel. Defects are modeled as small spheroids with respect to the wavelength, which makes it possible to find the fields inside these scatterers. Furthermore, an equation is found which relates deviations in receiver signals to the electric- and magnetic fields and contrasts in the roll. The quasi-static approach is used to simplify this equation, after which results are shown for different defects and antenna configurations. Similar outcomes are obtained when the measurement data is compared to the theory.

Imaging of Cracks and Weak Spots in Steel and Aluminium Plate Rolls

Thesis

submitted in partial fulfillment of the
requirements for the degree of

Master of Science

in

Electrical Engineering

by

J.H.F. van Gemert B.Sc.
born in Nijmegen, The Netherlands

This work was performed in:

Circuits and Systems Group
Department of Microelectronics
Faculty of Electrical Engineering, Mathematics and Computer Science
Delft University of Technology

Delft University of Technology

Delft University of Technology
Department of
Microelectronics

The undersigned hereby certify that they have read and recommend to the Faculty of Electrical Engineering, Mathematics and Computer Science for acceptance a thesis entitled **"Imaging of Cracks and Weak Spots in Steel and Aluminium Plate Rolls"** by **J.H.F. van Gemert B.Sc.** in partial fulfillment of the requirements for the degree of **Master of Science**.

Dated: 16th of August 2013

Chairman: _____
Prof. Dr. Ir. A.J. van der Veen

Advisor: _____
Dr. Ir. R.F. Remis

Committee Members: _____
Ir. C.M.J. Van Den Elzen

_____
Dr. Ir. N. V. Budko

Abstract

Because of several - sometimes extreme - complications caused by cracks and weak spots in a metal industry roll, it is of great importance to detect these defects in time. Measurements on rolls with artificial- and natural defects have been performed. An imaging operator is introduced, which uses the measurement data to depict the correct locations of the scatterers in the roll. Even when almost 95% of the original measurement data is discarded, the defects in the roll can still be detected. This thesis shows how these imperfections cause deviations in the eddy current measurement setup and presents how the deviations can be used to locate these defects in the steel. The roll is modeled as a conductive half space after which the inhomogeneous Helmholtz equation will be solved to find the electromagnetic fields inside the steel. Defects are modeled as small spheroids with respect to the wavelength, which makes it possible to find the fields inside these scatterers. Furthermore, an equation is found which relates deviations in receiver signals to the electric- and magnetic fields and contrasts in the roll. The quasi-static approach is used to simplify this equation, after which results are shown for different defects and antenna configurations. Similar outcomes are obtained when the measurement data is compared to the theory.

Acknowledgments

Last year, I decided to go to the Circuits and Systems lunch where the group presented thesis topics. I became enthusiastic when I met Rob Remis sometime later, he got an interesting topic about finding cracks in a roll where I could combine electromagnetics and imaging, exactly the work I was looking for. My interests were not misplaced, I really enjoyed working on this thesis. The work has been hard and challenging, overall it was a great experience.

As my thesis adviser, Rob guided me by writing a great piece of work from scratch. During the work he pushed me in the right direction whenever I got stuck, we even faced some challenges together which really showed his commitment. Also in his off-hours he was committed, I sometimes got an email in the evening where he told me he came up with some idea which might bring us closer to a solution. Therefore, I would like to thank Rob for all his time and effort, it has been very instructive and a great pleasure to work with him.

I also would like to thank the company Lismar who offered me this opportunity. I met some nice colleagues and it has been a pleasure to work with all of them. Especially, I would like to thank my adviser within the company, Elmar van den Elzen. We have had some struggles now and then, as I am theoretically set and he is more practically oriented. However, this challenged me a lot and kept me "rolling". He also provided me with a lot of interesting knowledge and insights regarding the work-field. Another colleague I would like to thank is Sander Mul, he has been supportive and helpful during my presence.

I also would like to express my gratitude to my friends and family who showed interest and accepted my new time arrangement. I thank my father Marijn, he reviewed my work and had been thinking along from the start, he made me really think about what I was doing by asking a lot of questions.

My final gratitude is expressed to Bonny my girlfriend. She has been supportive and committed along the way, and made sure I was distracted enough whenever I needed it. Problems had been solved as she made me look to them from a different perspective. We worked really hard together, as she was graduating herself, which has been a great pleasure.

Jeroen van Gemert
Delft, The Netherlands
16th of August 2013

Contents

Chapter 1

Introduction and survey

The production of metal sheets and plates is a great part of the metal industry to which large companies such as ArcelorMittal and Tata Steel are committed. Although there are many ways to create such sheets and plates, the concept is the same. Thick aluminium and steel plates are put through a pair of rotating rolls, the distance between these rolls determines the desired thickness of the plate. Each roll experiences a great repetitive amount of force during this process and thus it becomes fatigued over time. As a consequence, cracks and weak spots develop at and underneath the surface of the roll. These defects in the material are undesirable as they lead to multiple risks. Such a crack tends to grow due to the great forces acting on it and eventually impairs the roll to a certain extent after which pieces of the roll spall and burst out due to high internal stresses (see Figure 1.1). At such times safety can no longer be guaranteed for the environment. In addition, a roll is very valuable and therefore any impairment will cost an extensive amount of money. If a defect is found in time, the roll can be repaired using grinding technologies which then eliminates the above mentioned risks. Because money, and especially safety, are very important, it is a serious business to find the defects in the roll in time.

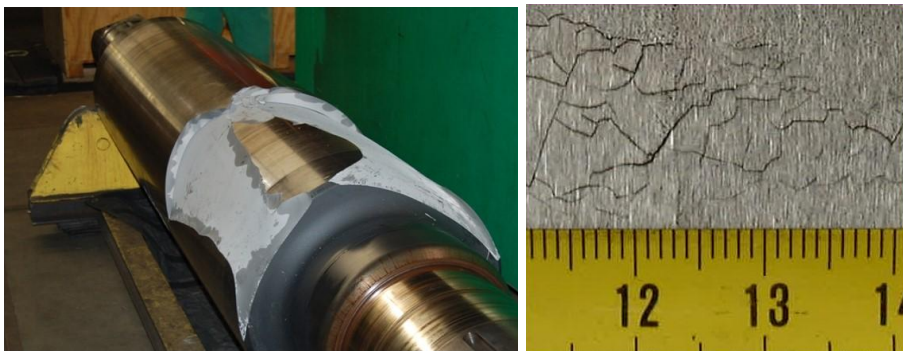

(a) (b)

Figure 1.1: A big piece is spalled from the roll (a) and some cracks in a roll from nearby are shown (b).

Lismar BV is a company which is specialized in finding such defects and they develop complete products for their customers in the metal industry to detect and remove these defects. Using eddy current and ultrasonic inspection as separate methods, they are able to map imperfections in the roll.

This thesis focuses on the first technique Lismar uses, namely, eddy currents. The developed system works, but the exact physical processes behind it are not completely understood. Therefore, the current system cannot be used optimally to obtain all the information from the measured data. Lismar plans on improving the signal processing of their system by the use of additional knowledge on the underlying physical processes. Such an improvement is desirable to find smaller defects (cracks) and to improve defect classification and defect sizing. Furthermore, Lismar would like to scan a roll as fast as possible without losing any valuable information. In order to improve the signal processing and therefore the system, a scientific foundation of the underlying processes is necessary. This leads to the following research proposal:

Develop a scientific model which describes how a roll with possible defects causes deviations in the received signals in the Lismar measurement system, and is employed such that it is applicable in practice to detect and display small defects.

This model will give a good electromagnetic foundation for the measurement system of Lismar. In addition, it will provide insights in the physical processes that take place within a roll and the defects. Therefore, it can be used to optimize the existing system. Furthermore, received signals from a measurement will be used to find the locations of the imperfections in a roll by using an imaging method.

The remainder of this thesis is as follows. Chapter 2 provides background information regarding eddy current testing, defects, and the configuration used by Lismar. In Chapter 3, a model is derived which explains how received signals deviate due to contrast sources. The application of the model is presented in Chapter 4 in which also an equation is derived which shows how defects disturb eddy currents. In order to find the defects in the roll, an imaging operator is derived in Chapter 5. This operator is applied to real measurements performed on two different rolls in Chapter 6, where theory derived in previous chapters is compared and applied. Finally, conclusions can be found in Chapter 7.

Chapter 2

Background

This chapter discusses the process of rolling and in particular the origin of defects in a roll. Material properties of the roll and existing research with regard to eddy current testing are mentioned, from which some useful publications are used throughout this thesis. Finally, the measurement setup from Lismar is discussed, which also provides the constraints for the model that is derived in this thesis.

2.1 Properties and origin of defects in a roll

The process of rolling can be divided into two main categories: hot rolling and cold rolling. This is a large difference as the former works with metal temperatures above the recrystallization temperature and the latter with temperatures beneath this point. Recrystallization is used to repair deformed crystals which arise in the rolling process. This recrystallization has an effect on the metal characteristics as it reduces in both strength and hardness [9], which makes it less fragile. Cold rolling does not repair deformed crystals and has an exact opposite effect on the metal characteristics; an increase in strength and hardness.

As long as the roll is intact and of good quality, the rolling process will be optimal and safe. However, there are some factors which might impair such rolls and therefore affect the quality and the safety. Since the rolls endure a lot of pressure (over 1000 MPa) due to the force acting on it [6], the shell is made from a strong material such as hardened steel.

The largest force of the roll acts in a plane tangential to the metal plate and due to the rotation of the roll the material becomes fatigued over time. As a consequence, small cracks appear and grow further due this repetitive pressure. Especially for hot rolling there is an additional factor which impairs the roll. As the temperature of the metal plates are usually above 1000 degrees Celsius during rolling [8], the roll itself tends to warm up quickly. This is undesirable because the roll loses its strength and therefore the roll is cooled with water. The downside of this cooling is the continuously warming up and cooling down which leads to thermal weakness. This thermal weakness causes fine cracks. In addition, water causes severe damage to the surface of the roll because of corrosion [5].

The last form of defects are in the form of weak spots and are most likely

Table 2.1: Characteristic properties of the roll

ε_r	relative permittivity [12]	1 [no unit]
μ_r	relative permeability	1-100 [no unit]
σ	conductivity [11]	$10^6 - 10^7 [\frac{1}{(\Omega m)}]$

caused by incidents during rolling. If, for example, a metal plate gets stuck in the machine, it damages the steel due to the abrupt concentrated force. This weakens the steel and cracks appear at and beneath the surface.

Electromagnetic fields are very sensitive to the material properties of a steel roll. It is therefore important to list these properties, which is done in Table 2.1. In general, two currents are distinguished. Namely, conduction currents (related to the conductivity) and displacement currents (related to the permittivity). For low frequencies, the former currents dominate and the latter currents can be ignored. Permeability is a measure of how easily a magnetic field can be formed in a material. This property is hard to determine and is therefore not a well-known characteristic.

2.2 Eddy current testing

In a wide range of applications, nondestructive testing (NDT) is of great importance. Under NDT conditions, certain objects are tested without breaking it, i.e. testing from outside the object. One could think of testing the quality of pipelines located under the ground, mapping parts of a human body with the use of MRI, inspecting airplanes for small cracks, or in this case finding cracks or weak spots in a roll.

There are multiple methods that can be used for NDT, the method chosen depends on the specific object to be tested. The commonly used ones for the application of finding defects in a conductive metal plate are ultrasonic- and eddy current testing. These methods have a thing in common, namely, it is possible to find cracks in both the surface and the subsurface of the plate. In this thesis we will only focus on eddy current testing.

Eddy current testing originates over 50 years ago [14]. A sinusoidal current

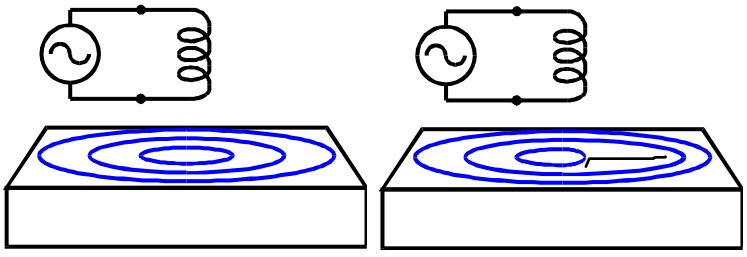

(a) (b)

Figure 2.1: Simplified sketch of how a coil above a conductive plate induces eddy currents (a) and how defects cause these currents to deviate (b) [13].

drives the coil which creates an electromagnetic field that induces eddy currents inside the object. These currents, as the name reveals, run in closed circles and are depicted in Figure 2.1a in simple form. The induced currents produce their own secondary EM-field which is picked up by the receive antenna. As soon as there is a defect in the material, the induced currents will flow somewhat differently (see Figure 2.1b) and consequently, radiate a different secondary field. These differences are found in deviations in the receiver's coil impedance in the form of resistance- and reactance fluctuations. Due to these two parts, both a phase and an amplitude can be obtained during a measurement and this information can be used to reveal information about the defect.

Because of the sinusoidal current, the fields can be derived in the frequency domain as is done in [15], where two different NDT setups are discussed. In the first setup, a coil above a conducting half space is considered, while in the second being a coil surrounding a tube is analyzed. Impedance changes are found for a small spherical defect which differs in conductivity from the object it is in. This has been extended for a setup of multiple coils and multiple cylindrical conductors [16]. Such a conducting half space has also been derived in the geophysics [4], where spatial Fourier transforms are applied to simplify calculations. However, only the space between the source in vacuum and the conducting half space is derived and not the field inside the conductor.

The impedance change due to a crack has been evaluated in several studies [17, 18, 19]. However, these studies do not provide a clear relation between the orientation of the crack and the change in impedance. Furthermore, the use of multiple antennas in a measurement setup is not incorporated. These multiple antennas are studied [24], by introducing a sensitivity function which connects these different antennas. However the crack is modeled as a sphere and is therefore orientation independent. Based on the same principle, multiple frequencies can be used instead of a single one [7]. In this case, more information is obtained about the imperfections and unwanted signals can be filtered out more easily [21].

Around the seventies, eddy current testing has been extended to the pulsed eddy current technique. A pulse has the advantage over a continuous wave as it contains more frequencies, i.e. a broader bandwidth. This implies that there is potentially more information available [20]. These pulses also contain more peak power than a continuous wave which means that with the same amount of energy one can also find defects that lie deeper inside the metal. In addition, with a pulse driven coil the electromagnetic fields decay over time, as does the secondary field. This decay can be studied by sending a pulse and after this transmission the receiver records only the secondary field induced by the object. This data provides additional information about the object, better approximations can be found for the dimensions and depth of defects. This is a rather new research field [22, 23] and more complicated since both time- and frequency-domain field analysis must be carrier out.

2.3 Configuration used by Lismar

This section discusses the measurement setup of Lismar which also leads to some constraints of the model. Due to confidential information, only the necessary parts of the setup are presented which are needed throughout this work.

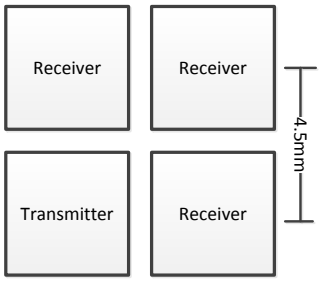

Figure 2.2: The antenna array used by Lismar consists of four square loop-antennas. The midpoints of the vertical- and horizontal aligned antennas are seperated 4.5 mm.

Lismar Engineering is continuously working on new and better equipment. Their newest system is called LRI which combines ultrasonic and eddy current measurements. This system is based on the same principles as the system VENDT, which has been a project by Lismar and TNO. Since both systems are built on the same concept, the VENDT system will be used as guideline for this work [25, 26].

This eddy current system is based on the multiple frequency method as described in the previous section. The measurement setup scans the metal with antennas from a 0.5-1 mm height, while moving over the length of the rotating roll. For this measurement, an array of antennas is used which has four square loop-antennas (depicted in Figure 2.2). One of the loops acts as a transmitter and a receiver (monostatic) while the remaining ones act as receivers.

The measurement array is connected to a differential bridge [10]. This bridge is used to find variations in potential over the antennas as these differences hold information about the defect. Without such a bridge, the absolute potential over an antenna from the measurement array is measured. This potential has some offset which makes it harder to find differences. The function of the bridge is to steer the offset of the antennas to zero, after which only the variations in potential are measured.

An FPGA and a digital-to-analog converter are used to transmit a signal. Every desired pulse or sequence of pulses can be modulated and send to the transmitter. All four outputs of the bridges are directed to an amplifier and this amplifier is connected to a 6-channel analog-to-digital converter. The sample frequency of this ADC is set to 10 MHz, which implies that frequencies up to 5 MHz can be found according to the Nyquist frequency. After the ADC, the signal is send towards the FPGA again which allows up to six demodulation-sequences per channel, such as a single frequency. Hereafter the final step is performed, namely, processing the data.

Chapter 3

Development of the model

The main goal of this thesis is to find more information about the defects in a roll. To this end, it is important to understand the underlying physical principles. Starting point is the measurement setup depicted in Figure 3.1. Here, the rectangle represents the roll containing a crack at the left-hand side. Above the roll two loop-antennas are located, one acts as a transmitter and the other one as a receiver.

The basic idea of finding cracks and weak spots in a roll is quite simple. The antenna pair scans over the roll from one end to the other. The transmitter continuously transmits an electromagnetic wave towards the roll. This wave interacts with the roll as it induces currents in the conductive material. These currents produce an electromagnetic wave which is picked up by the receiver. In case there is no crack present, i.e. a clean roll, the received signal will be the same at any point during the scan. When there is a flaw present, the roll radiates slightly different than before and consequently the antenna will receive a somewhat different signal. These differences contain information about the specific flaw, the difficulty lies in the interpretation of these deviations.

To translate these deviations in the received signal to valuable information, it is important to understand how the received signal comes into being. For example, what physics take place between the transmitter, the roll and the receiver? For this purpose, a theoretical model is developed which gives insight into this process. Having this model available, it can be used to translate the measured differences into useful information about the defects.

Within this chapter there will first be an elaboration on the mathematical notation which is used throughout this thesis. In Section 3.2, the electromagnetic fields are derived which are needed to find the difference in the received signal due to a flaw in the roll. Then, in Section 3.3, an expression is found which expresses these variations in the receive antenna as function of the derived fields, and as function of the geometric- and material properties of the defect. Its limitations are discussed at the end of this chapter.

3.1 Notation

Before the theory is discussed, first some elaboration on the notation and the use of mathematical operations throughout this chapter.

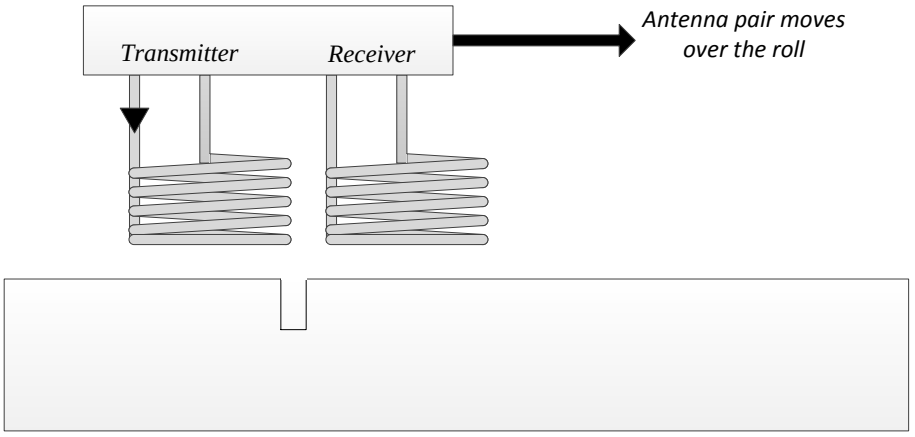

Figure 3.1: Measurement setup in its simplest form. A roll with a crack along with a transmitting and receiving antenna.

To specify position, a Cartesian coordinate system is used with unit vectors $\mathbf{i}_x$, $\mathbf{i}_y$ and $\mathbf{i}_z$, which form a right-handed system. The position vector is denoted as $\mathbf{x} = x\mathbf{i}_x + y\mathbf{i}_y + z\mathbf{i}_z$ and ∂_i denotes differentiation with respect to the ith coordinate ($i = x, y, z$). Furthermore, the nabla operator is given by

$$\nabla = \mathbf{i}_\mathrm{x}\partial_x + \mathbf{i}_\mathrm{y}\partial_y + \mathbf{i}_\mathrm{z}\partial_z,$$

and ∂_t denotes differentiation with respect to the time.

3.2 Electromagnetic fields

The purpose of this section is to find expressions for the electromagnetic fields that are present in case there is a roll with a possible defect. To this end, the measurement setup depicted in Figure 3.1 is built from scratch. We start simple and then rebuild the configuration to arrive at the original setup again.

Specifically, first we consider a source located in vacuum and we determine the resulting fields (see Figure 3.2 left). We refer to this field as the incident electromagnetic field. Second, we include the roll and place it beneath the source as indicated in Figure 3.2 (middle). The roll is characterized by a conductivity σ^{roll}, a permittivity $\varepsilon^{\mathrm{roll}}$, and a permeability μ^{roll}. The dimensions of the roll are finite but large with respect to the wavelength. The resulting field at any point in space is called the background electromagnetic field. Finally, to arrive at the measurement setup of interest, we include a possible defect to the latter setup. A loop antenna placed above a roll containing a possible crack is shown on the right of Figure 3.2. The medium parameters of the defects are given by the conductivity σ^{d}, the permittivity ε^{d}, and the permeability μ^{d} and the electromagnetic field in this configuration is called the total electromagnetic field.

In this section, the three cases of interest are treated separately, starting with a single source in vacuum.

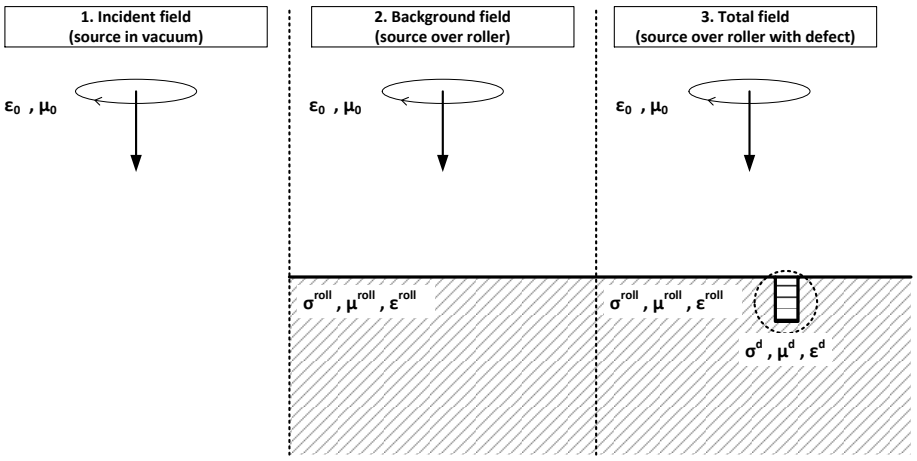

Figure 3.2: A loop antenna is placed in vacuum (left) and a loop antenna is placed above a roll of finite dimensions (middle). A loop antenna placed above a roll containing a possible defect is shown on the right.

3.2.1 The incident electromagnetic field

The first step is to place a loop-antenna in vacuum. In order to find expressions for the electromagnetic fields, the Maxwell equations need to be solved. In a vacuum domain, these equations are given by

$$-\nabla \times \mathbf{H}(\mathbf{x},t) + \varepsilon_0 \partial_t \mathbf{E}(\mathbf{x},t) = -\mathbf{J}(\mathbf{x},t), \tag{3.1}$$

and

$$\nabla \times \mathbf{E}(\mathbf{x},t) + \mu_0 \partial_t \mathbf{H}(\mathbf{x},t) = -\mathbf{K}(\mathbf{x},t). \tag{3.2}$$

Here,

$\mathbf{E}$	is the electric field strength [V/m],
$\mathbf{H}$	is the magnetic field strength [A/m],
$\mathbf{J}$	is the external electric current density [A/m^2],
$\mathbf{K}$	is the external magnetic current density [V/m^2],
$\mu_0 = 4\pi \times 10^{-7}$	is the magnetic permeability vacuum [H/m],

and

$\varepsilon_0 = \frac{1}{\mu_0 c_0^2}$	is the dielectric permittivity vacuum [F/m].

The external current densities are defined on a bounded source domain $\mathbb{D}$ and start to act at the time instant $t = 0$.

To solve Maxwell's equations (3.1) and (3.2) for the fields, we subject these equations to a one-sided Laplace transform with respect to time and a Fourier transform with respect to space.

For a wave field component $f(\mathbf{x},t)$ that is causally related to the source, the one-sided Laplace transform is defined as

$$\hat{f}(\mathbf{x},s) = \int_{t=0}^{\infty} f(\mathbf{x},t)e^{-st}\mathrm{d}t \qquad \text{for } \mathrm{Re}(s) > s_0,$$

and $\hat{f}$ is an analytic function of s in the the right-half plane $\mathrm{Re}(s) > s_0$.

The inverse Laplace transform is given by

$$f(\mathbf{x},t) = \frac{1}{2\pi i}\int_{s_0-i\infty}^{s_0+i\infty} \hat{f}(\mathbf{x},s)e^{st}\mathrm{d}s \qquad \text{for all } t,$$

and the integral on the right-hand side (the so-called Bromwich integral) automatically yields the value zero for $t < 0$.

Finally, the spatial Fourier transform of $\hat{f}(\mathbf{x},s)$ is defined as

$$\tilde{f}(\mathbf{k},s) = \int_{\mathbf{x}\in\mathbb{R}^3} \hat{f}(\mathbf{x},s)e^{-i\mathbf{k}\cdot\mathbf{x}}\mathrm{d}V, \tag{3.3}$$

while the inverse spatial Fourier transform is given by

$$\hat{f}(\mathbf{x},s) = \frac{1}{(2\pi)^3}\int_{\mathbf{k}\in\mathbb{R}^3} \tilde{f}(\mathbf{k},s)e^{i\mathbf{k}\cdot\mathbf{x}}\mathrm{d}V. \tag{3.4}$$

Applying now the temporal Laplace and spatial Fourier transform to Eqs. (3.1) and (3.2) and using the transformation rules

$$\partial_t \xrightarrow{\mathfrak{L}} s \qquad \text{and} \qquad \nabla \xrightarrow{\mathfrak{F}} i\mathbf{k},$$

we obtain

$$-i\mathbf{k}\times\tilde{\mathbf{H}}(\mathbf{k},s) + \eta_0\tilde{\mathbf{E}}(\mathbf{k},s) = -\tilde{\mathbf{J}}(\mathbf{k},s), \tag{3.5}$$

and

$$i\mathbf{k}\times\tilde{\mathbf{E}}(\mathbf{k},s) + \zeta_0\tilde{\mathbf{H}}(\mathbf{k},s) = -\tilde{\mathbf{K}}(\mathbf{k},s), \tag{3.6}$$

where $\eta_0 = s\varepsilon_0$ and $\zeta_0 = s\mu_0$. These equations can now be solved in a fairly straightforward manner (see Appendix A or e.g. [2]). The notation that we use and Eqs. (3.7)-(3.15) are cited from [1]. We then arrive at

$$\tilde{\mathbf{E}}(\mathbf{k},s) = -\left(\zeta_0\mathbb{I} + \frac{1}{\eta_0}\mathbf{k}\mathbf{k}^T\right)\tilde{\mathbf{A}}(\mathbf{k},s) - i\mathbf{k}\times\tilde{\mathbf{F}}(\mathbf{k},s), \tag{3.7}$$

and

$$\tilde{\mathbf{H}}(\mathbf{k},s) = -\left(\eta_0\mathbb{I} + \frac{1}{\zeta_0}\mathbf{k}\mathbf{k}^T\right)\tilde{\mathbf{F}}(\mathbf{k},s) + i\mathbf{k}\times\tilde{\mathbf{A}}(\mathbf{k},s), \tag{3.8}$$

where $\tilde{\mathbf{A}}$ and $\tilde{\mathbf{F}}$ are the so-called spectral domain electric and magnetic vector-potentials given by

$$\tilde{\mathbf{A}} = \tilde{G}\tilde{\mathbf{J}} \qquad \text{and} \qquad \tilde{\mathbf{F}} = \tilde{G}\tilde{\mathbf{K}}, \tag{3.9}$$

and

$$\tilde{G} = \frac{1}{\mathbf{k}^T\mathbf{k} + \gamma_0^2} \quad \text{with} \qquad \gamma_0 = \frac{s}{c_0} \tag{3.10}$$

is the spectral domain scalar Green's function.

Applying an inverse spatial Fourier transform to Eqs. (3.7) and (3.8), we obtain

$$\hat{\mathbf{E}}(\mathbf{x}, s) = -\zeta_0\hat{\mathbf{A}}(\mathbf{x}, s) + \frac{1}{\eta_0}\nabla\left(\nabla\cdot\hat{\mathbf{A}}(\mathbf{x}, s)\right) - \nabla\times\hat{\mathbf{F}}(\mathbf{x}, s), \tag{3.11}$$

and

$$\hat{\mathbf{H}}(\mathbf{x}, s) = -\eta_0\hat{\mathbf{F}}(\mathbf{x}, s) + \frac{1}{\zeta_0}\nabla\left(\nabla\cdot\hat{\mathbf{F}}(\mathbf{x}, s)\right) + \nabla\times\hat{\mathbf{A}}(\mathbf{x}, s), \tag{3.12}$$

where the frequency-domain vector potentials are given by

$$\hat{\mathbf{A}}(\mathbf{x}, s) = \int\limits_{\mathbf{x}'\in\mathbb{D}^3} \hat{G}(\mathbf{x}-\mathbf{x}')\hat{\mathbf{J}}(\mathbf{x}, s)\mathrm{d}V,$$

and

$$\hat{\mathbf{F}}(\mathbf{x}, s) = \int\limits_{\mathbf{x}'\in\mathbb{D}^3} \hat{G}(\mathbf{x}-\mathbf{x}')\hat{\mathbf{K}}(\mathbf{x}, s)\mathrm{d}V.$$

In the above expressions, $\hat{G}$ is the s-domain scalar Green's function given by

$$\hat{G}(\mathbf{x}, s) = \frac{e^{-\gamma_0|\mathbf{x}|}}{4\pi|\mathbf{x}|}. \tag{3.13}$$

Finally, carrying out all differentiations in Eqs. (3.11) and (3.12), we arrive at

$$\begin{aligned}
\hat{\mathbf{E}}(\mathbf{x}, s) = &\int\limits_{\mathbf{x}'\in\mathbb{D}} \frac{e^{-\gamma_0|\mathbf{x}-\mathbf{x}'|}}{4\pi|\mathbf{x}-\mathbf{x}'|^3}(3\mathbb{Q}-\mathbb{I})\frac{1}{\eta_0}\ \hat{\mathbf{J}}(\mathbf{x}', s)\mathrm{d}V \\
&+ \int\limits_{\mathbf{x}'\in\mathbb{D}} \frac{e^{-\gamma_0|\mathbf{x}-\mathbf{x}'|}}{4\pi|\mathbf{x}-\mathbf{x}'|^2}\left[(3\mathbb{Q}-\mathbb{I})\frac{\gamma_0}{\eta_0}\hat{\mathbf{J}}(\mathbf{x}', s) + \boldsymbol{\Theta}\times\hat{\mathbf{K}}(\mathbf{x}', s)\right]\mathrm{d}V \\
&+ \int\limits_{\mathbf{x}'\in\mathbb{D}} \frac{e^{-\gamma_0|\mathbf{x}-\mathbf{x}'|}}{4\pi|\mathbf{x}-\mathbf{x}'|}\left[(3\mathbb{Q}-\mathbb{I})\frac{\gamma_0^2}{\eta_0}\hat{\mathbf{J}}(\mathbf{x}', s) + \gamma_0\boldsymbol{\Theta}\times\hat{\mathbf{K}}(\mathbf{x}', s)\right]\mathrm{d}V
\end{aligned} \tag{3.14}$$

and

$$\hat{\mathbf{H}}(\mathbf{x},s) = \int\limits_{\mathbf{x}'\in\mathbb{D}} \frac{e^{-\gamma_0|\mathbf{x}-\mathbf{x}'|}}{4\pi|\mathbf{x}-\mathbf{x}'|^3}(3\mathbb{Q}-\mathbb{I})\frac{1}{\zeta_0}\ \hat{\mathbf{K}}(\mathbf{x}',s)\mathrm{d}V + \int\limits_{\mathbf{x}'\in\mathbb{D}} \frac{e^{-\gamma_0|\mathbf{x}-\mathbf{x}'|}}{4\pi|\mathbf{x}-\mathbf{x}'|^2}\left[(3\mathbb{Q}-\mathbb{I})\frac{\gamma_0}{\zeta_0}\hat{\mathbf{K}}(\mathbf{x}',s) - \boldsymbol{\Theta}\times\hat{\mathbf{J}}(\mathbf{x}',s)\right]\mathrm{d}V + \int\limits_{\mathbf{x}'\in\mathbb{D}} \frac{e^{-\gamma_0|\mathbf{x}-\mathbf{x}'|}}{4\pi|\mathbf{x}-\mathbf{x}'|}\left[(3\mathbb{Q}-\mathbb{I})\frac{\gamma_0^2}{\zeta_0}\hat{\mathbf{K}}(\mathbf{x}',s) - \gamma_0\boldsymbol{\Theta}\times\hat{\mathbf{J}}(\mathbf{x}',s)\right]\mathrm{d}V. \quad (3.15)$$

The integrals are evaluated over the source domain $\mathbb{D}$. Furthermore, $\boldsymbol{\Theta} = \frac{\mathbf{x}-\mathbf{x}'}{|\mathbf{x}-\mathbf{x}'|}$ is a unit vector in the direction $\mathbf{x}-\mathbf{x}'$, i.e. a vector pointing from the source to the receiver, and $\mathbb{Q}$ is a projection matrix defined as $\boldsymbol{\Theta}\boldsymbol{\Theta}^T$. Finally, the propagation coefficient of vacuum $\gamma_0 = (\eta_0\zeta_0)^{\frac{1}{2}} = \frac{s}{c_0}$ with $\mathrm{Re}(\gamma_0) \geq 0$.

Now, the electric- and magnetic field at location $\mathbf{x}$ can be determined for a specific source. The first integral in Eqs. (3.14) and (3.15) represents the near-field as this term is much larger than the other two integrals when evaluated at small distances. The third term is the far-field as this term dominates at large distances. Finally, the mid-term represents the intermediate field.

To work with these equations, it is necessary to know what source is being used in the configuration, which in our case is a small loop-antenna. Such an antenna can be represented as a point source in the form of a magnetic current density as

$$\mathbf{K}(\mathbf{x},t) = \mu_0\partial_t\mathbf{m}\delta(\mathbf{x}-\mathbf{x}^{\mathrm{s}}), \quad (3.16)$$

where $\mathbf{x}^s$ is the position of the source and $\mathbf{m}$ is the moment of the antenna. This moment is defined as $\mathbf{m} = I(t)A\mathbf{n}$, where I is the current through the loop, A is the area of the loop, and $\mathbf{n}$ is the normal vector perpendicular to this loop. In the Laplace domain this source is equal to $\hat{\mathbf{K}}(\mathbf{x},s) = \zeta_0\hat{I}(s)\pi a^2\delta(\mathbf{x}-\mathbf{x}^{\mathrm{s}})\mathbf{n}$, with a being the radius of the loop. The electric current density $\mathbf{J}$ can be set to zero as there is no other source present. Equations (3.14) and (3.15) can now be written as

$$\hat{\mathbf{E}}(\mathbf{x},s) = \frac{e^{-\gamma_0|\mathbf{x}-\mathbf{x}^{\mathrm{s}}|}}{4\pi|\mathbf{x}-\mathbf{x}^s|^2}\boldsymbol{\Theta}\times\zeta_0\hat{I}(s)\pi a^2\mathbf{n} + \frac{e^{-\gamma_0|\mathbf{x}-\mathbf{x}^{\mathrm{s}}|}}{4\pi|\mathbf{x}-\mathbf{x}^{\mathrm{s}}|}\gamma_0\boldsymbol{\Theta}\times\zeta_0\hat{I}(s)\pi a^2\mathbf{n}, \quad (3.17)$$

and

$$\hat{\mathbf{H}}(\mathbf{x},s) = \frac{e^{-\gamma_0|\mathbf{x}-\mathbf{x}^{\mathrm{s}}|}}{4\pi|\mathbf{x}-\mathbf{x}^{\mathrm{s}}|^3}(3\mathbb{Q}-\mathbb{I})\frac{1}{\zeta_0}\zeta_0\hat{I}(s)\pi a^2\mathbf{n} + \frac{e^{-\gamma_0|\mathbf{x}-\mathbf{x}^{\mathrm{s}}|}}{4\pi|\mathbf{x}-\mathbf{x}^{\mathrm{s}}|^2}(3\mathbb{Q}-\mathbb{I})\frac{\gamma_0}{\zeta_0}\zeta_0\hat{I}(s)\pi a^2\mathbf{n} + \frac{e^{-\gamma_0|\mathbf{x}-\mathbf{x}^{\mathrm{s}}|}}{4\pi|\mathbf{x}-\mathbf{x}^{\mathrm{s}}|}(3\mathbb{Q}-\mathbb{I})\frac{\gamma_0^2}{\zeta_0}\zeta_0\hat{I}(s)\pi a^2\mathbf{n}. \quad (3.18)$$

From Eq. (3.17), we observe that the electric field strength is completely transverse to $\mathbf{n}$, that is, $\mathbf{n}\cdot\hat{\mathbf{E}} = 0$. For example, if the loop is oriented in the z-direction ($\mathbf{n} = \mathbf{i}_z$), then $\hat{\mathbf{E}}_z = 0$.

In our NDT application, we are usually only interested in the electromagnetic field very close to the source. This means that for all practical purposes, the electromagnetic field can be approximated by

$$\hat{\mathbf{E}}^{\text{inc}}(\mathbf{x}, s) = \frac{a^2 \zeta_0 e^{-\gamma_0 |\mathbf{x}-\mathbf{x}^s|}}{4|\mathbf{x}-\mathbf{x}^s|^2} \boldsymbol{\Theta} \times \hat{I}(s)\mathbf{n} \tag{3.19}$$

and

$$\hat{\mathbf{H}}^{\text{inc}}(\mathbf{x}, s) = \frac{a^2 e^{-\gamma_0 |\mathbf{x}-\mathbf{x}^s|}}{4|\mathbf{x}-\mathbf{x}^s|^3} (3\mathbb{Q} - \mathbb{I}) \hat{I}(s)\mathbf{n}, \tag{3.20}$$

since the remaining terms essentially vanish within our domain of interest. These final equations are the incident electromagnetic fields in the near-field of the loop-antenna.

3.2.2 The background electromagnetic field

The incident field has been derived in the previous subsection. The next step is to include the roll in our configuration as depicted in Figure 3.2. This roll will interact with the incident field as it induces electric- and magnetic currents and consequently radiates a new electromagnetic field. This field is said to be the scattered field and needs to be found. If this field is known, then the background field is found as well by a simple superposition of the incident- and scattered field.

Equations (3.14) and (3.15) can be used again to find the scattered field. As the roll is in the near-field of the antenna, all the terms which are hardly of any influence on the fields can be neglected. Also, the sources in these equations are replaced by the induced sources using the constitutive relations given by

$$\hat{\mathbf{J}}^{\text{ind}}(\mathbf{x}, s) = \left[\sigma^{\text{roll}} + s(\varepsilon^{\text{roll}} - \varepsilon_0)\right] \hat{\mathbf{E}}(\mathbf{x}, s), \tag{3.21}$$

and

$$\hat{\mathbf{K}}^{\text{ind}}(\mathbf{x}, s) = s(\mu^{\text{roll}} - \mu_0) \hat{\mathbf{H}}(\mathbf{x}, s). \tag{3.22}$$

We arrive at

$$\begin{aligned} \hat{\mathbf{E}}^{\text{sc}}(\mathbf{x}, s) = &\int_{\mathbf{x}' \in \mathbb{D}^{\text{roll}}} \frac{e^{-\gamma_0 |\mathbf{x}-\mathbf{x}'|}}{4\pi|\mathbf{x}-\mathbf{x}'|^3} (3\mathbb{Q} - \mathbb{I}) \frac{1}{\eta_0} \hat{\mathbf{J}}^{\text{ind}}(\mathbf{x}', s) \mathrm{d}V \\ &+ \int_{\mathbf{x}' \in \mathbb{D}^{\text{roll}}} \frac{e^{-\gamma_0 |\mathbf{x}-\mathbf{x}'|}}{4\pi|\mathbf{x}-\mathbf{x}'|^2} \boldsymbol{\Theta} \times \hat{\mathbf{K}}^{\text{ind}}(\mathbf{x}', s) \mathrm{d}V, \end{aligned} \tag{3.23}$$

and

$$\begin{aligned} \hat{\mathbf{H}}^{\text{sc}}(\mathbf{x}, s) = &\int_{\mathbf{x}' \in \mathbb{D}^{\text{roll}}} \frac{e^{-\gamma_0 |\mathbf{x}-\mathbf{x}'|}}{4\pi|\mathbf{x}-\mathbf{x}'|^3} (3\mathbb{Q} - \mathbb{I}) \frac{1}{\zeta_0} \hat{\mathbf{K}}^{\text{ind}}(\mathbf{x}', s) \mathrm{d}V \\ &- \int_{\mathbf{x}' \in \mathbb{D}^{\text{roll}}} \frac{e^{-\gamma_0 |\mathbf{x}-\mathbf{x}'|}}{4\pi|\mathbf{x}-\mathbf{x}'|^2} \boldsymbol{\Theta} \times \hat{\mathbf{J}}^{\text{ind}}(\mathbf{x}', s) \mathrm{d}V. \end{aligned} \tag{3.24}$$

Now, as mentioned in the previous chapter, in typical applications the conduction currents dominate the displacement currents inside the roll. Consequently, we have

$$\hat{\mathbf{J}}^{\mathrm{ind}}(\mathbf{x}, s) = \sigma^{\mathrm{roll}}\hat{\mathbf{E}}(\mathbf{x}, s). \tag{3.25}$$

Taking into account the explicit expressions for the induced currents given by Eqs. (3.22) and (3.25), we arrive at

$$\begin{aligned}\hat{\mathbf{E}}^{\mathrm{sc}}(\mathbf{x}, s) = \frac{\sigma^{\mathrm{roll}}}{\eta_0} \int\limits_{\mathbf{x}' \in \mathbb{D}^{\mathrm{roll}}} \frac{e^{-\gamma_0|\mathbf{x}-\mathbf{x}'|}}{4\pi|\mathbf{x}-\mathbf{x}'|^3}(3\mathbb{Q} - \mathbb{I})\hat{\mathbf{E}}(\mathbf{x}', s)\mathrm{d}V \\ + \left(\frac{\mu^{\mathrm{roll}}}{\mu_0} - 1\right) \int\limits_{\mathbf{x}' \in \mathbb{D}^{\mathrm{roll}}} \frac{e^{-\gamma_0|\mathbf{x}-\mathbf{x}'|}}{4\pi|\mathbf{x}-\mathbf{x}'|^2}\boldsymbol{\Theta} \times \zeta_0\hat{\mathbf{H}}(\mathbf{x}', s))\mathrm{d}V,\end{aligned} \tag{3.26}$$

and

$$\begin{aligned}\hat{\mathbf{H}}^{\mathrm{sc}}(\mathbf{x}, s) = \left(\frac{\mu^{\mathrm{roll}}}{\mu_0} - 1\right) \int\limits_{\mathbf{x}' \in \mathbb{D}^{\mathrm{roll}}} \frac{e^{-\gamma_0|\mathbf{x}-\mathbf{x}'|}}{4\pi|\mathbf{x}-\mathbf{x}'|^3}(3\mathbb{Q} - \mathbb{I})\hat{\mathbf{H}}(\mathbf{x}', s)\mathrm{d}V \\ - \frac{\sigma^{\mathrm{roll}}}{\eta_0} \int\limits_{\mathbf{x}' \in \mathbb{D}^{\mathrm{roll}}} \frac{e^{-\gamma_0|\mathbf{x}-\mathbf{x}'|}}{4\pi|\mathbf{x}-\mathbf{x}'|^2}\boldsymbol{\Theta} \times \eta_0\hat{\mathbf{E}}(\mathbf{x}', s)\mathrm{d}V.\end{aligned} \tag{3.27}$$

If the field inside the roll is known (here $\hat{\mathbf{E}}$ and $\hat{\mathbf{H}}$), the background field is found by summing the incident field due the antenna and the scattered field due to the roll as

$$\hat{\mathbf{E}}^{\mathrm{bg}}(\mathbf{x}, s) = \hat{\mathbf{E}}^{\mathrm{inc}}(\mathbf{x}, s) + \hat{\mathbf{E}}^{\mathrm{sc}}(\mathbf{x}, s), \tag{3.28}$$

and

$$\hat{\mathbf{H}}^{\mathrm{bg}}(\mathbf{x}, s) = \hat{\mathbf{H}}^{\mathrm{inc}}(\mathbf{x}, s) + \hat{\mathbf{H}}^{\mathrm{sc}}(\mathbf{x}, s). \tag{3.29}$$

At this moment, however, the fields inside the roll are unknown. In fact, this field is a combination of the incident field and some self-interaction terms. These latter fields are caused by induced currents and these can be seen as new sources which induce new currents in the metal again. In addition, the field inside the roll strongly attenuates in depth due to the conductivity. Because of these reasons, $\hat{\mathbf{E}}(\mathbf{x}', s)$ and $\hat{\mathbf{H}}(\mathbf{x}', s)$ in above equations are hard to determine. In order to find the fields inside the roll explicitly, some additional expressions are necessary.

An approximation regarding the geometry of the roll is made to ease the derivation for the fields inside the object. Since the antenna is close to the surface, the curvature of the roll becomes negligible and the roll itself becomes extremely large compared to the height of the antenna above the metal. This implies that the roll can be seen as an infinitely large conducting half-space as depicted in Figure 3.3. Here, the loop-antenna is placed at a height of $z = -h$ with its winding parallel to the roll. The boundary between the two layers is placed at $z = 0$. The top-layer is labeled as medium a, while the conductive bottom-layer is labeled as medium b.

The background field is found more easily in this new setup because of two reasons:

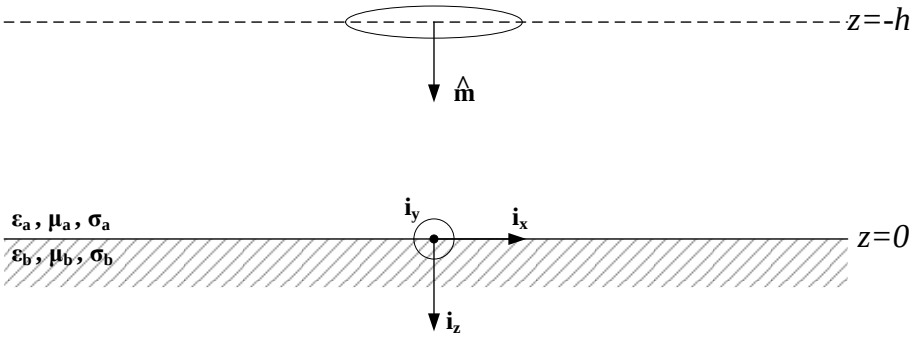

Figure 3.3: Half-space with a magnetic dipole at height $z = -h$ above the roll which occupies the domain $z > 0$. Both layers have their own medium properties ε, σ and μ.

1. The antenna only excites in vertical direction (i.e. the z-direction) and excitations in other directions can be set to zero;
2. The configuration is invariant in x- and y-direction. Consequently, the electromagnetic field can be found using spatial Fourier transformation techniques.

Let us now be more specific. First, recall that a small z-directed loop antenna located in medium a can be modelled as an external magnetic-current source of the form

$$\hat{\mathbf{K}}(\mathbf{x}, s) = \zeta_{\mathrm{a}} \hat{m} \delta(x)\delta(y)\delta(z-h)\mathbf{i}_z \tag{3.30}$$

and obviously we also have

$$\hat{\mathbf{J}}(\mathbf{x}, s) = 0. \tag{3.31}$$

Here, $\hat{m} = \pi a^2 I(s)$ and the unit vector $\mathbf{i}_z$ is extracted from the dipole moment as in this setup the moment of the antenna is directed in the z-direction, implying that the loop is parallel to the surface of the roll. Equations (3.11) and (3.12) give solutions for the electromagnetic field in terms of vector potentials which we can use. Since there is no electric current source, there is also no electric vector potential. This means $\hat{\mathbf{A}}$ can be set to zero and the equations become

$$\hat{\mathbf{E}}(\mathbf{x}, s) = -\nabla \times \hat{\mathbf{F}}, \tag{3.32}$$

and

$$\hat{\mathbf{H}}(\mathbf{x}, s) = -\eta_n \hat{\mathbf{F}} + \frac{1}{\zeta_n} \nabla \nabla \cdot \hat{\mathbf{F}}, \tag{3.33}$$

where $\eta_n = \sigma_n + s\varepsilon_n$ and $\zeta_n = s\mu_n$ are the medium parameters of medium n ($n = \mathrm{a}$ or $n = \mathrm{b}$). In our NDT application, the lower halfspace $z > 0$ is occupied by the roll (medium b), while medium a consists of air.

When operating at a frequency ω ($s = -\mathrm{i}\omega$), we know the frequency-domain magnetic vector potential $\hat{\mathbf{F}}$ should satisfy Helmholtz's equation in both the upper and lower halfspace. Explicitly, we have

$$(\nabla^2 + k_{\mathrm{a}}^2)\hat{\mathbf{F}} = -\zeta_{\mathrm{a}}\hat{m}\delta(x)\delta(y)\delta(z-h)\mathbf{i}_z \qquad \text{for } z < 0 \tag{3.34}$$

and

$$(\nabla^2 + k_{\mathrm{b}}^2)\hat{\mathbf{F}} = 0 \qquad \text{for } z > 0, \tag{3.35}$$

where $k_n = (-\eta_n\zeta_n)^{1/2}$ is the wave number with $\mathrm{Im}(k_n) \geq 0$. Notice that the right-hand side of the Helmholtz equation in medium b vanishes, since the source is located in the upper halfspace.

From the above equations we observe that only the z-component of the vector potential is excited and $\hat{F}_x$ and $\hat{F}_y$ are equal to zero. We are left with

$$(\partial_x^2 + \partial_y^2 + \partial_z^2 + k_{\mathrm{a}}^2)\hat{F}_z = -\zeta_{\mathrm{a}}\hat{m}\delta(x)\delta(y)\delta(z-h) \qquad \text{for } z < 0, \tag{3.36}$$

and

$$(\partial_x^2 + \partial_y^2 + \partial_z^2 + k_{\mathrm{b}}^2)\hat{F}_z = 0 \qquad \text{for } z > 0, \tag{3.37}$$

and from Eqs. (3.32) and (3.33) it follows that

$$\hat{E}_x = -\partial_y\hat{F}_z, \tag{3.38}$$

$$\hat{E}_y = \partial_x\hat{F}_z, \tag{3.39}$$

$$\hat{E}_z = 0, \tag{3.40}$$

$$\hat{H}_x = \hat{\zeta}_n^{-1}\partial_x\partial_z\hat{F}_z, \tag{3.41}$$

$$\hat{H}_y = \hat{\zeta}_n^{-1}\partial_y\partial_z\hat{F}_z, \tag{3.42}$$

and

$$\hat{H}_z = \hat{\zeta}_n^{-1}\partial_z^2\hat{F}_z - \hat{\eta}_n\hat{F}_z = \hat{\zeta}_n^{-1}(\partial_z^2 + k_n^2)\hat{F}_z. \tag{3.43}$$

We again observe that the z-component of the electric field vanishes, which means the electric field is completely transverse to the z-direction.

As mentioned before, the configuration considered here exhibits a spatial invariance in the x- and y-directions at any point in space. This property can be exploited by applying a spatial Fourier transformation with respect to the x- and y-coordinates. The forward Fourier transform is defined as

$$\tilde{F}_z(k_x, k_y, z, \omega) = \int_{x=-\infty}^{\infty}\int_{y=-\infty}^{\infty} \hat{F}_z(x, y, z, \omega)e^{-i(k_x x + k_y y)}\mathrm{d}x\mathrm{d}y, \tag{3.44}$$

while the inverse Fourier transform is given by

$$\hat{F}_z(x, y, z, \omega) = \frac{1}{4\pi^2}\int_{k_x=-\infty}^{\infty}\int_{k_y=-\infty}^{\infty} \tilde{F}_z(k_x, k_y, z, \omega)e^{i(k_x x + k_y y)}\mathrm{d}k_x\mathrm{d}k_y. \tag{3.45}$$

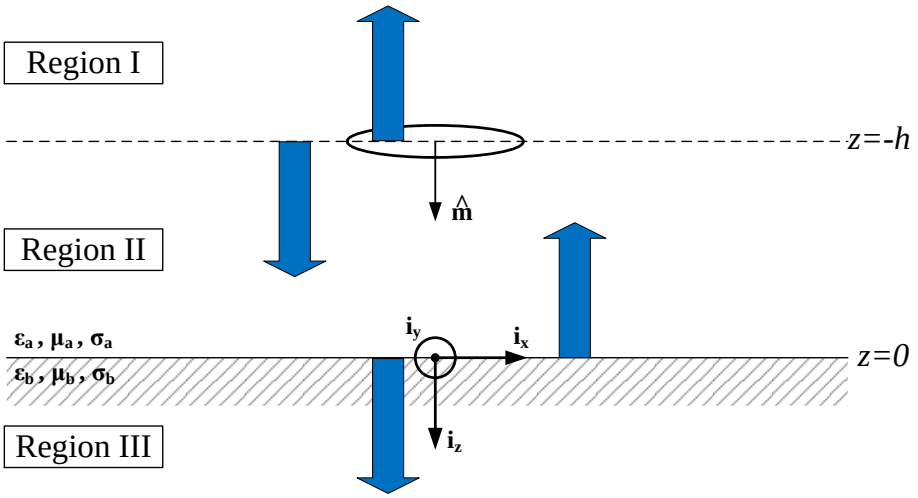

Figure 3.4: The configuration is divided into three regions, Region I only has wave propagation in negative z-direction, Region III only in positive z-direction and Region II has both

Applying now the spatial Fourier transform to Eqs. (3.36) and (3.37), we obtain

$$(\partial_z^2 - \gamma_\mathrm{a}^2)\tilde{F}_z = -\zeta_\mathrm{a} r\hat{m}\delta(z-h) \qquad \text{for } z < 0, \tag{3.46}$$

and

$$(\partial_z^2 - \gamma_\mathrm{b}^2)\tilde{F}_z = 0 \qquad \text{for } z > 0, \tag{3.47}$$

where γ_a and γ_b have been introduced as

$$\gamma_\mathrm{a} = (k_x^2 + k_y^2 - k_\mathrm{a}^2)^{\frac{1}{2}} \quad \text{with } \mathrm{Re}(\gamma_\mathrm{a}) \geq 0,$$

and

$$\gamma_\mathrm{b} = (k_x^2 + k_y^2 - k_\mathrm{b}^2)^{\frac{1}{2}} \quad \text{with } \mathrm{Re}(\gamma_\mathrm{b}) \geq 0.$$

As a reminder, the idea is to find solutions for the magnetic potential F_z such that the electromagnetic fields can be found. For this purpose the configuration from Figure 3.3 is divided into three regions as is shown in Figure 3.4. In Region I there is only an upward traveling wave (negative z-direction), Region II has both an upward and downward traveling wave, and Region III only has a downward traveling wave (positive z-direction).

In Region I, there is no source present and the fields are in medium a. Therefore, Eq. (3.46) is valid with a vanishing right-hand side. We have

$$(\partial_z^2 - \gamma_\mathrm{a}^2)\tilde{F}_z = 0. \tag{3.48}$$

A general solution for $\tilde{F}_z$ for this equation is

$$\tilde{F}_z = \tilde{a}^+ e^{-\gamma_\mathrm{a} z} + \tilde{\mathrm{a}}^- e^{\gamma_\mathrm{a} z}. \tag{3.49}$$

This equation should remain bounded for $z \to -\infty$. This is only true if $\tilde{a}^+ = 0$.

In Region III, Eq. (3.47) is applicable and a general solution for this equation is

$$\tilde{F}_z = \tilde{\mathrm{c}}^+ e^{-\gamma_\mathrm{b} z} + \tilde{\mathrm{c}}^- e^{\gamma_\mathrm{b} z}. \tag{3.50}$$

Here, the solution should remain bounded for $z \to \infty$, implying $\tilde{c}^- = 0$. Since Region II is already bounded by the regions surrounding it, the solutions for $\tilde{F}_z$ become

$$\text{Region I} \qquad \tilde{F}_z = \tilde{\mathrm{a}}^- e^{\gamma_\mathrm{a} z} \qquad z < -h, \tag{3.51}$$

$$\text{Region II} \qquad \tilde{F}_z = \tilde{\mathrm{b}}^+ e^{-\gamma_\mathrm{a} z} + \tilde{\mathrm{b}}^- e^{\gamma_\mathrm{a} z} \qquad -h < z < 0, \tag{3.52}$$

and

$$\text{Region III} \qquad \tilde{F}_z = \tilde{\mathrm{c}}^+ e^{-\gamma_\mathrm{b} z} \qquad z > 0. \tag{3.53}$$

The problem of finding $\tilde{F}_z(\mathbf{k}, s)$ has shifted to finding the coefficients $\tilde{\mathrm{a}}^-$, $\tilde{\mathrm{b}}^-$, $\tilde{\mathrm{b}}^+$, and $\tilde{\mathrm{c}}^+$. These coefficients can be found by invoking the electromagnetic boundary and source conditions at $z = 0$ and $z = -h$, respectively. As soon as the coefficients have been found, the solutions for $\tilde{F}_z(\mathbf{k}, s)$ must be transformed back to the $(\mathbf{x}, s)$-domain. Hereafter, the required background field for a half-space configuration can be found using Eqs. (3.38)-(3.43). These latter steps have all been carried out in Appendix B and the results have been summarized in Table 3.1. In this table, J_0 and J_1 are the Bessel functions of the first kind and order zero and one, respectively. Region I is not included, since we do not carry out any measurements in this domain. The equations in the table present the complete solution for the background electromagnetic field.

Table 3.1: Background fields for regions II and III

Region II ($-h < z < 0$)	Region III ($z > 0$)
$\hat{E}_x = \frac{y}{\rho}\frac{\hat{\zeta}_\mathrm{a}\hat{m}}{4\pi}\int\limits_{\lambda=0}^{\infty}\frac{\lambda^2}{\gamma_\mathrm{a}}[e^{-\gamma_\mathrm{a}(z+h)} + Re^{\gamma_\mathrm{a}(z-h)}]J_1(\lambda\rho)\mathrm{d}\lambda$	$\hat{E}_x = \frac{y}{\rho}\frac{\hat{\zeta}_\mathrm{a}\hat{m}}{4\pi}\int\limits_{\lambda=0}^{\infty}\frac{\lambda^2}{\gamma_a}Te^{-\gamma_a h}e^{-\gamma_\mathrm{b} z}J_1(\lambda\rho)\mathrm{d}\lambda$
$\hat{E}_y = -\frac{x}{\rho}\frac{\hat{\zeta}_\mathrm{a}\hat{m}}{4\pi}\int\limits_{\lambda=0}^{\infty}\frac{\lambda^2}{\gamma_\mathrm{a}}[e^{-\gamma_\mathrm{a}(z+h)} + Re^{\gamma_\mathrm{a}(z-h)}]J_1(\lambda\rho)\mathrm{d}\lambda$	$\hat{E}_y = -\frac{x}{\rho}\frac{\hat{\zeta}_\mathrm{a}\hat{m}}{4\pi}\int\limits_{\lambda=0}^{\infty}\frac{\lambda^2}{\gamma_\mathrm{a}}Te^{-\gamma_\mathrm{a}h}e^{-\gamma_\mathrm{b} z}J_1(\lambda\rho)\mathrm{d}\lambda$
$\hat{E}_z = 0$	$\hat{E}_z = 0$
$\hat{H}_x = \frac{\hat{m}}{4\pi}\frac{x}{\rho}\int\limits_{\lambda=0}^{\infty}[(e^{-\gamma_\mathrm{a}(z+h)} - Re^{\gamma_\mathrm{a}(z-h)}]\lambda^2 J_1(\lambda\rho)\mathrm{d}\lambda$	$\hat{H}_x = \frac{\hat{\zeta}_\mathrm{a}}{\hat{\zeta}_\mathrm{b}}\frac{x}{\rho}\frac{\hat{m}}{4\pi}\int\limits_{\lambda=0}^{\infty}\lambda^2\frac{\gamma_\mathrm{b}}{\gamma_\mathrm{a}}Te^{-\gamma_\mathrm{a}h}e^{-\gamma_\mathrm{b} z}J_1(\lambda\rho)\mathrm{d}\lambda$
$\hat{H}_y = \frac{\hat{m}}{4\pi}\frac{y}{\rho}\int\limits_{\lambda=0}^{\infty}[(e^{-\gamma_\mathrm{a}(z+h)} - Re^{\gamma_\mathrm{a}(z-h)}]\lambda^2 J_1(\lambda\rho)\mathrm{d}\lambda$	$\hat{H}_y = \frac{\hat{\zeta}_\mathrm{a}}{\hat{\zeta}_\mathrm{b}}\frac{y}{\rho}\frac{\hat{m}}{4\pi}\int\limits_{\lambda=0}^{\infty}\lambda^2\frac{\gamma_\mathrm{b}}{\gamma_\mathrm{a}}Te^{-\gamma_\mathrm{a}h}e^{-\gamma_\mathrm{b} z}J_1(\lambda\rho)\mathrm{d}\lambda$
$\hat{H}_z = \frac{\hat{m}}{4\pi}\int\limits_{\lambda=0}^{\infty}\frac{\lambda^3}{\gamma_\mathrm{a}}[e^{-\gamma_\mathrm{a}(z+h)} + Re^{\gamma_\mathrm{a}(z-h)}]J_0(\lambda\rho)\mathrm{d}\lambda$	$\hat{H}_z = \frac{\hat{\zeta}_\mathrm{a}}{\hat{\zeta}_\mathrm{b}}\frac{\hat{m}}{4\pi}\int\limits_{\lambda=0}^{\infty}\frac{\lambda^3}{\gamma_\mathrm{a}}Te^{-\gamma_\mathrm{a}h}e^{-\gamma_\mathrm{b} z}J_0(\lambda\rho)\mathrm{d}\lambda$
$\hat{F}_z(\rho,z,\omega) = \frac{\hat{\zeta}_\mathrm{a}\hat{m}}{4\pi}\int\limits_{\lambda=0}^{\infty}\frac{\lambda}{\gamma_\mathrm{a}}[e^{-\gamma_\mathrm{a}(z+h)} + Re^{\gamma_\mathrm{a}(z-h)}]J_0(\lambda\rho)\mathrm{d}\lambda$	$\hat{F}_z(\rho,z,\omega) = \frac{\hat{\zeta}_\mathrm{a}\hat{m}}{4\pi}\int\limits_{\lambda=0}^{\infty}\frac{\lambda}{\gamma_\mathrm{a}}Te^{-\gamma_\mathrm{a}h}e^{-\gamma_\mathrm{b} z}J_0(\lambda\rho)\mathrm{d}\lambda$
$R = \frac{\gamma_\mathrm{a}-\gamma_\mathrm{b}}{\gamma_\mathrm{a}+\gamma_\mathrm{b}}$	$T = \frac{2\gamma_\mathrm{a}}{\gamma_\mathrm{a}+\gamma_\mathrm{b}}$
$\gamma_\mathrm{n} = (\lambda^2 - k_\mathrm{n}^2)^{\frac{1}{2}}$ with $\Re(\gamma_\mathrm{n}) \geq 0$	$k_\mathrm{n} = (-\hat{\eta}_\mathrm{n}\hat{\zeta}_\mathrm{n})^{\frac{1}{2}}$ with $\mathrm{Im}(k_n) \geq 0$
$\lambda^2 = k_x^2 + k_y^2, \quad \rho^2 = x^2 + y^2$	$\hat{\eta}_\mathrm{n} = \sigma_\mathrm{n} - i\omega\varepsilon_\mathrm{n}, \quad \hat{\zeta}_\mathrm{n} = -i\omega\mu_\mathrm{n}$

3.2.3 The total electromagnetic field

In the previous subsections the incident field and the background field have been determined completely. The background field is the field that is present if there is no defect in the roll, i.e. a clean roll. If there is a flaw in the metal then the fields arriving at a receiver will be slightly different. Specifically, we have

$$\hat{\mathbf{E}}^{\mathrm{tot}}(\mathbf{x}, s) = \hat{\mathbf{E}}^{\mathrm{bg}}(\mathbf{x}, s) + \hat{\mathbf{E}}^{\mathrm{d}}(\mathbf{x}, s), \tag{3.54}$$

and

$$\hat{\mathbf{H}}^{\mathrm{tot}}(\mathbf{x}, s) = \hat{\mathbf{H}}^{\mathrm{bg}}(\mathbf{x}, s) + \hat{\mathbf{H}}^{\mathrm{d}}(\mathbf{x}, s). \tag{3.55}$$

This latter term is the field caused by deviations in conductivity or permeability due to a crack or weak spot which causes fluctuations in the field. The source of these defects can be defined in the same manner as Eqs. (3.22) and (3.25), i.e.

$$\hat{\mathbf{J}}^{\mathrm{d}}(\mathbf{x}, s) = \left[\sigma^{\mathrm{d}} - \sigma^{\mathrm{roll}} + s(\varepsilon^{\mathrm{d}} - \varepsilon^{\mathrm{roll}})\right] \hat{\mathbf{E}}^{\mathrm{tot}}(\mathbf{x}, s) \tag{3.56}$$

and

$$\hat{\mathbf{K}}^{\mathrm{d}}(\mathbf{x}, s) = s(\mu^{\mathrm{d}} - \mu^{\mathrm{roll}})\hat{\mathbf{H}}^{\mathrm{tot}}(\mathbf{x}, s). \tag{3.57}$$

The scattered field can be found by using the Maxwell equations, which are given by

$$\begin{aligned}\hat{\mathbf{E}}^{\mathrm{d}}(\mathbf{x}, s) = &\int_{\mathbf{x}' \in \mathbb{D}^{\mathrm{d}}} \mathbf{G}^{\mathrm{EJ}}(\mathbf{x} - \mathbf{x}')\hat{\mathbf{J}}^{\mathrm{d}}(\mathbf{x}', s)\mathrm{d}V \\ &+ \int_{\mathbf{x}' \in \mathbb{D}^{\mathrm{d}}} \mathbf{G}^{\mathrm{EK}}(\mathbf{x} - \mathbf{x}')\hat{\mathbf{K}}^{\mathrm{d}}(\mathbf{x}', s)\mathrm{d}V,\end{aligned} \tag{3.58}$$

and

$$\begin{aligned}\hat{\mathbf{H}}^{\mathrm{d}}(\mathbf{x}, s) = &\int_{\mathbf{x}' \in \mathbb{D}^{\mathrm{d}}} \mathbf{G}^{\mathrm{HJ}}(\mathbf{x} - \mathbf{x}')\hat{\mathbf{J}}^{\mathrm{d}}(\mathbf{x}', s)\mathrm{d}V \\ &+ \int_{\mathbf{x}' \in \mathbb{D}^{\mathrm{d}}} \mathbf{G}^{\mathrm{HK}}(\mathbf{x} - \mathbf{x}')\hat{\mathbf{K}}^{\mathrm{d}}(\mathbf{x}', s)\mathrm{d}V.\end{aligned} \tag{3.59}$$

The sources are given by Eqs. (3.56) and (3.57). The permittivity of the metal is close to that of vacuum, in addition we work with low frequencies, therefore these two sources become

$$\hat{\mathbf{J}}^{\mathrm{d}}(\mathbf{x}, s) = (\sigma^{\mathrm{d}} - \sigma^{\mathrm{roll}})\hat{\mathbf{E}}^{\mathrm{tot}}(\mathbf{x}, s) = \delta\sigma\hat{\mathbf{E}}^{\mathrm{tot}}(\mathbf{x}, s) \tag{3.60}$$

and

$$\hat{\mathbf{K}}^{\mathrm{d}}(\mathbf{x}, s) = s(\mu^{\mathrm{d}} - \mu^{\mathrm{roll}})\hat{\mathbf{H}}^{\mathrm{tot}}(\mathbf{x}, s) = \delta\mu\hat{\mathbf{H}}^{\mathrm{tot}}(\mathbf{x}, s). \tag{3.61}$$

Substituting these results in Maxwell's equations gives

$$\hat{\mathbf{E}}^{\mathrm{d}}(\mathbf{x},s) = \delta\sigma \int\limits_{\mathbf{x}'\in\mathbb{D}^{\mathrm{d}}} \mathbf{G}^{\mathrm{EJ}}(\mathbf{x}-\mathbf{x}')\hat{\mathbf{E}}^{\mathrm{tot}}(\mathbf{x}',s)\mathrm{d}V + \delta\mu \int\limits_{\mathbf{x}'\in\mathbb{D}^{\mathrm{d}}} \mathbf{G}^{\mathrm{EK}}(\mathbf{x}-\mathbf{x}')\hat{\mathbf{H}}^{\mathrm{tot}}(\mathbf{x}',s)\mathrm{d}V, \tag{3.62}$$

and

$$\hat{\mathbf{H}}^{\mathrm{d}}(\mathbf{x},s) = \delta\sigma \int\limits_{\mathbf{x}'\in\mathbb{D}^{\mathrm{d}}} \mathbf{G}^{\mathrm{HJ}}(\mathbf{x}-\mathbf{x}')\hat{\mathbf{E}}^{\mathrm{tot}}(\mathbf{x}',s)\mathrm{d}V + \delta\mu \int\limits_{\mathbf{x}'\in\mathbb{D}^{\mathrm{d}}} \mathbf{G}^{\mathrm{HK}}(\mathbf{x}-\mathbf{x}')\hat{\mathbf{H}}^{\mathrm{tot}}(\mathbf{x}',s)\mathrm{d}V. \tag{3.63}$$

Equations (3.54) and (3.55) can now be used to find solutions for the total electromagnetic field.

3.3 Change in the impedance due to a defect

In the last section the electromagnetic fields have been derived for the background and the scatterer. However, these expressions do not give a direct relation between the change in the impedance and the presence of a defect. With the use of Lorentz's reciprocity theorem, it is possible to arrive at such a relation [27]. The reciprocity theorem interconnects two different states (called A and B) which both are possible to occur in one and the same domain. Each state has its own source and medium parameters. The two states relevant for

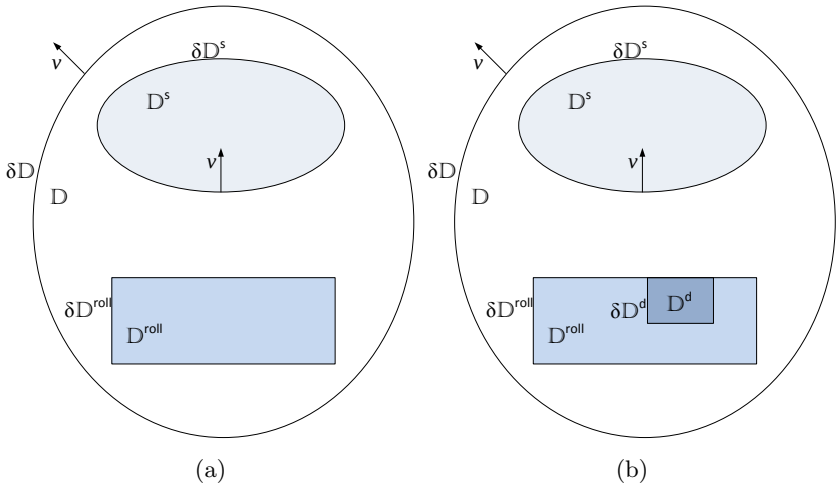

Figure 3.5: The two different states which are used in the reciprocity theory. The left-hand side shows a roll without a defect (state A) and the right-hand side a roll with a defect (state B).

our NDT application are specified in Table 3.2 and illustrated in Figures 3.5a and 3.5b. In these figures, $\mathbb{D}^{\text{roll}}$ is the domain occupied by the roll, $\mathbb{D}^{\text{d}}$ is the domain occupied by the defect, while the domain $\mathbb{D}^{\text{s}}$ contains the transmitting and receiving antennas. This domain has a closed boundary surface $\partial\mathbb{D}^{\text{s}}$. Furthermore, the domain surrounding the roll, defect, and antenna domain is denoted by $\mathbb{D}$. This domain has a closed outer boundary surface $\partial\mathbb{D}$. Notice that domain $\mathbb{D}$ is source-free, since all sources are located within the domain $\mathbb{D}^{\text{s}}$.

For a general time-invariant and bounded domain $\mathbb{D}$ with closed boundary $\partial\mathbb{D}$ and outward unit normal $\boldsymbol{\nu}$, Lorentz's reciprocity theorem is given by [27]

$$\begin{aligned}
&\int_{\mathbf{x}\in\partial\mathbb{D}} \left(\hat{\mathbf{E}}^{\text{A}} \times \hat{\mathbf{H}}^{\text{B}} - \hat{\mathbf{E}}^{\text{B}} \times \hat{\mathbf{H}}^{\text{A}}\right) \cdot \boldsymbol{\nu}\, \mathrm{d}A = \\
&\int_{\mathbf{x}\in\mathbb{D}} \left[-(\eta^{\text{B}} - \eta^{\text{A}})\hat{\mathbf{E}}^{\text{A}} \cdot \hat{\mathbf{E}}^{\text{B}} + (\zeta^{\text{B}} - \zeta^{\text{A}})\hat{\mathbf{H}}^{\text{A}} \cdot \hat{\mathbf{H}}^{\text{B}}\right] \mathrm{d}V \\
&+ \int_{\mathbf{x}\in\mathbb{D}} \left(\hat{\mathbf{J}}^{\text{A}} \cdot \hat{\mathbf{E}}^{\text{B}} - \hat{\mathbf{K}}^{\text{A}} \cdot \hat{\mathbf{H}}^{\text{B}} - \hat{\mathbf{J}}^{\text{B}} \cdot \hat{\mathbf{E}}^{\text{A}} + \hat{\mathbf{K}}^{\text{B}} \cdot \hat{\mathbf{H}}^{\text{A}}\right) \mathrm{d}V.
\end{aligned} \tag{3.64}$$

We now apply this theorem to the domain $\mathbb{D}$ as shown in Figures 3.5a and 3.5b and use the states as specified in Table 3.2. The above reciprocity relation then becomes

$$\begin{aligned}
&\int_{\mathbf{x}\in\partial\mathbb{D}} \left(\hat{\mathbf{E}}^{\text{bg}} \times \hat{\mathbf{H}}^{\text{tot}} - \hat{\mathbf{E}}^{\text{tot}} \times \hat{\mathbf{H}}^{\text{bg}}\right) \cdot \boldsymbol{\nu}\, \mathrm{d}A + \int_{\mathbf{x}\in\partial\mathbb{D}^{\text{s}}} \left(\hat{\mathbf{E}}^{\text{bg}} \times \hat{\mathbf{H}}^{\text{tot}} - \hat{\mathbf{E}}^{\text{tot}} \times \hat{\mathbf{H}}^{\text{bg}}\right) \cdot \boldsymbol{\nu}\, \mathrm{d}A \\
&= \int_{\mathbf{x}\in\mathbb{D}^{\text{d}}} \left(-\delta\sigma\, \hat{\mathbf{E}}^{\text{bg}} \cdot \hat{\mathbf{E}}^{\text{tot}} + s\delta\mu\, \hat{\mathbf{H}}^{\text{bg}} \cdot \hat{\mathbf{H}}^{\text{tot}}\right) \mathrm{d}V,
\end{aligned} \tag{3.65}$$

where we have introduced the differences in conductivity and permeability as

$$\delta\sigma = \sigma^{\text{d}} - \sigma^{\text{roll}} \quad \text{and} \quad \delta\mu = \mu^{\text{d}} - \mu^{\text{roll}}.$$

The first term on the left-hand side of Eq. (3.65) vanishes if we place the surface

Table 3.2: Definition states

State A	State B
$\hat{\mathbf{E}}^{\text{A}}(\mathbf{x}, s) = \hat{\mathbf{E}}^{\text{bg}}(\mathbf{x}, s) \quad (\mathbf{x} \in \mathbb{D})$	$\hat{\mathbf{E}}^{\text{B}}(\mathbf{x}, s) = \hat{\mathbf{E}}^{\text{tot}}(\mathbf{x}, s) \quad (\mathbf{x} \in \mathbb{D})$
$\hat{\mathbf{H}}^{\text{A}}(\mathbf{x}, s) = \hat{\mathbf{H}}^{\text{bg}}(\mathbf{x}, s) \quad (\mathbf{x} \in \mathbb{D})$	$\hat{\mathbf{H}}^{\text{B}}(\mathbf{x}, s) = \hat{\mathbf{H}}^{\text{tot}}(\mathbf{x}, s) \quad (\mathbf{x} \in \mathbb{D})$
$\hat{\mathbf{J}}^{\text{A}}(\mathbf{x}, s) = 0 \quad (\mathbf{x} \in \mathbb{D})$	$\hat{\mathbf{J}}^{\text{B}}(\mathbf{x}, s) = 0 \quad (\mathbf{x} \in \mathbb{D})$
$\hat{\mathbf{K}}^{\text{A}}(\mathbf{x}, s) = 0 \quad (\mathbf{x} \in \mathbb{D})$	$\hat{\mathbf{K}}^{\text{B}}(\mathbf{x}, s) = 0 \quad (\mathbf{x} \in \mathbb{D})$
$\hat{\eta}^{\text{A}} = \begin{cases} \sigma^{\text{roll}} + s\varepsilon^{\text{roll}} & \text{if } \mathbf{x} \in \mathbb{D}^{\text{roll}} \\ s\varepsilon_0 & \text{if } \mathbf{x} \notin \mathbb{D}^{\text{roll}} \end{cases}$	$\hat{\eta}^{\text{B}} = \begin{cases} \sigma^{\text{roll}} + s\varepsilon^{\text{roll}} & \text{if } \mathbf{x} \in \mathbb{D}^{\text{roll}} \\ \sigma^{\text{d}} + s\varepsilon^{\text{roll}} & \text{if } \mathbf{x} \in \mathbb{D}^{\text{d}} \\ s\varepsilon_0 & \text{if } \mathbf{x} \notin \left\{\mathbb{D}^{\text{roll}} \cup \mathbb{D}^{\text{d}}\right\} \end{cases}$
$\hat{\zeta}^{\text{A}} = \begin{cases} s\mu^{\text{roll}} & \text{if } \mathbf{x} \in \mathbb{D}^{\text{roll}} \\ s\mu_0 & \text{if } \mathbf{x} \notin \mathbb{D}^{\text{roll}} \end{cases}$	$\hat{\zeta}^{\text{B}} = \begin{cases} s\mu^{\text{roll}} & \text{if } \mathbf{x} \in \mathbb{D}^{\text{roll}} \\ s\mu^{\text{d}} & \text{if } \mathbf{x} \in \mathbb{D}^{\text{d}} \\ s\mu_0 & \text{if } \mathbf{x} \notin \left\{\mathbb{D}^{\text{roll}} \cup \mathbb{D}^{\text{d}}\right\} \end{cases}$

$\partial\mathbb{D}$ at infinity. Carrying out this procedure, we are left with

$$\int_{\mathbf{x}\in\partial\mathbb{D}^{\mathrm{s}}} \left(\hat{\mathbf{E}}^{\mathrm{bg}} \times \hat{\mathbf{H}}^{\mathrm{tot}} - \hat{\mathbf{E}}^{\mathrm{tot}} \times \hat{\mathbf{H}}^{\mathrm{bg}}\right) \cdot \boldsymbol{\nu}\, \mathrm{d}A = \int_{\mathbf{x}\in\mathbb{D}^{\mathrm{c}}} \left(-\delta\sigma\, \hat{\mathbf{E}}^{\mathrm{bg}} \cdot \hat{\mathbf{E}}^{\mathrm{tot}} + s\delta\mu\, \hat{\mathbf{H}}^{\mathrm{bg}} \cdot \hat{\mathbf{H}}^{\mathrm{tot}}\right) \mathrm{d}V. \tag{3.66}$$

Let us now focus on the surface integral on the left-hand side of Eq. (3.66). Recall that this closed surface bounds the antenna domain $\mathbb{D}^{\mathrm{s}}$.

We now assume that we operate at low frequencies and the electric field strength on $\partial\mathbb{D}^{\mathrm{s}}$ can be considered as curl-free. Consequently, we can write the electric field strength as the gradient of a potential function. Explicitly, we have

$$\hat{\mathbf{E}}^{\mathrm{bg}} = -\nabla\hat{\phi}^{\mathrm{bg}} \quad \text{and} \quad \hat{\mathbf{E}}^{\mathrm{tot}} = -\nabla\hat{\phi}^{\mathrm{tot}} \quad \text{on } \partial\mathbb{D}^{\mathrm{s}},$$

where $\hat{\phi}^{\mathrm{bg}}$ and $\hat{\phi}^{\mathrm{tot}}$ are the potential functions corresponding to $\hat{\mathbf{E}}^{\mathrm{bg}}$ and $\hat{\mathbf{E}}^{\mathrm{tot}}$, respectively.

Substitution of the above relations in the surface integral gives

$$\int_{\mathbf{x}\in\partial\mathbb{D}^{\mathrm{s}}} \left(\hat{\mathbf{E}}^{\mathrm{bg}} \times \hat{\mathbf{H}}^{\mathrm{tot}} - \hat{\mathbf{E}}^{\mathrm{tot}} \times \hat{\mathbf{H}}^{\mathrm{bg}}\right) \cdot \boldsymbol{\nu}\, \mathrm{d}A = \int_{\mathbf{x}\in\partial\mathbb{D}^{\mathrm{s}}} \left(\nabla\hat{\phi}^{\mathrm{tot}} \times \hat{\mathbf{H}}^{\mathrm{bg}} - \nabla\hat{\phi}^{\mathrm{bg}} \times \hat{\mathbf{H}}^{\mathrm{tot}}\right) \cdot \boldsymbol{\nu}\, \mathrm{d}A.$$

Using the identity

$$\nabla\hat{\phi} \times \hat{\mathbf{H}} = \nabla \times (\hat{\phi}\hat{\mathbf{H}}) - \hat{\phi}\nabla \times \hat{\mathbf{H}}$$

this can be written as

$$\int_{\mathbf{x}\in\partial\mathbb{D}^{\mathrm{s}}} \left(\hat{\mathbf{E}}^{\mathrm{bg}} \times \hat{\mathbf{H}}^{\mathrm{tot}} - \hat{\mathbf{E}}^{\mathrm{tot}} \times \hat{\mathbf{H}}^{\mathrm{bg}}\right) \cdot \boldsymbol{\nu}\, \mathrm{d}A =$$
$$\int_{\mathbf{x}\in\partial\mathbb{D}^{\mathrm{s}}} \left[\nabla \times (\hat{\phi}^{\mathrm{tot}}\hat{\mathbf{H}}^{\mathrm{bg}}) - \nabla \times (\hat{\phi}^{\mathrm{bg}}\hat{\mathbf{H}}^{\mathrm{tot}}) + \hat{\phi}^{\mathrm{bg}}\nabla \times \hat{\mathbf{H}}^{\mathrm{tot}} - \hat{\phi}^{\mathrm{tot}}\nabla \times \hat{\mathbf{H}}^{\mathrm{bg}}\right] \cdot \boldsymbol{\nu}\, \mathrm{d}A.$$

With the help of Stokes's integral theorem, it is easily shown that

$$\int_{\mathbf{x}\in\partial\mathbb{D}^{\mathrm{s}}} \left[\nabla \times (\hat{\phi}^{\mathrm{tot}}\hat{\mathbf{H}}^{\mathrm{bg}}) - \nabla \times (\hat{\phi}^{\mathrm{bg}}\hat{\mathbf{H}}^{\mathrm{tot}})\right] \cdot \boldsymbol{\nu}\, \mathrm{d}A = 0,$$

and we obtain

$$\int_{\mathbf{x}\in\partial\mathbb{D}^{\mathrm{s}}} \left(\hat{\mathbf{E}}^{\mathrm{bg}} \times \hat{\mathbf{H}}^{\mathrm{tot}} - \hat{\mathbf{E}}^{\mathrm{tot}} \times \hat{\mathbf{H}}^{\mathrm{bg}}\right) \cdot \boldsymbol{\nu}\, \mathrm{d}A = \int_{\mathbf{x}\in\partial\mathbb{D}^{\mathrm{s}}} \left(\hat{\phi}^{\mathrm{bg}}\nabla \times \hat{\mathbf{H}}^{\mathrm{tot}} - \hat{\phi}^{\mathrm{tot}}\nabla \times \hat{\mathbf{H}}^{\mathrm{bg}}\right) \cdot \boldsymbol{\nu}\, \mathrm{d}A.$$

Using Maxwell's equations in the low-frequency approximation

$$\nabla \times \hat{\mathbf{H}}^{\mathrm{bg}} = \hat{\mathbf{J}}^{\mathrm{bg}} \quad \text{and} \quad \nabla \times \hat{\mathbf{H}}^{\mathrm{tot}} = \hat{\mathbf{J}}^{\mathrm{tot}}$$

this can be written as

$$\int_{\mathbf{x}\in\partial\mathbb{D}^{\mathrm{s}}} \left(\hat{\mathbf{E}}^{\mathrm{bg}} \times \hat{\mathbf{H}}^{\mathrm{tot}} - \hat{\mathbf{E}}^{\mathrm{tot}} \times \hat{\mathbf{H}}^{\mathrm{bg}}\right) \cdot \boldsymbol{\nu}\, \mathrm{d}A = \int_{\mathbf{x}\in\partial\mathbb{D}^{\mathrm{s}}} \left(\hat{\phi}^{\mathrm{bg}}\hat{\mathbf{J}}^{\mathrm{tot}} - \hat{\phi}^{\mathrm{tot}}\hat{\mathbf{J}}^{\mathrm{bg}}\right) \cdot \boldsymbol{\nu}\, \mathrm{d}A.$$

We now assume that the current density over the surface $\partial\mathbb{D}^{\mathrm{s}}$ is mainly concentrated at the perfect conductors that form the ports of the antenna system

located in the source domain (see Figure 3.6). For an antenna system consisting of N ports [28], we then have

$$\int_{\mathbf{x}\in\partial\mathbb{D}^{\mathrm{s}}} \left(\hat{\mathbf{E}}^{\mathrm{bg}} \times \hat{\mathbf{H}}^{\mathrm{tot}} - \hat{\mathbf{E}}^{\mathrm{tot}} \times \hat{\mathbf{H}}^{\mathrm{bg}}\right) \cdot \boldsymbol{\nu}\, \mathrm{d}A = \sum_{\alpha=1}^{N} \int_{\mathbf{x}\in A_\alpha} \left(\hat{\phi}^{\mathrm{bg}} \hat{\mathbf{J}}^{\mathrm{tot}} - \hat{\phi}^{\mathrm{tot}} \hat{\mathbf{J}}^{\mathrm{bg}}\right) \cdot \boldsymbol{\nu}\, \mathrm{d}A,$$

where A_α is the surface of the αth termination port. Notice that the potential is constant at the surface of a conductor, since the terminals are assumed to be perfectly conducting.

Inside the source domain, we now select a reference point where we set the electric potential to be zero. With reference to this point, terminal α now has a potential $\hat{V}_\alpha$ and we may write

$$\int_{\mathbf{x}\in\partial\mathbb{D}^{\mathrm{s}}} \left(\hat{\mathbf{E}}^{\mathrm{bg}} \times \hat{\mathbf{H}}^{\mathrm{tot}} - \hat{\mathbf{E}}^{\mathrm{tot}} \times \hat{\mathbf{H}}^{\mathrm{bg}}\right) \cdot \boldsymbol{\nu}\, \mathrm{d}A = \sum_{\alpha=1}^{N} \left[\hat{V}_\alpha^{\mathrm{bg}} \hat{I}_\alpha^{\mathrm{tot}} - \hat{V}_\alpha^{\mathrm{tot}} \hat{I}_\alpha^{\mathrm{bg}}\right], \quad (3.67)$$

where $\hat{I}_\alpha$ is the electric current at the surface of the port of a conductor with constant voltage $\hat{V}_\alpha$.

The voltages at the terminals can be written as a product of the impedance matrix and the currents flowing through the terminals as

$$\hat{V}_\alpha = \sum_{\beta=1}^{N} \hat{Z}_{\alpha,\beta} \hat{I}_\beta. \quad (3.68)$$

If $\alpha = \beta$, $Z_{\alpha,\beta}$ is the self-impedance of the port/antenna, while for $\alpha \neq \beta$ the impedance $Z_{\alpha,\beta}$ is called the mutual impedance between antenna α and β. For the configuration considered here, it can be shown that the system is reciprocal, that is, $Z_{\alpha,\beta} = Z_{\beta,\alpha}$. This property implies the impedance matrix Z is symmetric.

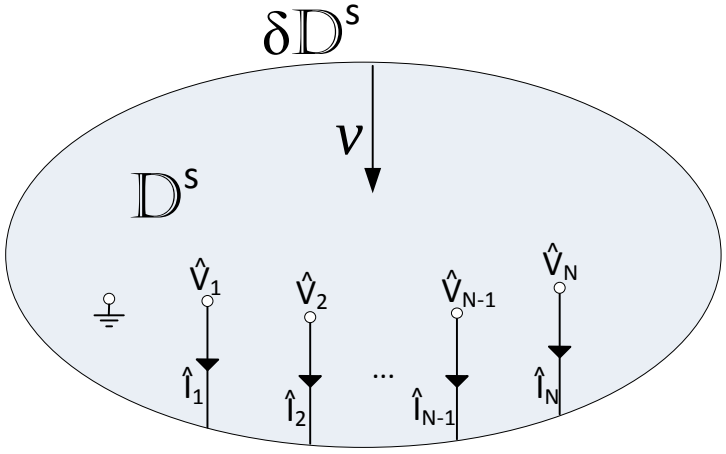

Figure 3.6: Source domain represented as ports, number of antennas/ports equals N.

Substituting Eq. (3.68) in the above equation and applying the symmetry of $Z_{\alpha,\beta}$, we obtain

$$\begin{aligned}\sum_{\alpha=1}^{N}\left[\hat{V}_{\alpha}^{\mathrm{bg}}\hat{I}_{\alpha}^{\mathrm{tot}}-\hat{V}_{\alpha}^{\mathrm{tot}}\hat{I}_{\alpha}^{\mathrm{bg}}\right]&=\sum_{\alpha=1}^{N}\sum_{\beta=1}^{N}\left[\hat{Z}_{\alpha,\beta}^{\mathrm{bg}}\hat{I}_{\beta}^{\mathrm{bg}}\hat{I}_{\alpha}^{\mathrm{tot}}-\hat{Z}_{\alpha,\beta}^{\mathrm{tot}}\hat{I}_{\beta}^{\mathrm{tot}}\hat{I}_{\alpha}^{\mathrm{bg}}\right],\\&=\sum_{\alpha=1}^{N}\sum_{\beta=1}^{N}\left[\hat{Z}_{\alpha,\beta}^{\mathrm{bg}}\hat{I}_{\beta}^{\mathrm{bg}}\hat{I}_{\alpha}^{\mathrm{tot}}-\hat{Z}_{\beta,\alpha}^{\mathrm{tot}}\hat{I}_{\alpha}^{\mathrm{tot}}\hat{I}_{\beta}^{\mathrm{bg}}\right],\\&=\sum_{\alpha=1}^{N}\sum_{\beta=1}^{N}\left[\hat{Z}_{\alpha,\beta}^{\mathrm{bg}}-\hat{Z}_{\alpha,\beta}^{\mathrm{tot}}\right]\hat{I}_{\alpha}^{\mathrm{tot}}\hat{I}_{\beta}^{\mathrm{bg}},\\&=\sum_{\alpha=1}^{N}\sum_{\beta=1}^{N}\delta\hat{Z}_{\alpha,\beta}\hat{I}_{\alpha}^{\mathrm{tot}}\hat{I}_{\beta}^{\mathrm{bg}},\end{aligned}\tag{3.69}$$

where we have introduced the change in the impedance matrix $\delta Z_{\alpha,\beta}$ as

$$\delta\hat{Z}_{\alpha,\beta}=\hat{Z}_{\alpha,\beta}^{\mathrm{bg}}-\hat{Z}_{\alpha,\beta}^{\mathrm{tot}}.\tag{3.70}$$

The right-hand side of Eq. (3.67) can now be replaced with this new result leading to

$$\sum_{\alpha=1}^{N}\sum_{\beta=1}^{N}\delta\hat{Z}_{\alpha,\beta}\hat{I}_{\alpha}^{\mathrm{tot}}\hat{I}_{\beta}^{\mathrm{bg}}=\int_{\mathbf{x}\in\mathbb{D}^{\mathrm{d}}}\left(-\delta\sigma\hat{\mathbf{E}}^{\mathrm{bg}}\cdot\hat{\mathbf{E}}^{\mathrm{tot}}+s\delta\mu\hat{\mathbf{H}}^{\mathrm{bg}}\cdot\hat{\mathbf{H}}^{\mathrm{tot}}\right)\mathrm{d}V.\tag{3.71}$$

To obtain an expression for the individual elements of $\delta Z_{\alpha,\beta}$, we take $\hat{I}_{\alpha}^{\mathrm{tot}}$ and $\hat{I}_{\beta}^{\mathrm{bg}}$ nonzero for $\alpha=f$ and $\beta=g$, $f,g\in\{1,2,...,N\}$, and set all other currents to zero. We then have

$$\delta\hat{Z}_{f,g}\hat{I}_{f}^{\mathrm{tot}}\hat{I}_{g}^{\mathrm{bg}}=\int_{\mathbf{x}\in\mathbb{D}^{\mathrm{d}}}\left(-\delta\sigma\hat{\mathbf{E}}^{\mathrm{bg}}\cdot\hat{\mathbf{E}}^{\mathrm{tot}}+s\delta\mu\hat{\mathbf{H}}^{\mathrm{bg}}\cdot\hat{\mathbf{H}}^{\mathrm{tot}}\right)\mathrm{d}V.\tag{3.72}$$

Finally, since the electromagnetic fields are linearly related to the currents, we may write

$$\begin{aligned}\hat{\mathbf{E}}^{\mathrm{bg}}&=\hat{\mathbf{e}}_{g}^{\mathrm{bg}}\hat{I}_{g}^{\mathrm{bg}},\\\hat{\mathbf{E}}^{\mathrm{tot}}&=\hat{\mathbf{e}}_{f}^{\mathrm{tot}}\hat{I}_{f}^{\mathrm{tot}},\\\hat{\mathbf{H}}^{\mathrm{bg}}&=\hat{\mathbf{h}}_{g}^{\mathrm{bg}}\hat{I}_{g}^{\mathrm{bg}},\\\hat{\mathbf{H}}^{\mathrm{tot}}&=\hat{\mathbf{h}}_{f}^{\mathrm{tot}}\hat{I}_{f}^{\mathrm{tot}},\end{aligned}\tag{3.73}$$

and Eq. (3.72) can be rewritten as

$$\delta\hat{Z}_{f,g}\hat{I}_{f}^{\mathrm{tot}}\hat{I}_{g}^{\mathrm{bg}}=\int_{\mathbf{x}\in\mathbb{D}^{\mathrm{d}}}\left(-\delta\sigma\,\hat{\mathbf{e}}_{g}^{\mathrm{bg}}\cdot\hat{\mathbf{e}}_{f}^{\mathrm{tot}}+s\delta\mu\,\hat{\mathbf{h}}_{g}^{\mathrm{bg}}\cdot\hat{\mathbf{h}}_{f}^{\mathrm{tot}}\right)\mathrm{d}V\,\hat{I}_{f}^{\mathrm{tot}}\hat{I}_{g}^{\mathrm{bg}}.$$

Since this equation should hold for any nonzero $\hat{I}_{f}^{\mathrm{tot}}$ and $\hat{I}_{g}^{\mathrm{bg}}$, we conclude that

$$\boxed{\delta\hat{Z}_{f,g}=\int_{\mathbf{x}\in\mathbb{D}^{\mathrm{c}}}\left(-\delta\sigma\,\hat{\mathbf{e}}_{g}^{\mathrm{bg}}\cdot\hat{\mathbf{e}}_{f}^{\mathrm{tot}}+s\delta\mu\,\hat{\mathbf{h}}_{g}^{\mathrm{bg}}\cdot\hat{\mathbf{h}}_{f}^{\mathrm{tot}}\right)\mathrm{d}V.}\tag{3.74}$$

This equation relates the change in the impedance to the presence of a defect. If no defect is present, then $\delta\sigma = 0$ and $\delta\mu = 0$ and clearly $\delta\hat{Z}_{f,g} = 0$ as well.

To put the above formula into action, suppose that we have two antennas present in our configuration. One antenna acts as a receiver ($f = \mathrm{rx}$), while the other one acts as a source ($g = \mathrm{tx}$). Then the impedance difference between these two antennas can be found by finding the electromagnetic fields inside the crack. Specifically, the vectors fields $\hat{\mathbf{e}}_{\mathrm{tx}}^{\mathrm{bg}}, \hat{\mathbf{h}}_{\mathrm{tx}}^{\mathrm{bg}}$, $\hat{\mathbf{e}}_{\mathrm{rx}}^{\mathrm{tot}}$, and $\hat{\mathbf{h}}_{\mathrm{rx}}^{\mathrm{tot}}$ have to be found inside the domain $\mathbb{D}^{\mathrm{d}}$ occupied by the defect. These fields can be interpreted as follows:

$\hat{\mathbf{e}}_{\mathrm{tx}}^{\mathrm{bg}}, \hat{\mathbf{h}}_{\mathrm{tx}}^{\mathrm{bg}}$ is essentially the electromagnetic background field inside $\mathbb{D}^{\mathrm{d}}$ in case there is no defect present inside this domain,

$\hat{\mathbf{e}}_{\mathrm{rx}}^{\mathrm{tot}}, \hat{\mathbf{h}}_{\mathrm{rx}}^{\mathrm{tot}}$ is essentially the electromagnetic field inside the crack if the receiver would act as a the transmitter.

These fields have been derived in Section 3.2 and are given given in Table 3.1 and Eqs. (3.54) and (3.55). However, in many cases of practical interest the defect is small (crack) compared to the wavelengths of operation and the Born approximation may be applied. In this approximation, the total field inside the defect is approximated by the background field, i.e., $\hat{\mathbf{e}}^{\mathrm{tot}} \approx \hat{\mathbf{e}}^{\mathrm{bg}}$ and $\hat{\mathbf{h}}^{\mathrm{tot}} \approx \hat{\mathbf{h}}^{\mathrm{bg}}$. Using this approximation, the above equation becomes

$$\delta\hat{Z}_{\mathrm{f,g}} = \int_{\mathbf{x}\in\mathbb{D}^{\mathrm{d}}} \left\{ -\delta\sigma\, \hat{\mathbf{e}}_g^{\mathrm{bg}} \cdot \hat{\mathbf{e}}_f^{\mathrm{bg}} + s\delta\mu\, \hat{\mathbf{h}}_g^{\mathrm{bg}} \cdot \hat{\mathbf{h}}_f^{\mathrm{bg}} \right\} \mathrm{d}V \tag{3.75}$$

and there is no need anymore to determine the total field inside the defect.

A change in impedance over two antennas is not precisely what is measured by the system. Voltages are measured instead and it is therefore convenient to rewrite the change in impedance formula (3.74) in terms of voltages.

To this end, we return to the N-port description (Eq. (3.68))

$$\begin{bmatrix} \hat{V}_1 \\ \hat{V}_2 \\ \vdots \\ \hat{V}_N \end{bmatrix} = \begin{bmatrix} \hat{Z}_{11} & \hat{Z}_{12} & \cdots & \hat{Z}_{1N} \\ \hat{Z}_{21} & \hat{Z}_{22} & \cdots & \hat{Z}_{2N} \\ \vdots & \vdots & \ddots & \vdots \\ \hat{Z}_{N1} & \hat{Z}_{N2} & \cdots & \hat{Z}_{NN} \end{bmatrix} \begin{bmatrix} \hat{I}_1 \\ \hat{I}_2 \\ \vdots \\ \hat{I}_N \end{bmatrix} \tag{3.76}$$

and consider a system consisting of four ports ($N = 4$). The first port represents the transmitter, while the other three act as receivers. Now the voltage at receiver 3, for example, is given by

$$\hat{V}_3 = \hat{Z}_{31}\hat{I}_1 + \hat{Z}_{32}\hat{I}_2 + \hat{Z}_{33}\hat{I}_3 + \hat{Z}_{34}\hat{I}_4. \tag{3.77}$$

Since the voltage at port 3 needs to be determined, the transfer from port 1 to port 3 needs to be found. This can be done by setting $\hat{I}_2$, $\hat{I}_3$ and $\hat{I}_4$ to zero. Solving for $\hat{Z}_{31}$ then gives us

$$\hat{Z}_{31} = \frac{\hat{V}_3}{\hat{I}_1}, \qquad (\hat{I}_2, \hat{I}_3, \hat{I}_4 = 0). \tag{3.78}$$

When there is a crack or weak spot in the roll, a change in impedance will occur and therefore also a change in the voltage at the receiver ($\hat{V}_3$). These quantities

are linearly related via Ohm's law and therefore

$$\hat{Z}_{31}^{\mathrm{bg}} - \hat{Z}_{31}^{\mathrm{tot}} = \frac{\hat{V}_3^{\mathrm{bg}} - \hat{V}_3^{\mathrm{tot}}}{\hat{I}_1},$$

which is equal to

$$\delta\hat{Z}_{31} = \frac{\delta\hat{V}_3}{\hat{I}_1}. \tag{3.79}$$

Generalizing this approach to arbitrary ports of an N-port system, we have

$$\frac{\delta\hat{V}_{\mathrm{f}}}{\hat{I}_{\mathrm{g}}} = \int_{\mathbf{x}\in\mathbb{D}^{\mathrm{c}}} \left\{ -\delta\sigma\, \hat{\mathbf{e}}_{\mathrm{g}}^{\mathrm{bg}} \cdot \hat{\mathbf{e}}_f^{\mathrm{tot}} + s\delta\mu\, \hat{\mathbf{h}}_{\mathrm{g}}^{\mathrm{bg}} \cdot \hat{\mathbf{h}}_{\mathrm{f}}^{\mathrm{tot}} \right\} \mathrm{d}V. \tag{3.80}$$

3.4 Limitation of the model

In Section 3.2, expressions for the electromagnetic fields have been derived for a small loop antenna in vacuum, for a loop antenna above a roll, and for an antenna above a roll with a possible defect. Section 3.3 covered the derivation of the theoretical models that we will use in our experimental studies. Before doing so, however, it is important to realize that some assumptions have been made in deriving these models. These assumptions are:

1. The electromagnetic fields given in Eqs. (3.19), (3.20), (3.28), (3.29), (3.54), and (3.55) have neglected the intermediate- and far field terms caused by a source. This assumption has been made because the wavelengths in free space are much larger than the dimensions of the measurement setup. Therefore these terms become negligible compared to the near-field term [3].

2. The antennas in the original setup used by Lismar are square loop-antennas. Within this work, these antennas have been modeled as magnetic dipoles to ease the calculations. The far field of an electrically small square loop-antenna is identical to that of an electrically small circular loop-antenna and a magnetic dipole [3]. The near field, however, will probably differ and should be investigated in future work. For example, the near field of a square loop-antenna can be modeled as four magnetic dipoles (see [35]). This field can therefore be computed using the results presented in this thesis without a lot of additional effort.

   Furthermore, antennas that are close to each other have some mutual coupling which has not been been taken into account. However, using the double integral Neumann formula [36], it follows this effect can be neglected as it is close to zero.

3. The derivation for the background field that is presented in Table 3.1 has as a starting point the assumption that the roll is a conductive half space, implying that the cylindrical shape of the roll has been neglected. This is assumed because the antennas are really close to the roll (0.5 mm) and its curvature can therefore be neglected.

Chapter 4

Application of the field and impedance model

This chapter discusses eddy currents in clean rolls and rolls containing a defect. For a roll that does not contain any flaws, non-disturbed eddy currents should form inside the metal. This will be shown by using derivations from last chapter and by the use of the simulation program Comsol Multiphysics. Hereafter, defects will be further examined by introducing a small crack in the shape of an ellipsoid and the question will be answered why some cracks are easily found while others are not.

4.1 Eddy currents in a clean roll

This section is divided in two parts. In the first part we investigate the attenuation of the electromagnetic field inside the roll as function of the skin-depth. Using this function, the surface currents can be found by pushing the skin-depth to zero. Using a new derived equation for these currents, we are able to partly validate the background field derived in last chapter. The second part starts with a skin-depth which is not equal to zero, after which the fields in the roll

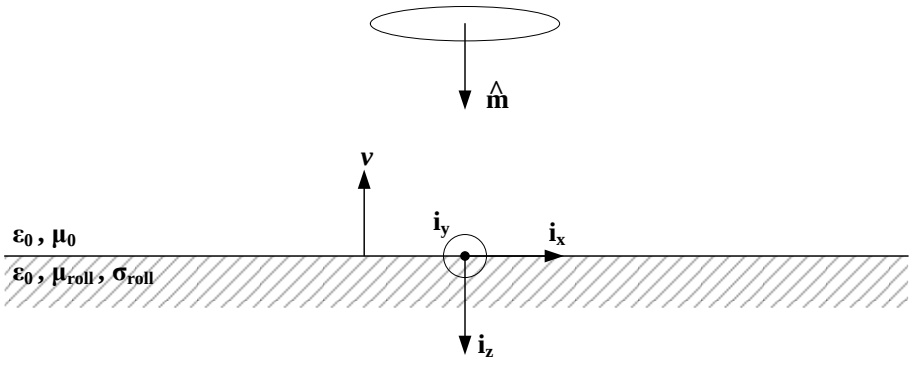

Figure 4.1: Magnetic dipole placed above a roll, $\boldsymbol{\nu} = -\mathbf{i}_z$ is a unit vector perpendicular to the surface.

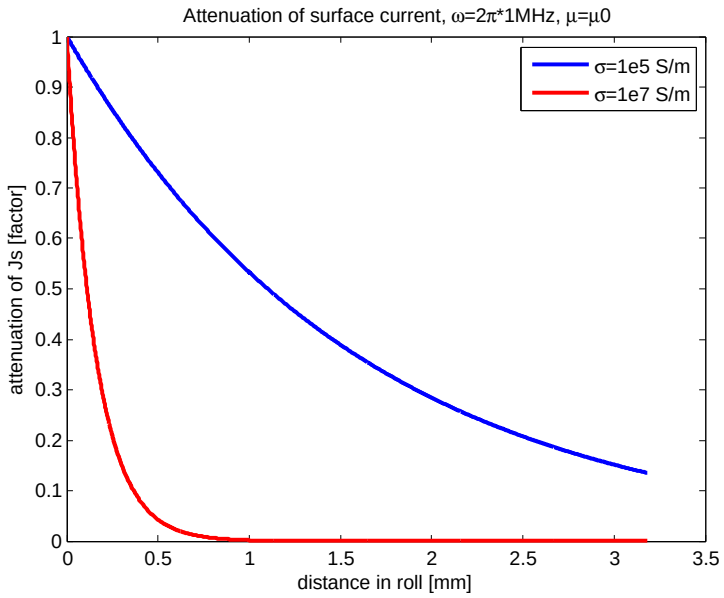

Figure 4.2: Skin depth for f=1 MHz, $\mu = \mu_0$, and for two different conductivities, namely, σ=10^5 S/m and σ=10^7 S/m.

are evaluated with the use of Comsol and the derived theory.

4.1.1 Surface currents

Consider the setup illustrated in Figure 4.1. Here, a small current carrying wire is placed above a roll. In the roll there will be induced currents due to the magnetic fields of this antenna and the currents at the surface are called surface currents ($\mathbf{J}_\mathrm{s}$). Each field penetrating the roll attenuates with distance depending on the material characteristics of the roll. In general, this relation can be given in terms of the skin-depth as [29]

$$\mathbf{J} = \mathbf{J}_\mathrm{s} e^{-\frac{|\mathbf{x}|}{\delta_\mathrm{s}}}, \quad \text{where the skin-depth } \delta_s = \sqrt{\frac{2}{\omega\sigma\mu}}. \tag{4.1}$$

This relation implies that the skin-depth becomes really small for a high conductivity, high permeability, or high frequencies. As a consequence, for such small values, the currents attenuate really fast over distance. For comparison, Figure 4.2 illustrates one case in which the conductivity is equal to 10^5 S/m and the other for $\sigma = 10^7$ S/m. This attenuation is also seen in the expressions for the background field listed in Table 3.1 through the factor $e^{-\gamma_\mathrm{b} z}$, in which γ_b is dependent on the material properties.

For a perfect electric conductor (PEC) the conductivity is infinitely large ($\sigma \to \infty$). This means that all the currents are concentrated at the surface. In this special case, the surface currents are given by

$$\hat{\mathbf{J}}_\mathrm{s}(x,y) = \begin{bmatrix} 6yh \\ -6xh \\ 0 \end{bmatrix} \frac{\hat{K}_z^1}{4\pi|\mathbf{x}-\mathbf{x}^s|^5}, \quad [\mathrm{A/m}] \tag{4.2}$$

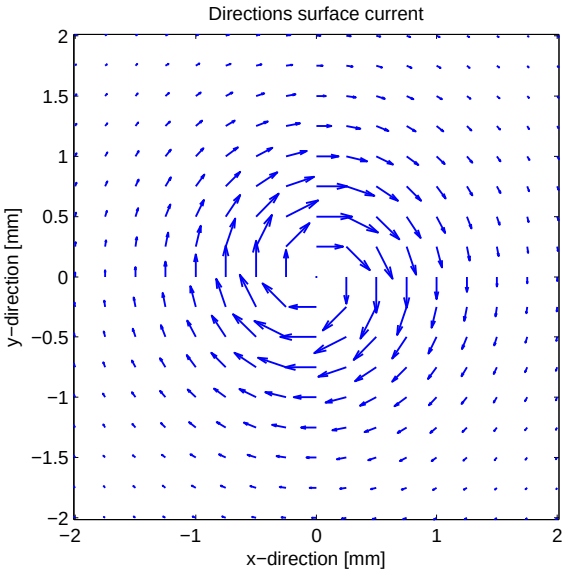

(a) Directions of $\hat{\mathbf{J}}_s$

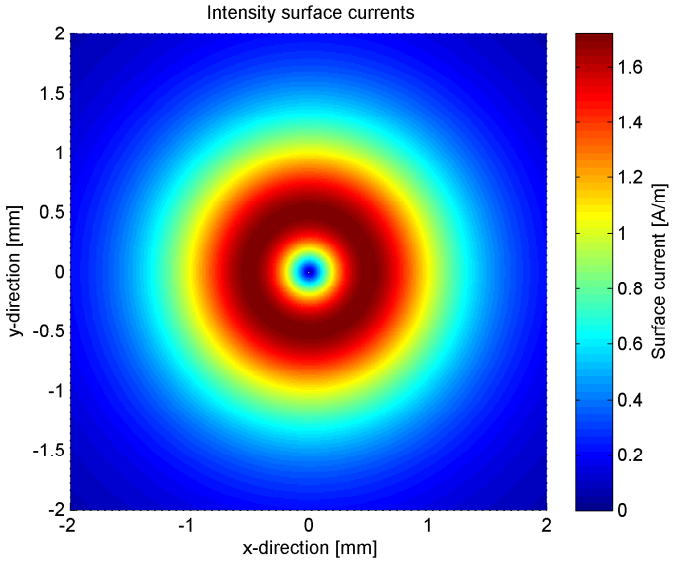

(b) Intensity of $\hat{\mathbf{J}}_s$

Figure 4.3: Surface currents found with Equation 4.2. Magnetic dipole is located at point (0,0). The left figure illustrates the directions of the currents while the right shows the intensity of these currents.

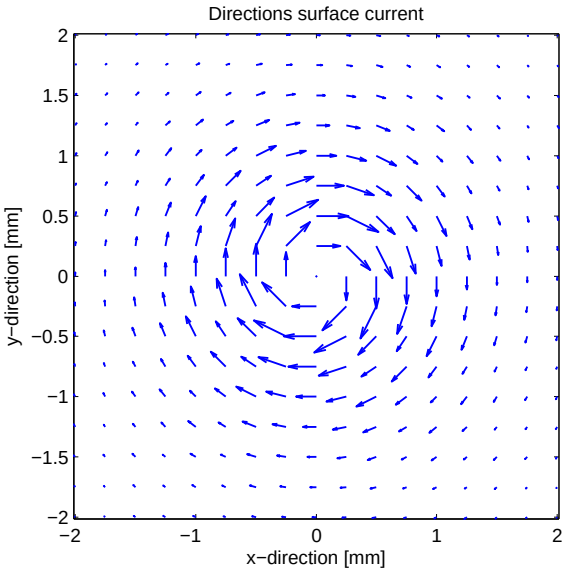

(a) Directions of $\hat{\mathbf{J}}_s$

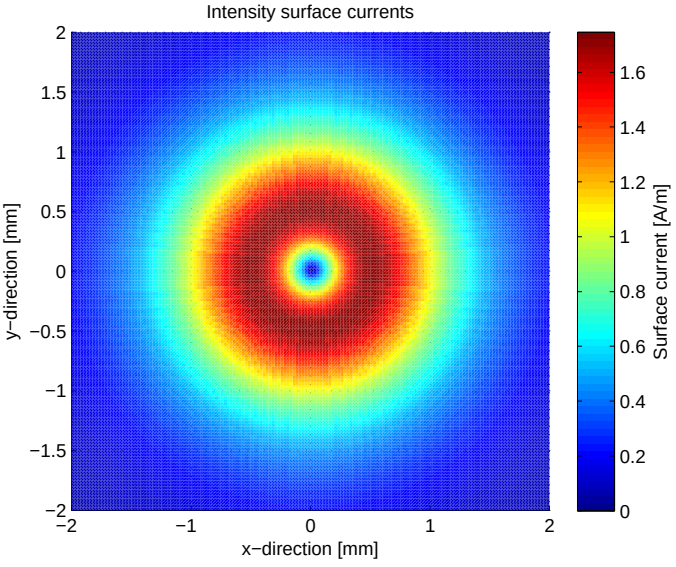

(b) Intensity of $\hat{\mathbf{J}}_s$

Figure 4.4: Surface currents found with background field. Magnetic dipole is located at point (0,0) and the magnetic field is evaluated at $z = 10^{-30}$ m. The left figure illustrates the directions of the currents while the right shows the intensity of these currents.

with $z = 0$, and in which $\hat{K}_z^1 = I(s)A$, where I is the current through the winding, A is the cross section of the loop, and h is the height of the antenna. This equation is derived in Appendix C. The currents are obviously tangential to the surface, since $\mathbf{J}_s$ only has a x- and y-components.

The surface currents have been plotted in Figure 4.3 for $h = 1$ mm, $I = 1$ mA, and a cross section of $\pi(2 \cdot 10^{-6})$ m^2. The magnetic dipole is located at the point $(0, 0)$ and is evaluated for a total surface of 16 mm^2. The left-hand side of Figure 4.3 illustrates the directions of the currents, whereas the right-hand side figure illustrates the intensity of the currents. Clearly, the currents are running in circles on the surface of the roll. Hence, these currents are named eddy currents.

The background field derived in Subsection 3.2.2 should provide equally like outcomes as the surface currents derived in Appendix C. Because these latter derivations assume an infinitely large conductivity, a high conductivity will be chosen for the background field. As the electric field is approaching zero at the surface for a high conductivity, the magnetic field is used to find the currents. This field is evaluated just below the surface and its result is shown in Figure 4.4. The graphs are identical to each other including the magnitude of the surface currents.

4.1.2 Evaluating the fields inside the roll

The electromagnetic fields will penetrate the steel when the conductivity and permeability do not approach infinity. To see what fields are produced by a magnetic dipole placed above steel (see Figure 4.1), we will evaluate the derived background field from Subsection 3.2.2 for different depths. For validation and comparison reasons, the same setup has been built in Comsol Multiphysics from which we should see similar trends regarding the fields. In Comsol, the roll is built in two dimensions, which is reasonable since the roll has large dimensions in the x- and y-directions. Figure 4.5 illustrates this procedure. The configuration is extended to infinity in both directions on the condition that there is no variation in these directions.

We will consider a roll with a conductivity of 10^8 S/m and a permeability equal to vacuum for depths 0.05 mm, 0.10 mm, and 0.15 mm. The electric field component E_y that is tangential to the steel and the magnetic fields H_z

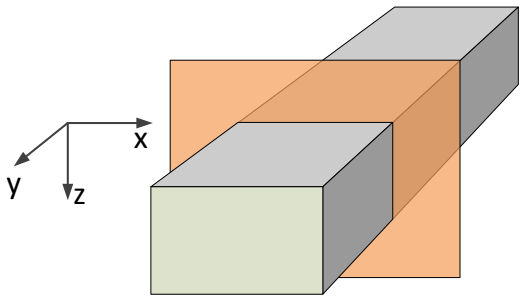

Figure 4.5: Comsol extends the configuration in y-direction to infinity in both directions, such that 3D objects can be modeled as 2D objects by taking a slice.

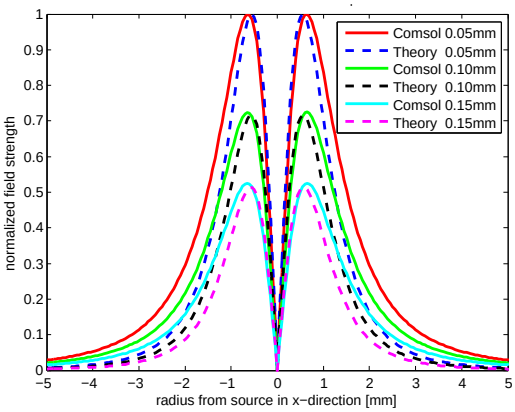

(a) Electric field E_y for σ=10^8 S/m, $\mu = \mu_0$.

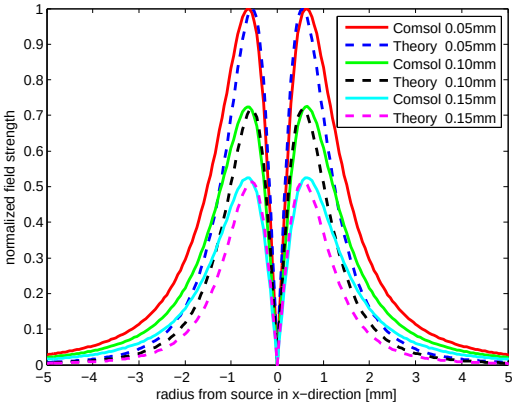

(b) Magnetic field H_x for σ=10^8 S/m, $\mu = \mu_0$.

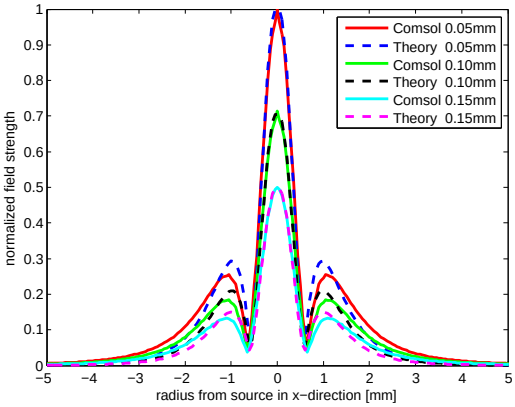

(c) Magnetic field H_z for σ=10^8 S/m, $\mu = \mu_0$.

Figure 4.6: Normalized fields for different depths and medium parameters. Results from Comsol are depicted by solid lines, the theory with dashed lines.

perpendicular- and H_x tangential to the steel, are separately plotted in Figures 4.6a, 4.6b, and 4.6c respectively. The results have been normalized to the maximum of the strongest field as the amplitudes from Comsol and the theory are different. The difference in magnitude results from the fact that an ideal dipole source (Dirac distribution) cannot be modeled exactly in a numerical code such as Comsol. However, both Comsol and the theory give similar results for conductive media. In all sub-figures, the attenuation of the fields in depth, and horizontal distance, is the same. The diffusion of the waves in the medium can clearly be seen as the fields tend to attenuate when distancing from the source.

The simulation in Comsol has also been applied for media with a permeability not equal to that of vacuum. However, this causes some deviations with respect to the derived background field equations. More precisely, the attenuation of the field over distance in the x-direction differs. Further validation by simulating 3D in Comsol is recommended for future work, as these differences are probably caused by the way the source is implemented in Comsol.

4.2 Defects in a roll

The section is divided in two parts. The first part will use the simulation program Comsol Multiphysics to illustrate the disturbance of currents due to a rectangular crack, with different orientations with respect to the eddy currents. Hereafter, an equation is derived which models a small ellipsoid in a homogenous medium. Using this model, it becomes clear why some cracks are found and other are not. The second part will cover the change in impedance caused by a defect with the use of the impedance model presented in Eq. (3.74).

4.2.1 Disturbance of currents

In Comsol Multiphysics, a simple 3D setup is built which can be used to get insight in the disturbance of eddy currents due to cracks. We consider a magnetic dipole that is located above the center of a highly conductive plate containing a rectangular crack. This crack can have different orientations with respect to the eddy currents. Two extreme cases are distinguished, namely, one in which the long side of a crack runs parallel to the currents, and one in which a crack is perpendicularly oriented with respect to the currents. The crack has been cut out from the plate and is filled with air.

Both cases are illustrated in Figure 4.7. The top two figures show the eddy currents for a crack that is oriented parallel to the currents, whereas the bottom two illustrate eddy currents for a crack perpendicular to the currents. The cones in these figures indicate the direction of the eddy currents and the colors their intensity. We observe that the eddy currents are much more perturbed in the perpendicular case as more current has to change route in this case. In this example, the modeled crack is quite large and will most-likely be detected in both scenarios. However, as the size of the cracks becomes smaller, the eddy currents will hardly be affected by the parallel crack, while the perpendicular crack can still cause dramatic changes in the eddy current pattern. We therefore conjecture that small parallel cracks are much more difficult to detect than cracks which are perpendicularly oriented.

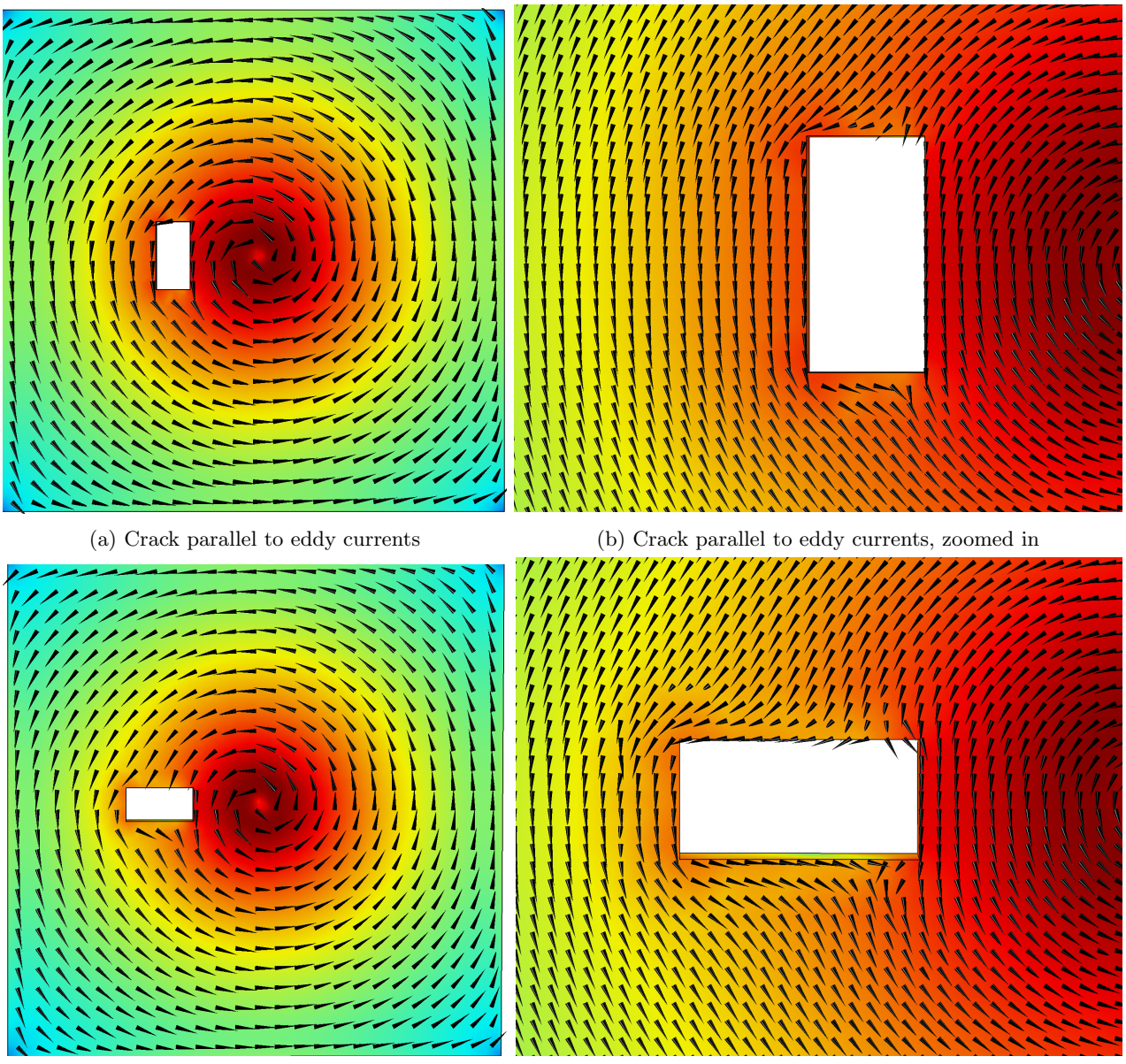

(a) Crack parallel to eddy currents

(b) Crack parallel to eddy currents, zoomed in

(c) Crack perpendicular to eddy currents

(d) Crack perpendicular to eddy currents, zoomed in

Figure 4.7: Two different orientations of the cracks. Perpendicular cracks disturb the currents more than parallel cracks.

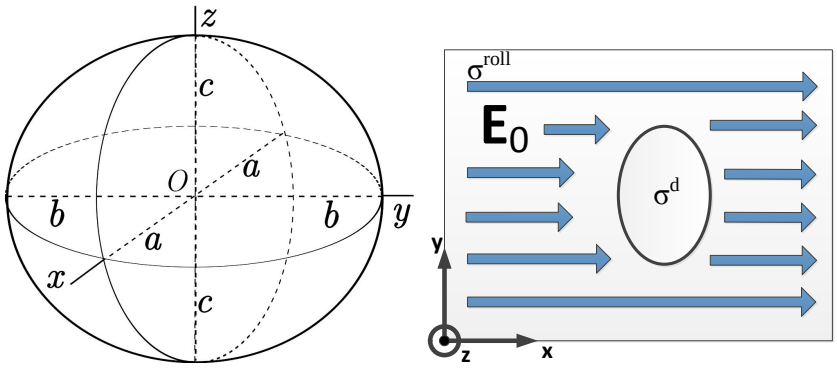

(a) (b)

Figure 4.8: Ellipsoid in a Cartesian coordinate system on the left, where parameters a, b and c are free to choose and determine the shape of the object. On the right, an ellipsoid placed in a uniform external electric field. The medium has a conductivity σ^{roll} and the ellipsoid a conductivity σ^{d}.

By modeling the crack as an ellipsoid, it can be shown that this is indeed the case. Specifically, let us take an ellipsoid filled with a homogeneous and isotropic material that is characterized by a constant conductivity σ^{d}. Its shape is determined by the parameters a, b, and c as illustrated in Figure 4.8a. We embed this ellipsoid in a homogeneous and isotropic background medium with conductivity σ^{roll} and we assume that an external field $\mathbf{E}_0$ is present in this background material (see Figure 4.8b.) Denoting the field inside the ellipsoid by $\mathbf{E}^{\text{in}}$, it can be shown that [31]

$$\mathbf{E}^{\text{in}}(\mathbf{x}) = (1 + \mathbf{L}\frac{\delta\sigma}{\sigma^{\text{roll}}})^{-1}\mathbf{E}_0(\mathbf{x}). \tag{4.3}$$

Here $\delta\sigma = \sigma^{\text{d}} - \sigma^{\text{roll}}$ and $\mathbf{L}$ is the depolarization factor. This factor is actually a diagonal dyadic with diagonal elements L_x, L_y, and L_z. These factors relate the external field to the field in the ellipsoid and add up to one. A special case of the ellipsoid is a spheroid for which $a = c$, implying $L_x = L_z$ (see Figure 4.8a). Using this shape, only the L_y factor remains in integral form given by [32]

$$L_y = \frac{g}{2}\int_{-1}^{1} \frac{u^2}{1-(1-g)u^2}du, \qquad \text{where } g = \left(\frac{a}{b}\right)^2, \tag{4.4}$$

and

$$L_x = L_z = \frac{1 - L_y}{2}. \tag{4.5}$$

For the case $b >> a = c$, the spheroid takes the form of a needle and is oriented perpendicular to the x-directed electric field. Therefore, $g \approx 0$ and consequently $L_y = 0$ and $L_x = L_z = 1/2$. Using Eq. (4.3) with $\sigma^{\text{d}} = 0$, the field inside the ellipsoid becomes

$$\begin{bmatrix} E_x^{\text{in}} \\ E_y^{\text{in}} \\ E_z^{\text{in}} \end{bmatrix} = \begin{bmatrix} 2 & 0 & 0 \\ 0 & 1 & 0 \\ 0 & 0 & 2 \end{bmatrix} \begin{bmatrix} E_0 \\ 0 \\ 0 \end{bmatrix} = \begin{bmatrix} 2E_0 \\ 0 \\ 0 \end{bmatrix}. \tag{4.6}$$

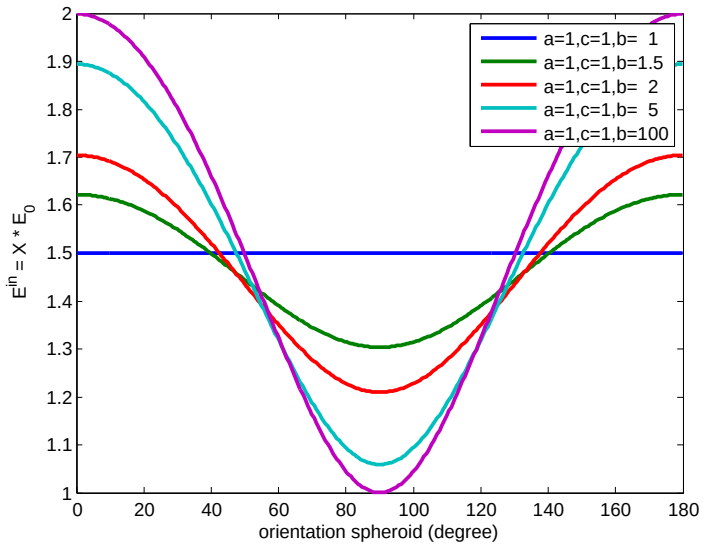

(a) Rotated for different values of b, with constant $a = c = 1$.

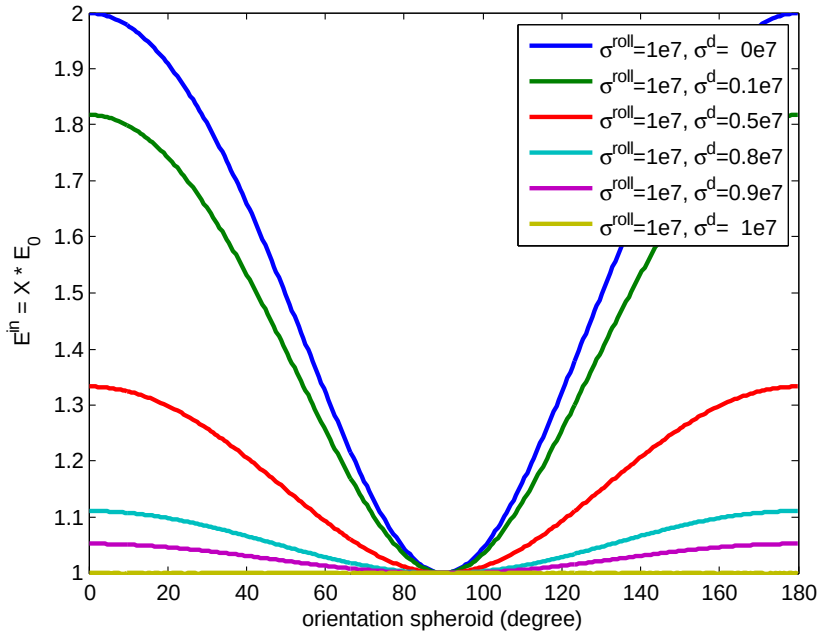

(b) Rotated for different values of σ, $a = c = 1, b = 100$.

Figure 4.9: The spheroid is rotated 180 degrees for different shapes (a) and different conductivities (b), the factor X is shown in the plots, i.e. $\mathbf{E}^{\text{in}} = \text{X}\mathbf{E}_0$.

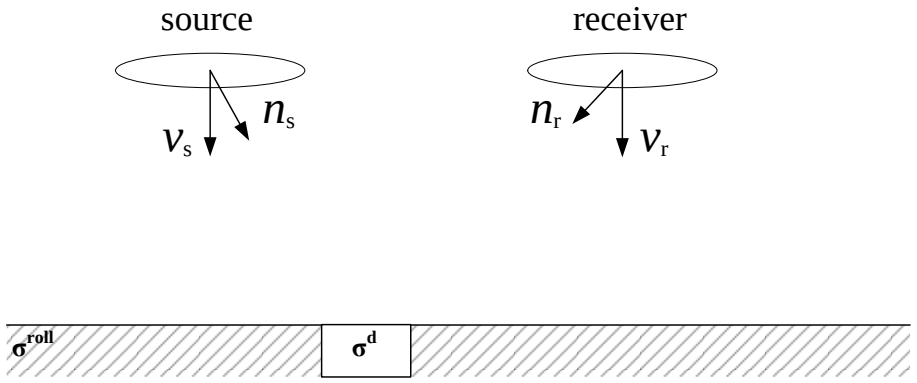

Figure 4.10: Two antennas above a roll. The unit vectors $\boldsymbol{\nu}_{\mathrm{n}}$ and $\mathbf{n}_{\mathrm{n}}$ are shown as well. The former is a unit vector orthogonal to the surface of the loop, the latter is a unit vector pointing towards the defect.

The field inside the ellipsoid becomes twice as large as the background field. Such a crack can be found easily by a measurement system. Now, imagine that the crack is rotated by 90 degrees and becomes parallel to the electric field. Following a similar analysis as before, we now get

$$\begin{bmatrix} E_x^{\mathrm{in}} \\ E_y^{\mathrm{in}} \\ E_z^{\mathrm{in}} \end{bmatrix} = \begin{bmatrix} 1 & 0 & 0 \\ 0 & 2 & 0 \\ 0 & 0 & 2 \end{bmatrix} \begin{bmatrix} E_0 \\ 0 \\ 0 \end{bmatrix} = \begin{bmatrix} E_0 \\ 0 \\ 0 \end{bmatrix}. \tag{4.7}$$

Now, the field inside the spheroid is the same as the background field. Hence, it cannot be found as it does not disturb the field. In Figure 4.9a some different shapes of the spheroid versus orientation are plotted with respect to the background field. Figure 4.9b shows a needle perpendicular to the electric field for some different values of $\delta\sigma$.

4.2.2 Change in the impedance due to a crack

In Section 3.3, a model has been derived for impedance variations due to contrasts with respect to the background field. For convenience, this equation is repeated here as

$$\delta\hat{Z}_{f,g} = \int_{\mathbf{x}\in\mathbb{D}^{\mathrm{d}}} \left(-\delta\sigma\, \hat{\mathbf{e}}_g^{\mathrm{bg}} \cdot \hat{\mathbf{e}}_f^{\mathrm{tot}} + s\delta\mu\, \hat{\mathbf{h}}_g^{\mathrm{bg}} \cdot \hat{\mathbf{h}}_f^{\mathrm{tot}} \right) \mathrm{d}V. \tag{4.8}$$

As mentioned earlier, the Born approximation can be used to approximate the total field by the background field if the defect is sufficiently small. However, the background field is still required in this case and this can be a computationally intensive task.

In this section, we therefore follow an alternate route and approximate the electromagnetic field by the quasi-static field. The background field derived in Subsection 3.2.2 is not used in this alternate route. For simplicity, we consider defects with no contrast in the permeability and a configuration consisting of a single transmitter and single receiver (see Figure 4.10). In Appendix D, it is

shown that within a quasi-static field approximation, the change in the mutual impedance between these two antennas is given by

$$\delta\hat{Z} = (\omega\mu_0 A)^2 \int_{\mathbf{x}\in\mathbb{D}^{\mathrm{d}}} \frac{\delta\sigma}{16\pi^2|\mathbf{x}-\mathbf{x}_{\mathrm{s}}|^2|\mathbf{x}-\mathbf{x}_{\mathrm{r}}|^2} \left[(\mathbf{n}_{\mathrm{s}}\cdot\mathbf{n}_{\mathrm{r}})(\boldsymbol{\nu}_{\mathrm{s}}\cdot\boldsymbol{\nu}_{\mathrm{r}}) - (\mathbf{n}_{\mathrm{s}}\cdot\boldsymbol{\nu}_{\mathrm{r}})(\boldsymbol{\nu}_{\mathrm{s}}\cdot\mathbf{n}_{\mathrm{r}})\right] \mathrm{d}V, \tag{4.9}$$

where $\mathbf{n}_{\mathrm{n}} = \frac{\mathbf{x}-\mathbf{x}_n}{|\mathbf{x}-\mathbf{x}_n|}$ is a unit vector pointing from the transmit or receive antenna (n=s or n=r) towards the point that is evaluated ($\mathbf{x} \in \mathbb{D}^{\mathrm{d}}$), $\boldsymbol{\nu}_{\mathrm{n}}$ is the unit vector perpendicular to the area of the loop-antenna, and ω is the frequency of operation. These unit vectors are depicted in Figure 4.10.

Equation (4.9) shows that the impedance variations are caused purely by geometrical changes in the system, such as the distances and directions from the antenna to a contrast point. Furthermore, because we said there is no contrast in permeability, the expression gives just solutions for the resistive part of the impedance variations. For higher frequencies there will also be higher order terms. We did not incorporate these terms in the quasi-static approach as their influence on the impedance is minimal for low frequencies. If these higher order terms where incorporated, there would also be a reactive part caused by changes in conductivity.

To see what kind of results this equation gives, we first have to note that the orientation of the crack with respect to the eddy currents is not yet included. Therefore, we will consider a hole in the form of a sphere which is orientation independent (see Subsection 4.2.1). Now suppose we have two antennas which are placed horizontally next to each other at 1.5 mm height above a steel plate, this plate contains a crack with a volume 10^{-3} mm^3 at some location. The distance between the midpoints of the antennas is 4.5 mm and they transmit a frequency of 100 kHz. The antenna pair is scanning the plate vertically, where every time the end of the plate is reached it starts over some horizontally distance further. This process is illustrated in Figure 4.11. The impedance variations

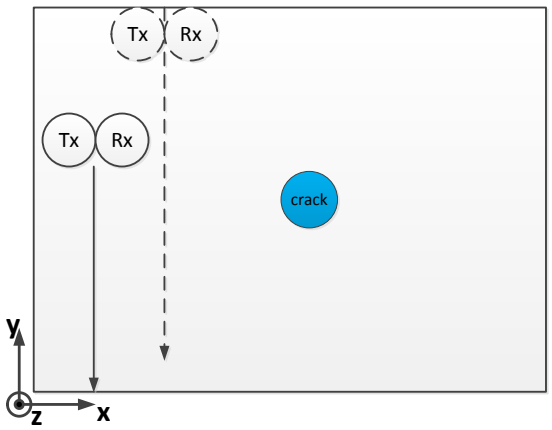

Figure 4.11: The transmitter and receiver are scanning the steel plate vertically, where every time the end of the plate is reached it starts over some horizontally distance further.

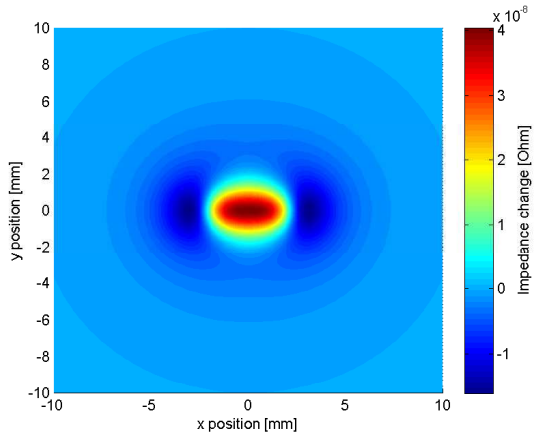

(a) Antennas horizontally aligned, xy-plot

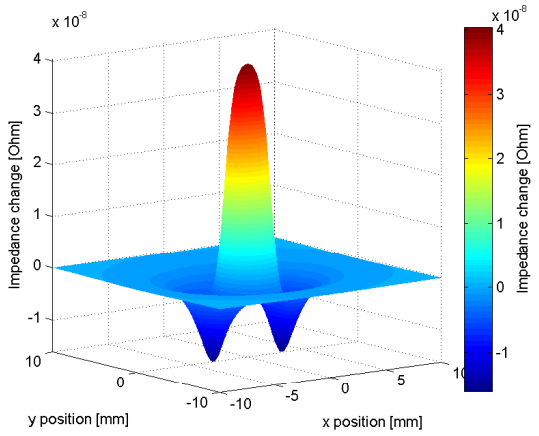

(b) Antennas horizontally aligned, xyz-plot

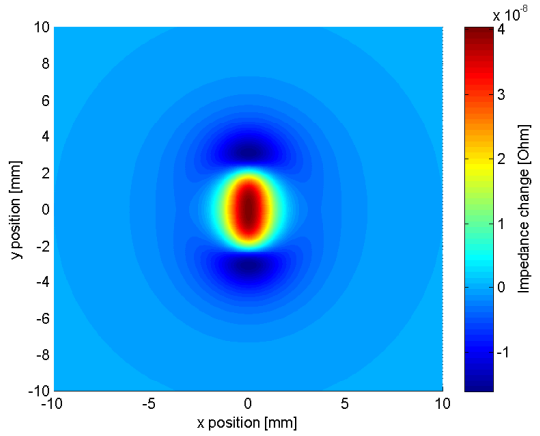

(c) Antennas vertically aligned

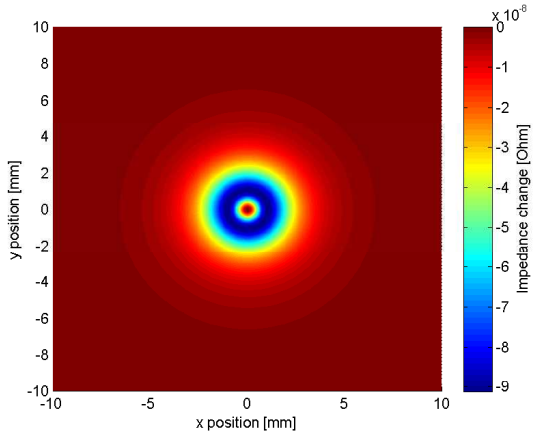

(d) Antennas in a monostatic configuration

Figure 4.12: Impedance variation plot for a scan over a steel plate containing a spherical crack at location (0,0), for bistatic and monostatic configuration.

can now be measured by taking samples during the scan using Eq. (4.9).

The result of this scan is shown in Figure 4.12a and 4.12b where the xy-axes determine the location where a sample has been taken, and the z-axis determines the variation in impedance. Upon approaching a defect, the change in the impedance first decreases a bit but shortly after increases significantly. This alternation is due to the multiplication of the unit vectors $\mathbf{n}_\mathrm{s}$ and $\mathbf{n}_\mathrm{r}$ as these flip sign as soon as one antenna has moved over the defect already while the other has not. The strongest signal is achieved if the crack is in between the two antennas. Furthermore, the shape of the sphere cannot be recognized because it is stretched in the horizontal direction due to the distance between the horizontally oriented antennas. This distance causes the sensitivity region between the antennas to be stretched as well. For small cracks with respect to this distance, the impedance variation is a rough copy of the sensitivity region. Therefore, this distance can be said to determine the resolution of the scanning

system for some part.

The same scan can be made by antennas which are oriented differently towards each other. For example, in Figure 4.12c we have made a scan with two antennas placed vertically towards each other. The difference is that the image is rotated by 90 degrees, which is expected as the antennas have been rotated by 90 degrees as well and the crack is modeled as a sphere. If the scan is made with the antennas in monostatic configuration, the result from Figure 4.12d is obtained. Here, we observe a circle in which the dark blue peak of this circle corresponds with the most sensitive part of the antenna system. This fits the theory, as the eddy currents induced by our source are rotationally symmetric.

To include the orientation of the crack with respect to the eddy currents, we create an oblate spheroid with a width that is twice as large as its length (i.e. $b = 2$ and $a = c = 1$) and dimensions much smaller than the wavelength. The total electric field term in Eq. (4.8) is now influenced by the orientation of the crack via Eq. (4.3).

Illustrated in Figure 4.13 are four enlarged cracks with a different orientation which we would like to detect. One scan is made with a bistatic configuration where the antennas are horizontally aligned, while the other scan is made in a monostatic configuration. The scanning results are shown in Figures 4.14a and Figure 4.14b, respectively. Clearly, the best detections for a horizontally aligned antenna system are obtained for a horizontally oriented crack , since in this case the eddy currents are maximally disturbed. The vertically oriented spheroid disturbs the eddy currents less and as a consequence shows a lower variation in impedance. The variation for diagonal oriented spheroids is somewhere in between.

The orientation of the cracks can be found in a monostatic measurement setup. This is because the eddy currents are disturbed most when the crack is perpendicular to these currents. In case of a horizontal oriented crack this occurs when the antennas are located on the left and on the right side of this crack, which causes the currents to be perpendicular to the long side of the crack. We also see some impedance deviations in case the antenna is located above and below the crack. This is due to the fact the currents are disturbed as well by the short side of the defect, but to a much smaller extend. For other

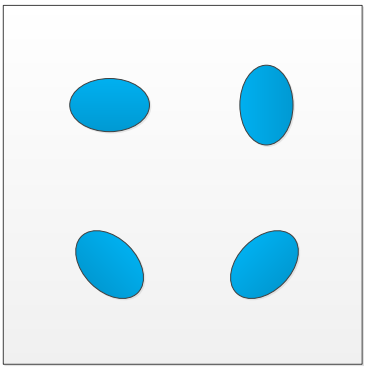

Figure 4.13: Four spheroid cracks with $b = 2$ and $a = c = 1$ are placed in a steel plate, all four have a different orientation.

oriented cracks the same analysis applies as can be seen in the figure.

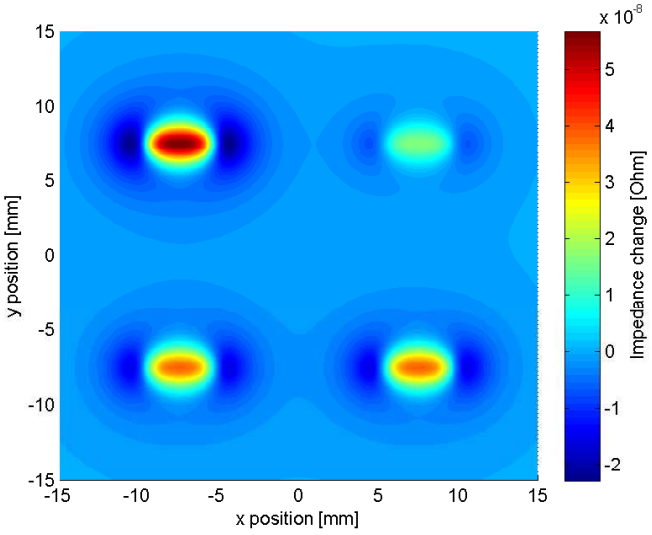

(a) Antennas horizontally aligned

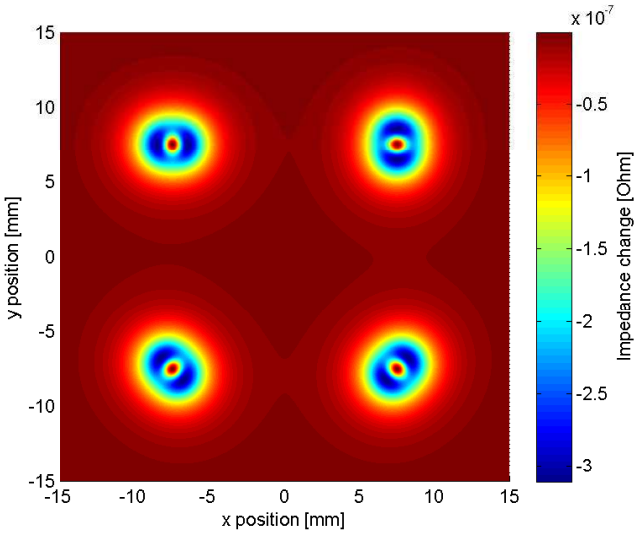

(b) Antennas in a monostatic configuration

Figure 4.14: Impedance variation plot for a scan over a steel plate containing four holes at different locations with different orientations.

Chapter 5

Imaging

In this chapter we discuss the construction of an imaging operator that can be applied on measured NDT data to construct images of possible defects. The imaging operator is essentially a backprojection operator, that is, it projects measured data back to the place where they originally came from. To demonstrate the effectiveness of the operator, we apply it on synthetic data created by Comsol Multiphysics. In Chapter 6 the operator is applied to measured data.

5.1 Imaging operator

During a measurement we acquire data which holds information about the roll. Using imaging we try to reconstruct the sources and contrasts in the roll by making use of this data. In order to do so, we develop an imaging operator that acts on the data and projects it back to the imaging domain.

We start by defining the scattered field due to defects in the roll as

$$w^{\mathrm{d}}(\mathbf{x}, s) = \int_{\mathbf{x}' \in \mathbb{D}^{\mathrm{d}}} G(\mathbf{x} - \mathbf{x}', s) q^{\mathrm{d}}(\mathbf{x}', s) \mathrm{d}V, \qquad \text{with } \mathbf{x} \in \mathbb{D}^{\mathrm{r}}. \tag{5.1}$$

Here, G is the frequency-dependent Green's function, q^{d} is the scatterer source defined in domain $\mathbb{D}^{\mathrm{d}}$, and w^{d} is the field due to a defect measured in the

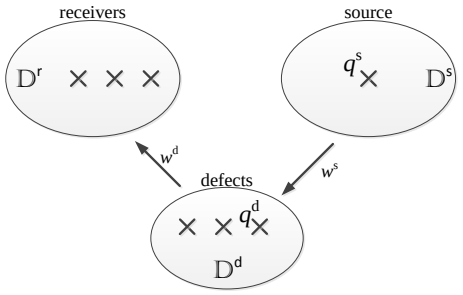

Figure 5.1: Configuration used in imaging. Three domains are specified, the source domain $\mathbb{D}^{\mathrm{s}}$ with source q^{s}, the scatterer domain $\mathbb{D}^{\mathrm{d}}$ with sources q^{d}, and the receiver domain $\mathbb{D}^{\mathrm{r}}$ where the receivers are located.

receiver domain $\mathbb{D}^{\mathrm{r}}$. This scatterer source is induced by the field radiated by the transmit antenna. In particular, we have

$$q^{\mathrm{d}}(\mathbf{x}) = \chi(\mathbf{x}) w(\mathbf{x}, s), \tag{5.2}$$

where w is the total field inside the domain $\mathbb{D}^{\mathrm{d}}$ and χ is the frequency-independent contrast function containing the medium parameters of the defect. For imaging purposes, we are interested in the distance between the source and the scatterer and the phase shifts which arise. Therefore, we are not concerned about the exact total field inside the steel and we can replace the total field by the incident field using the Born approximation[1]. This incident field is given by

$$w^{\mathrm{s}}(\mathbf{x}, s) = \int_{\mathbf{x}' \in \mathbb{D}^{\mathrm{s}}} G(\mathbf{x} - \mathbf{x}', s) q^{\mathrm{s}}(\mathbf{x}', s) \mathrm{d}V, \qquad \text{for } \mathbf{x} \in \mathbb{D}^{\mathrm{d}}. \tag{5.3}$$

Here, q^{s} is the source defined in the source domain $\mathbb{D}^{\mathrm{s}}$. If this source is a point source with unit amplitude located at $\mathbf{x} = \mathbf{x}_{\mathrm{s}}$, the above simplifies to

$$w^{\mathrm{s}}(\mathbf{x}, s) = G(\mathbf{x} - \mathbf{x}_{\mathrm{s}}, s). \tag{5.4}$$

Applying the Born approximation and using this incident field, we obtain for our data the integral representation

$$w^{\mathrm{d}}(\mathbf{x}, s) = \int_{\mathbf{x}' \in \mathbb{D}^{\mathrm{d}}} G(\mathbf{x} - \mathbf{x}', s) G(\mathbf{x}' - \mathbf{x}_{\mathrm{s}}, s) \chi(\mathbf{x}') \, \mathrm{d}V \qquad \text{with } \mathbf{x} \in \mathbb{D}^{\mathrm{r}}. \tag{5.5}$$

Now typically data is collected for different source locations at different frequencies and different receiver locations. Denoting the position vector of the different point source locations by $\mathbf{x}_{\mathrm{s};m}$, $m = 1, 2, ..., M$, the position vector of the different receiver locations by $\mathbf{x}_{\mathrm{r};n}$, $n = 1, 2, ..., N$, and the different frequencies of operation by s_f, $f = 1, 2, ..., F$, we have a total amount of measured data given by

$$w^{\mathrm{d}}(\mathbf{x}_{\mathrm{r};n}, \mathbf{x}_{\mathrm{s};m}, s_f) = \int_{\mathbf{x}' \in \mathbb{D}^{\mathrm{d}}} G(\mathbf{x}_{\mathrm{r};n} - \mathbf{x}', s_f) G(\mathbf{x}' - \mathbf{x}_{\mathrm{s};m}, s_f) \chi(\mathbf{x}') \, \mathrm{d}V, \tag{5.6}$$

for $m = 1, 2, ..., M$, $n = 1, 2, ..., N$, and $f = 1, 2, ..., F$. The right-hand side of the above equation defines a data operator

$$\Lambda\{\chi\}(\mathbf{x}_{\mathrm{r};n}, \mathbf{x}_{\mathrm{s};m}, s_f) = \int_{\mathbf{x}' \in \mathbb{D}^{\mathrm{d}}} G(\mathbf{x}_{\mathrm{r};n} - \mathbf{x}', s_f) G(\mathbf{x}' - \mathbf{x}_{\mathrm{s};m}, s_f) \chi(\mathbf{x}') \, \mathrm{d}V. \tag{5.7}$$

To introduce the imaging operator, we first define the inner product of two measured data sets. Specifically, the inner product of the data sets w and v is defined as

$$\langle w, v \rangle_{\mathrm{M}} = \sum_{m=1}^{M} \sum_{n=1}^{N} \sum_{f=1}^{F} w(\mathbf{x}_{\mathrm{r};n}, \mathbf{x}_{\mathrm{s};m}, s_f) v^*(\mathbf{x}_{\mathrm{r};n}, \mathbf{x}_{\mathrm{s};m}, s_f), \tag{5.8}$$

where the asterisk denotes complex conjugation. Similarly, the inner product of two functions χ and ξ defined on the imaging domain $\mathbb{D}^{\mathrm{d}}$ is defined as

$$\langle \chi, \xi \rangle_{\mathrm{D}} = \int_{\mathbf{x} \in \mathbb{D}^{\mathrm{d}}} \chi(\mathbf{x}) \xi^*(\mathbf{x}) \, \mathrm{d}V. \tag{5.9}$$

[1]The defects are usually small as well and the Born approximation is fairly accurate in these cases.

The *adjoint or imaging operator* is now introduced as the operator Λ^* for which

$$\langle \Lambda\{\chi\}, v\rangle_{\mathrm{M}} = \langle \chi, \Lambda^*\{v\}\rangle_{\mathrm{D}}$$

for all measurement sets v and all χ defined on the imaging domain. Notice that by definition the imaging operator acts on measured data and maps it to a function defined on the imaging domain.

To arrive at an explicit expression for the imaging operator, we substitute the definition of the data operator in the left-hand side of the above equation. We obtain

$$\langle \Lambda\{\chi\}, v\rangle_{\mathrm{M}} =$$
$$\sum_{m=1}^{M}\sum_{n=1}^{N}\sum_{f=1}^{F}\int_{\mathbf{x}'\in\mathbb{D}^{\mathrm{d}}} G(\mathbf{x}_{\mathrm{r};n}-\mathbf{x}', s_f)G(\mathbf{x}'-\mathbf{x}_{\mathrm{s};m}, s_f)\chi(\mathbf{x}')\,\mathrm{d}V\, v^*(\mathbf{x}_{\mathrm{r};n}, \mathbf{x}_{\mathrm{s};m}, s_f) =$$
$$\int_{\mathbf{x}'\in\mathbb{D}^{\mathrm{d}}} \chi(\mathbf{x}')\left[\sum_{m=1}^{M}\sum_{n=1}^{N}\sum_{f=1}^{F} G^*(\mathbf{x}_{\mathrm{r};n}-\mathbf{x}', s_f)G^*(\mathbf{x}'-\mathbf{x}_{\mathrm{s};m}, s_f)v(\mathbf{x}_{\mathrm{r};n}, \mathbf{x}_{\mathrm{s};m}, s_f)\right]^* \mathrm{d}V.$$

From this result, the imaging operator is easily recognized as

$$\Lambda^*\{v\}(\mathbf{x}) = \sum_{m=1}^{M}\sum_{n=1}^{N}\sum_{f=1}^{F} G^*(\mathbf{x}_{\mathrm{r};n}-\mathbf{x}, s_f)G^*(\mathbf{x}-\mathbf{x}_{\mathrm{s};m}, s_f)v(\mathbf{x}_{\mathrm{r};n}, \mathbf{x}_{\mathrm{s};m}, s_f), \quad (5.10)$$

with $\mathbf{x}\in\mathbb{D}^{\mathrm{d}}$. The description of the imaging operator is now complete, except for the Green's functions which we will discuss in the next section.

5.2 Green's function

In the previous chapters, we have shown that the scalar steady-state Green's function for a vacuum domain is given by

$$G(\mathbf{x},\omega) = \frac{\exp(-\gamma_0|\mathbf{x}|)}{4\pi|\mathbf{x}|},$$

where the propagation coefficient is given by $\gamma_0 = -i\omega/c_0$.

For a homogeneous and lossy medium, the Green's function is essentially the same except for the propagation factor. Specifically, for a homogeneous medium with a constant conductivity σ^{roll}, constant permittivity ε, and constant permeability μ^{roll}, we have

$$G(\mathbf{x},\omega) = \frac{\exp(-\gamma|\mathbf{x}|)}{4\pi|\mathbf{x}|},$$

where the propagation coefficient is now given by

$$\gamma = \left[-i\omega\mu^{\mathrm{roll}}(\sigma^{\mathrm{roll}} - i\omega\varepsilon)\right]^{1/2} \quad \text{with} \quad \mathrm{Re}(\gamma)\geq 0.$$

In our NDT application, we have $\sigma^{\mathrm{roll}} >> \omega\varepsilon$, since the conductivity is in the order of 10^7 S/m and the frequency in the order of 10^6 Hz, while $\varepsilon \approx \varepsilon_0$. The propagation coefficient simplifies to

$$\gamma = \frac{1-i}{\delta_{\mathrm{s}}},$$

where we have introduced the skin depth as

$$\delta_{\mathrm{s}} = \sqrt{\frac{2}{\omega \sigma^{\mathrm{roll}} \mu^{\mathrm{roll}}}}.$$

The scalar Green's function for wave field problems turns into the Green's function for diffusion problems and becomes

$$G(\mathbf{x}, \omega) = \frac{\exp(-\frac{|\mathbf{x}|}{\delta_{\mathrm{s}}}) \exp(i\frac{|\mathbf{x}|}{\delta_{\mathrm{s}}})}{4\pi|\mathbf{x}|}.$$

Substituting this Green's function in the expression for the imaging operator, we obtain

$$\Lambda^*\{v\}(\mathbf{x}) = \sum_{m=1}^{M} \sum_{n=1}^{N} \sum_{f=1}^{F} \frac{\exp\left[-(i+1)\dfrac{d_{n,m}(\mathbf{x})}{\delta_{\mathrm{s};f}}\right]}{16\pi^2 |\mathbf{x}_{\mathrm{r};n} - \mathbf{x}|^2 |\mathbf{x} - \mathbf{x}_{\mathrm{s};m}|^2} v(\mathbf{x}_{\mathrm{r};n}, \mathbf{x}_{\mathrm{s};m}, s_f), \qquad (5.11)$$

with $\mathbf{x} \in \mathbb{D}^{\mathrm{d}}$, and where we have introduced the total distance function

$$d_{n,m}(\mathbf{x}) = |\mathbf{x}_{\mathrm{r};n} - \mathbf{x}| + |\mathbf{x} - \mathbf{x}_{\mathrm{s};m}| \qquad (5.12)$$

and

$$\delta_{\mathrm{s};f} = \sqrt{\frac{2}{\omega_f \sigma^{\mathrm{roll}} \mu^{\mathrm{roll}}}} \quad \text{for } f = 1, 2, ..., F.$$

Equation (5.11) is the imaging operator for a homogeneous and highly conductive background medium (roll of infinite extent). To take the presence of air into account, we should actually use the Green's dyadics for the halfspace problem.

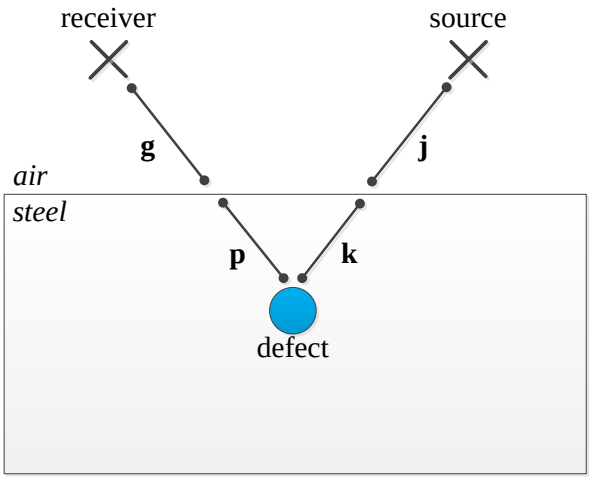

Figure 5.2: The electromagnetic field propagates in two different media, namely, air and steel. The shortest distance from an antenna to a defect has been indicated by the distances g, j, p, and k. The former two are the distances through air, while the latter two are through steel.

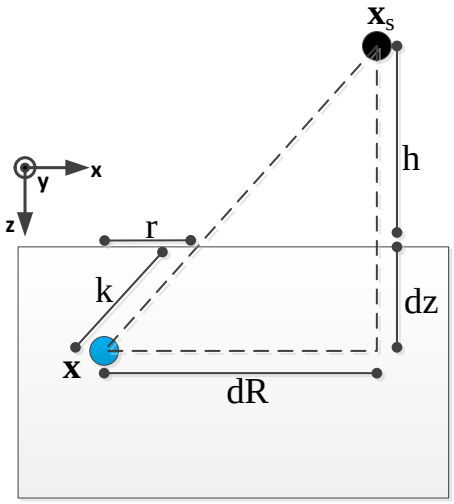

Figure 5.3: The source is located at position $\mathbf{x}_\mathrm{s}$, the point we want to evaluate at $\mathbf{x}$. Distances are indicated as parameters.

These dyadics can be determined using the techniques presented in Chapter 3. The resulting expressions are very complex, however, and very expensive to compute. We therefore resort to the following heuristic approach.

First, observe that in our configuration, fields propagate through air along a path from the antenna to the surface of the roll and along a path through the roll from the surface to the defect. This is illustrated in Figure 5.2, where the shortest distances from the antenna towards a defect are indicated. Now the denominator of the Green's function is the same in both media. The nominator, however, is medium dependent and the lengths of the shortest paths through air and steel have to be found. Typically, the antennas are placed at a height of about 1 mm above the roll and the source transmits a signal with a frequency up to approximately 1 MHz. In air this corresponds to a wavelength of 300 m (see Section 2.3). Consequently, there will hardly be any phase shift or attenuation along the path located in air. It is therefore not necessary to find the lengths g and j and their contribution to the total distances $d_{n,m}(\mathbf{x})$ can be neglected in the imaging operator. On the other hand, due to diffusion, the parts inside the roll introduce a large phase shifts and attenuation even for small distances. The lengths p and k need to be found for this reason.

To find explicit expressions for these lengths, consider the geometry depicted in Figure 5.3, where $\mathbf{x}_\mathrm{s}$ is the location of the source placed at height h and $\mathbf{x}$ the location of the evaluated point at depth dz and removed some horizontal distance dR from the source. The gradient of the line between the two points is equal to

$$GR = \frac{h + dz}{dR} = \frac{h + dz}{\sqrt{(x_\mathrm{s} - x)^2 + (y_\mathrm{s} - y)^2}}. \tag{5.13}$$

Now, the horizontal distance inside the roll is found as

$$r = \frac{dz}{GR}, \tag{5.14}$$

after which the distance k can be calculated as

$$\begin{aligned} k &= \sqrt{dz^2 + r^2} \\ &= \sqrt{dz^2 + \left(\frac{dz}{h+dz}\right)^2 [(x_\mathrm{s} - x)^2 + (y_\mathrm{s} - y)^2]}. \end{aligned} \tag{5.15}$$

The same procedure can be used to find distance p. When computing the distances $d_{n,m}(\mathbf{x})$ in the imaging operator, we use $d_{m,n}(\mathbf{x}) = k_m(\mathbf{x}) + p_n(\mathbf{x})$ instead of the original formula (5.12). Here, k_m is the distance from source m to the evaluated point, whereas p_n is the distance from receiver n to the evaluated point.

5.3 Imaging of synthetic data

Having the imaging operator ready, we are now in a position to detect some defects. To confirm that this is indeed the case, we use the program Comsol Multiphyics to create some synthetic data. The modeled configuration is depicted in Figure 5.4. Here, a source and a receiver are placed above a steel halfspace with a conductivity of 10^7 S/m and a relative permeability of 100. Three defects are present at the surface of this steel object. Each has a width of 1 mm and their edges are separated 5 mm from each other. Their depths are 0.5 mm, 0.8 mm, and 1.1 mm as illustrated in Figure 5.4. The antenna pair scans the object once from left to right, while the source transmits at 8 kHz, 10 kHz, and 20 kHz. During the scan, samples are collected every 1 mm by the source and the receiver. In this example, we image a slice through the steel plate located exactly beneath the scanning line. We do not perform a complete surface scan, since this takes too much computation time in Comsol. This does not affect the testing of the imaging operator, of course.

The data that is received by the two antennas represent the total magnetic field. Because we are interested in the scattered data only, we subtract the fields induced by a defect free part of the roll from the received data as

$$\mathrm{H}^\mathrm{d} = \mathrm{H}^\mathrm{tot} - \mathrm{H}^\mathrm{steel}. \tag{5.16}$$

The data that is left is caused only by the defects inside the roll.

To implement the imaging operator, we first subdivide our imaging domain $\mathbb{D}^\mathrm{d}$ into Q voxels. The midpoint of each voxel is denoted by $\mathbf{x}_q$, $q =$

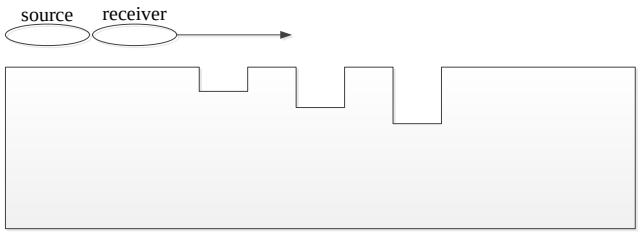

Figure 5.4: A source and a receiver scan a roll containing defects with depths 0.5 mm, 0.8 mm, and 1.1 mm (left to right). The roll is modeled as a halfspace.

$1, 2, ..., Q$. Our image is now obtained by setting $\mathbf{x} = \mathbf{x}_q$ in Eq. (5.11). We have

$$\Lambda^*\{v\}(\mathbf{x}_q) = \sum_{m=1}^{M}\sum_{n=1}^{N}\sum_{f=1}^{F} \frac{\exp\left[-(i+1)\dfrac{d_{n,m}(\mathbf{x}_q)}{\delta_{\mathrm{s};f}}\right]}{16\pi^2|\mathbf{x}_{\mathrm{r};n} - \mathbf{x}_q|^2|\mathbf{x}_q - \mathbf{x}_{\mathrm{s};m}|^2} v(\mathbf{x}_{\mathrm{r};n}, \mathbf{x}_{\mathrm{s};m}, s_f), \quad (5.17)$$

for $q = 1, 2, ..., Q$. Arranging all the elements $\Lambda^*\{v\}(\mathbf{x}_q)$ and data values $v(\mathbf{x}_{\mathrm{r};n}, \mathbf{x}_{\mathrm{s};m}, s_f)$ in the Q-by-1 and MNF-by-1 vectors $\mathbf{c}$ and $\mathbf{b}$, respectively, we can also write the imaging operator in matrix-vector form as

$$\mathbf{c} = \mathbf{A}^H\mathbf{b}, \quad (5.18)$$

where the elements of the Q-by-MNF matrix $\mathbf{A}^H$ are implicitly defined in Eq. (5.17). Note that we write the imaging operator as $\mathbf{A}^H$, since the MNF-by-Q matrix $\mathbf{A} = (\mathbf{A}^H)^H$ is essentially a discretized version of the data operator Λ given in Eq. (5.7). With this identification, our imaging approach is basically equivalent to matched filtering.

In our numerical experiment, the imaging operator of Eq. (5.17) is now applied to data acquired using a mono- and bistatic source/receiver setup. The imaging results are depicted in Figures 5.5a and 5.5b. We observe that the location of the cracks at the surface of the roll are found in both cases. If a crack has a greater depth, then a larger spot is produced by our imaging operator. Furthermore, in bistatic mode the recovered cracks spread out in depth, while in monostatic mode the width of the recovered cracks increases as the depth of the cracks increases.

In both figures the actual depth of the crack cannot be recovered. Imaging produces "blurred spots" and only uses the attenuation and phase shifts introduced along the paths between an antenna and an evaluated point. To find the exact geometric features and constitution of a crack, a more accurate model has to be developed and full nonlinear inversion techniques need to be applied.

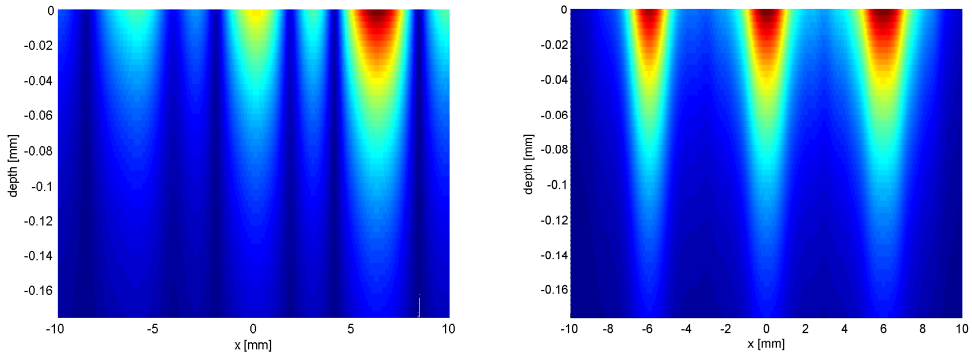

(a) (b)

Figure 5.5: Imaging results for bistatic (a) and monostatic (b) data. The cracks are located at x=-6 mm, 0 mm, and 6 mm. Going from left to right, the depths of the cracks are 0.5 mm, 0.8 mm, and 1.1 mm.

Chapter 6

Measurements

The previous chapter introduced the concept of imaging. The introduced imaging operator has been tested on synthetic data and has been proven to work. Within this chapter we will test this operator on real data measured by a setup from Lismar.

First this measurement setup is discussed, i.e. which hardware is used, what kind of signal is transmitted and what objects are to be tested. Hereafter the measured data will be presented and prepared for imaging, followed by the actual imaging itself.

6.1 Measurement setup

The measurement setup that is used to get data can be described as follows. The modulated transmit signal is created by an FPGA. This device can be programmed with the use of Lismar's software. Before the signal is transmitted it passes by a Digital to Analog Converter (DAC) and an amplifier. At the receiver end, the output of four bridges (see Section 2.3) is amplified and then digitized using an Analog to Digital Converter (ADC) operating at 10 MS/s. The FPGA allows this digital signal to be demodulated for several frequencies, after which the result is send to the PC for further processing.

A block diagram for this setup is depicted in Figure 6.1 and the components used in the measurement setup are shown in Figure 6.2a. The roll is placed in a turning lathe and while scanning, the antennas move at some height over the rotating roll from left to right while sampling the received data. This is illustrated in Figure 6.2b.

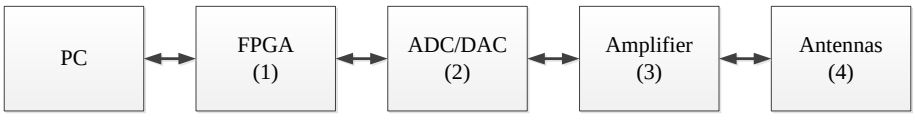

Figure 6.1: Block diagram of the measurement setup. The PC controls the FPGA, the signals are send to a DAC and amplifier, after which it reaches the antennas. The received signals are amplified, digitized, and processed by an FPGA. The PC is responsible for further processing.

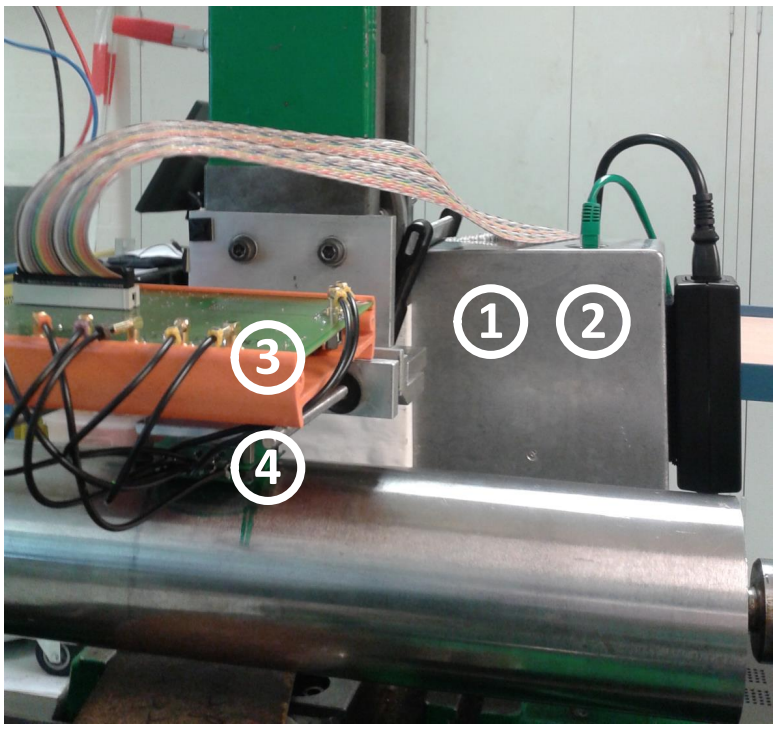

(a) Photograph showing the different components of the measurement setup. Here, (1) and (2) are the ADC/DAC and FPGA which are sealed in a box, (3) is the amplifier, and (4) are the antennas.

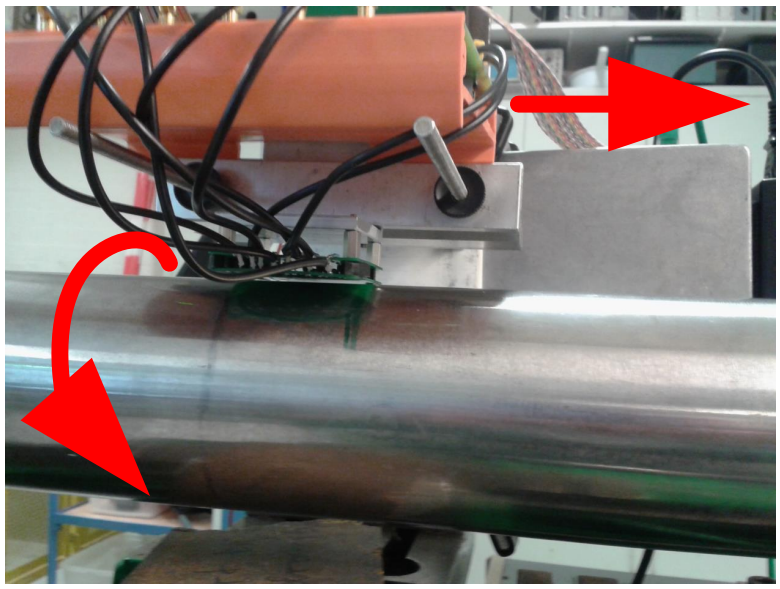

(b) The roll rotates during a scan, while the antennas move from left to right over the roll.

Figure 6.2: Photographs of the measurement setup. The top figure displays the components, whereas the lower figure shows how a scan is made.

The transmitted signal is a periodic wave of 100 kHz, which contains the 100 kHz, 300 kHz, and 500 kHz components. This allows us to get more data for processing. These three frequencies are also used for demodulation in the FPGA. Since we need the amplitude and phase of a signal for imaging, we also demodulate the received signals with the orthogonal 90 degrees forward shifted versions of the last mentioned frequencies. The resulting receiver setup is called the in-phase & quadrature receiver [33]. Our six demodulation signals are depicted in Figure 6.3. The demodulator in the FPGA uses sample and hold [33] to collect the data. This means that a group of demodulated samples are summed before it is transferred to the computer. In the end, at every 0.5 mm in roll circumference direction and 0.3 mm in roll axial direction, a complex sample is taken during the measurement.

Lismar developed software which maps the received data for each channel to a 2D surface. This surface represents the area of the roll, i.e. the circumference position versus the axial position is plotted. This implies that we do not have to account for the rotational and axial speed of the roll anymore.

Two rolls have been tested in our measurement campaign. The first roll contains some defects which are artificially made. On this roll four slots (representing cracks) with different orientations are present, each having a depth of 0.6 mm, a width of 0.1 mm, and a length of 3 mm. In addition, this roll also contains some small round holes. The second roll has actually been used in practice and contains some natural damage. This damage is seen as a weak spot or as a group of cracks on a small area.

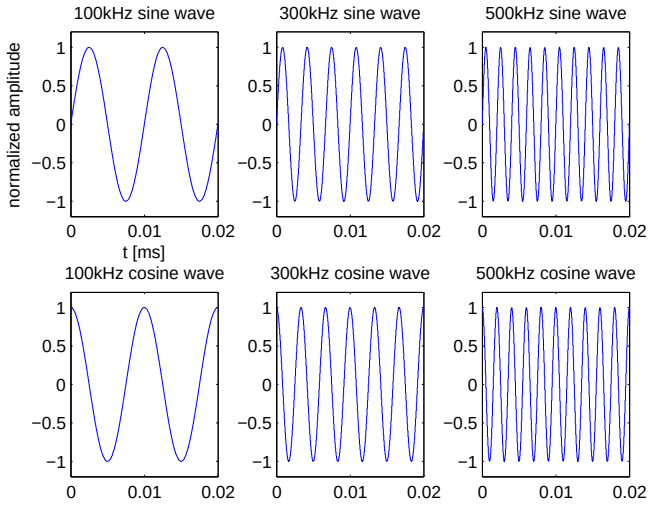

Figure 6.3: Six demodulation signals. The top row displays the sine waves of 100 kHz, 300 kHz and 500 kHz. The bottom row displays the corresponding cosine waves.

6.2 Preprocessing of data

During a measurement, we obtain data from a total of 24 channels consisting of the real and imaginary parts of the complex signals delivered by the four antennas that correspond to the three frequencies of operation. The signals represent the deviation in voltage over the bridge while scanning the roll (see Section 2.3). Because the roll is placed a bit oblique in the turning lathe, it causes some variation in height of the antenna above the roll. As a consequence, the received signals deviate during a scan, even if there is no defect. This can be seen in Figures 6.4a and 6.4b, where as an example the imaginary signal is taken from the 100 kHz data of the first roll under test. Here we see that the signal deviates strongly in both the x- and y-directions. The horizontal variation is caused because of the changing height during the scan, the vertical variation is caused because we scan the rotating roll while the antennas are moving. Therefore, strokes of the roll surface that are acquired during a scan, are a bit skewed. In the processing this has been corrected for by treating these skewed lines as straight lines again, and therefore this vertical direction is subject to height variations as well. The cracks can also be seen clearly due to the strong peaks.

The undesirable deviations can be compensated for by subtracting a clean part of the roll from the total signal. As the signal strongly deviates over the surface, the surface of the roll is divided into a few large blocks which all are treated separately. For such a block, a wide defect-free stroke of the roll is found in x-direction. This wide stroke is averaged over the y-direction to filter out noise variations and to get a single line. This line is then subtracted from the original surface to compensate for the height variations. This procedure is repeated for a wide defect-free stroke in y-direction to filter out the deviations due to the skewed scanning lines. An advantage of this method is that we immediately are left with the signal coming from the scatterers only, see Eq. (5.16). The result of this method is shown in Figures 6.4c and 6.4d. After correction, only a small offset and a few deviations are present in the x- and y-directions.

6.3 Analyzing the data

In this section we compare the measurement results with the theoretical expressions obtained in Section 4.2. Note that in that particular section we assumed that the roll has no contrast in its permeability, i.e. the roll has a relative permeability equal to one. Furthermore, only the zero-order electric field was taken into account and the resulting expression for the mutual impedance is therefore purely real. For nonmagnetic steel this may be an legitimate approximation [34].

The roll that is used to compare measurements with theory is the artificially damaged roll. This roll contains four cracks: one horizontal, one vertical, and two diagonally oriented cracks. The diagonal cracks are in opposite direction. In addition, a defect is present in the form of a cone hole with a diameter of 2.6 mm. This latter defect will be put to the test first because it comes closest to the sphere we examined in Section 4.2.

The results from the measurement are shown in Figure 6.5 for bistatic and monostatic setups. To compare the measurements with theory, we take the absolute value of the complex signal, since then we have a strong agreement

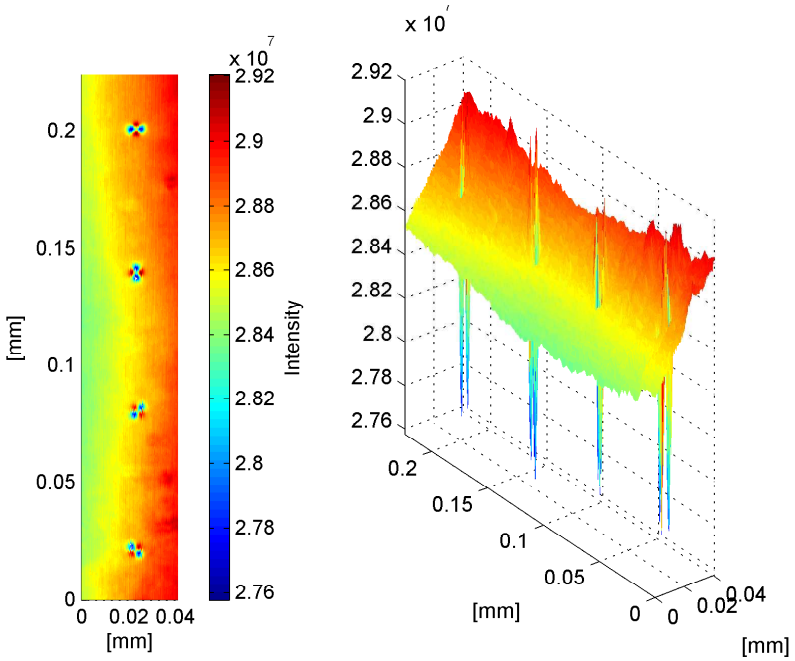

(a) Unprocessed data

(b) Unprocessed data

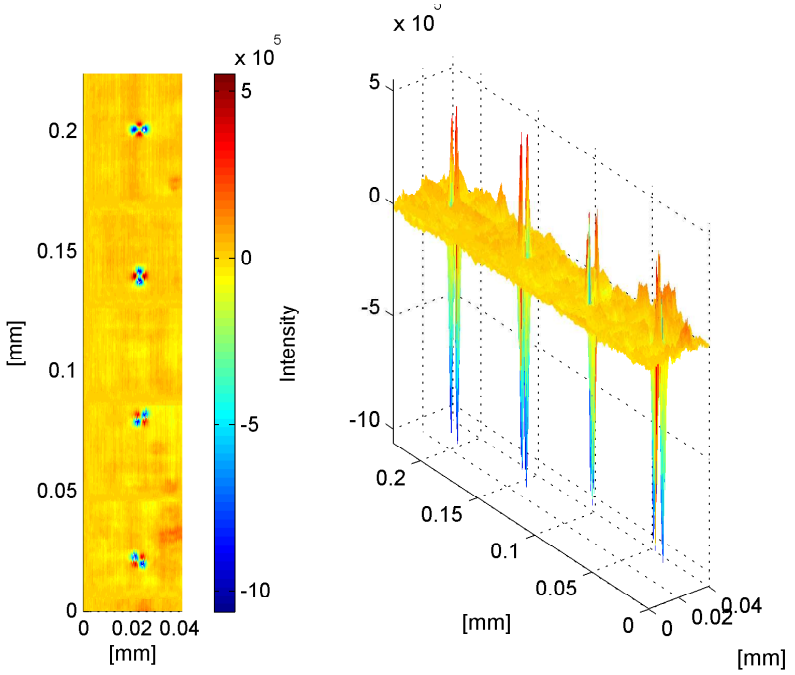

(c) Preprocessed data

(d) Preprocessed data

Figure 6.4: Compensating variations in the data due to the roll. Unprocessed data is shown in the top row, while the bottom row shows preprocessed data. Clearly, processing of the data corrects for the variations due to the roll.

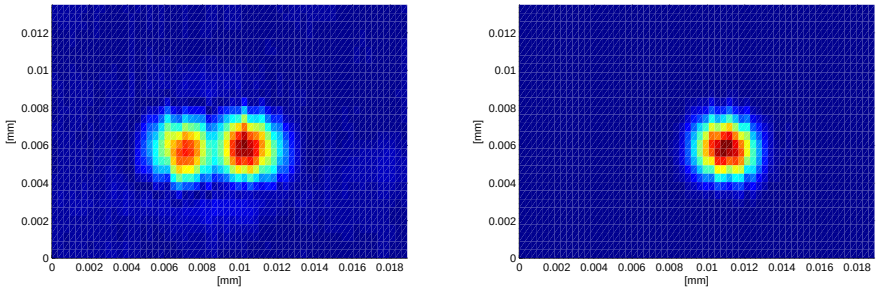

(a) (b)

Figure 6.5: Absolute signal for a bistatic (a) and monostatic (b) scan over a cone hole with a diameter of 2.6 mm.

between measured and predicted data. One reason for this could be that the relative permeability in the roll is small, or the influence of the permeability on the received signal is much smaller than the influence of the conductivity. This would mean that the resistive part of the signal dominates. The measurement results are shown in Figure 6.5 for both the bistatic and monostatic configuration. In the bistatic setup, the antennas are horizontally aligned. The corresponding results derived for a sphere are shown in Figures 4.12a and 4.12d. For the monostatic configuration the results look quite similar, except that the theoretical results show a zero point in the middle of the crack. This is because we use the electric field of a dipole antenna to create the data, which has in theory a forced zero point right beneath the center of the loop-antenna. Since the antennas have a maximum magnetic field in the center of the loop, it could cause some deviation for a small change in permeability. Another explanation is that our modeled sphere is much smaller than the wavelength, which is definitely not the case here. Therefore, the zero in the middle vanishes as well. The same trend is seen however, since the eddy currents are equally disturbed at either side of the hole.

For the bistatic setup, we observe a stretched shape in the horizontal direction for predicted and measured data. The measurements also show two peaks on the side of the cone. The reason is that the currents are more concentrated at the sides where the eddy currents run parallel. This is because the blocked eddy currents find a new way around the defect. This is confirmed in Figures 4.7c and 4.7d, where we see a darker color (larger intensity) at these sides. Because the antennas are horizontally aligned and have their most sensitive part in between their centers, the peaks are also horizontally aligned.

In our next experiment we consider a monostatic antenna setup, which scans four slots with a different orientation. The measurement data that is used is the absolute signal of the 100 kHz data-set and the measurement results are shown in Figure 6.6. The results for the corresponding theoretical model are depicted in Figure 4.14b. We observe that the figures are quite similar. The edges of the slots are highlighted most, and the highest intensity is found around the slot tips of the defects. This is because here the eddy currents are perpendicular to the long side of the slot and try to go around the defect. The two smaller peaks

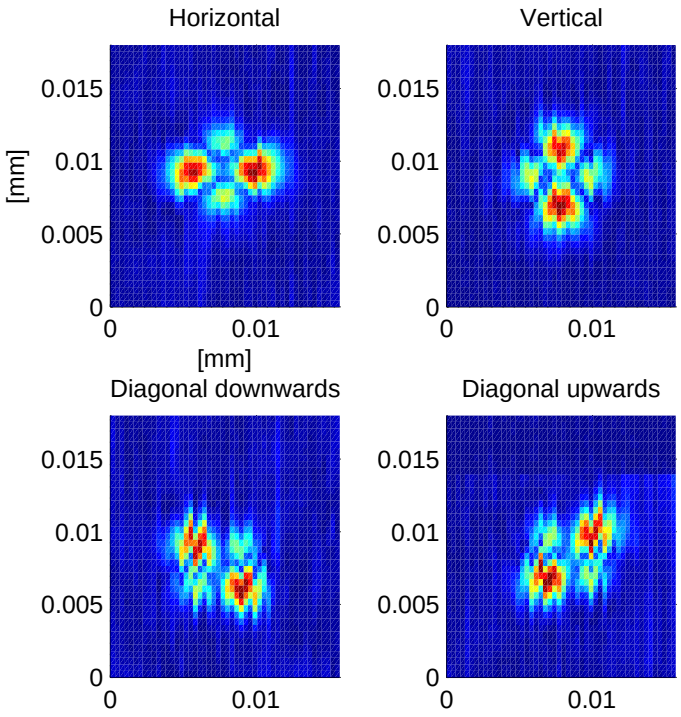

Figure 6.6: Absolute signal for four different oriented cracks. The cracks are scanned using a monostatic source/receiver unit.

in each sub-figure are caused by the short sides of the crack which disturb the currents as well, but to a lesser extent. In the original measurements, the small peaks have an opposite sign compared to the large peaks. The reason is not completely clear, but it could be that the eddy currents go over the faces of the slot rather than around the slot. The concentration of the currents running at the long sides of the slots then decreases (where it normally would increase). In our theoretical model we used a spheroid, which does not have any sharp edges and the electric field varies continuously around the defect. A strong edge-effect is therefore not observed and we do not encounter any sign changes as well (see Figure 4.9a). The strongest peaks do appear at the same locations, however.

As a final example, we compare the measured and theoretically predicted signals when scanning over a crack. The horizontally oriented crack from the artificially modified roll is used for this test. The 100 kHz component of the received signal is used and the antennas are horizontally aligned towards each other. We choose this setup because the top left crack from Figure 4.14a is made with these settings. The only difference between the setups used in practice and theory is the height of the antennas above the roll. This difference in height does not have a significant influence on the results, however (see Eq. (4.9)). If we now plot the data for a horizontal line-scan exactly over the crack, we obtain the results as shown in Figure 6.7. We observe that in this case the theoreti-

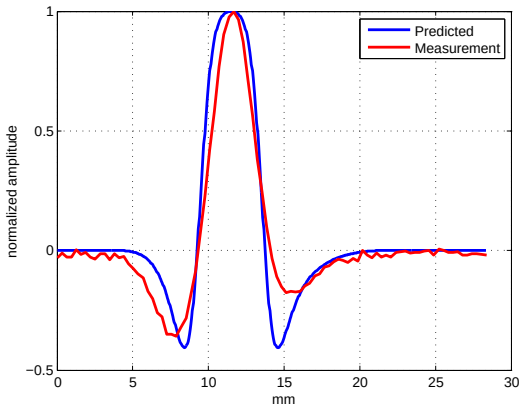

Figure 6.7: Linescan over a horizontally oriented crack with horizontally aligned antennas. Each curve is normalized with respect to its own maximum.

cally predicted response is in excellent agreement with the measurements. The spheroid used in the theory has a very small size compared to the wavelength inside the roll, while the slot in the roll has a much larger size (its length is 3 mm). Because the distance between the two antennas is 4.5 mm, the larger size of the slot is barely noticed and as a consequence the responses look quite the same. As these defects are both smaller than the distance between the antennas, the sensitivity of the antenna pair dominates. For defects with larger dimensions the influence of the shape of the defect is likely to become more noticeable.

6.4 Imaging

Within this section we will see to what extent the imaging operator works on the measured data. First we will inspect the roll with artificial defects and subsequently consider the roll with natural defects.

First, we will illustrate how the data looks like before it is processed. For the 100 kHz received signal, the monostatic, the horizontal, and diagonally oriented antennas are depicted in Figure 6.8. The vertical signal is not shown as it looks about the same as the horizontal one. Already we can see some disturbances in the steel and a significant improvement is obtained if we apply the preprocessing step from Section 6.2. The results that are obtained are shown in Figure 6.9 for the same three antenna pairs. The data is much cleaner now and all the cracks can be seen already.

The imaging operator from Chapter 5 can be built in Matlab by using some properties of the setup. The height of the antennas above the roll and the distance between the midpoint of the antennas is used. Since we do not know the properties of the material, we choose a conductivity equal to 10^7 S/m and a relative permeability equal to 1. For imaging purposes, knowing the exact values for these parameters is not essential. If, for example, the medium parameters are chosen too large then a more focussed image will be obtained, while a more "blurry" image is obtained if the medium parameters are chosen too low. The

depth at which we try to image is chosen to be one skin-depth for the highest frequency. This corresponds to a depth of 0.23 mm.

We have four antennas each receiving three different frequencies and initially the imaging operator was built to make one surface plot with all the available data. Such an approach cannot be followed, however, since each antenna has its own gain and phase shift introduced due to the hardware settings and the hardware involved in the measurement configuration. We therefore computed images for each antenna separately. Using some kind of signal processing to restore the actual phases and amplitudes, this problem can probably be resolved. The imaging results for the artificially damaged roll and naturally damaged roll are discussed in the next two subsections, starting with the artificially damaged roll.

6.4.1 Roll with artificial defects

The imaging results for a roll with artificial defects are shown in Figure 6.10. At first sight, the results are not remarkably different compared to the image we started with. This is due to the fact that the data is already really clean after preprocessing. As the antennas are really close to the surface, it is natural that if a large deviation in phase and amplitude is induced it must come from an imperfection close around it. A better comparison can be made if we zoom in on the third crack from above for the monostatic signal, since this signal is of relatively poor quality. The imaging results are shown in Figure 6.11 for the original data, the preprocessed data, and the imaged data. The resolution in all the images remains the same. We observe that imaging provides a significant improvement, since it uses all the data available from the monostatic antenna. The original and preprocessed data contain some shifts in the vertical direction. This is due to a slightly variable speed of the turning lathe. The size of the crack cannot be determined exactly, since this requires more detailed knowledge about the radiation pattern of the antennas, the distance between the antennas, and the material properties chosen for imaging. Since the edges of the crack cause the highest disturbance of the eddy currents, we can only provide an indication of the size of the defect.

Data reduction

During the measurements, usually a large number of samples were taken. Specifically, samples were taken every 0.5 mm in roll circumference direction and every 0.3 mm in roll axial direction. Lismar tries to deliver products to their clients which are able to scan a roll quickly and therefore the sampling in roll axial direction is not as fine as during the measurement. As an extreme case, assume that we take a sample every 4.5 mm in roll axial direction. This length corresponds to the distance between the antennas. As a consequence, 93% of the original data is then discarded. In Figures 6.12 and 6.13 the resulting images are presented. Again, the imaging operator is able to detect the crack, but to what extent depends on which lines are being discarded. The former uses data that is close to some peaks from the original set, whereas the latter uses data between the peaks. In both cases, however, the crack is found.

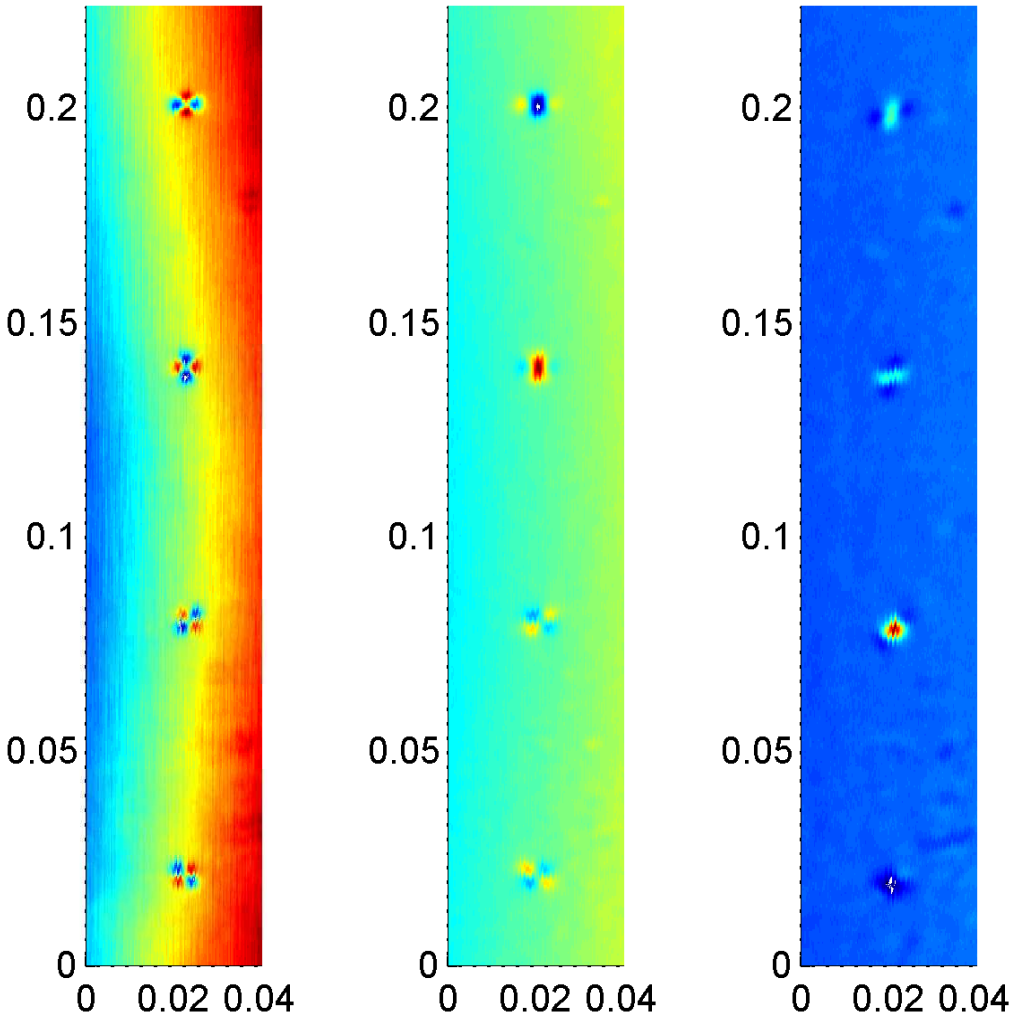

(a) monostatic (b) Horizontal (c) Diagonal

Figure 6.8: Unprocessed data for the 100 kHz signal and for different antenna pairs. Distances in this figure are expressed in meters.

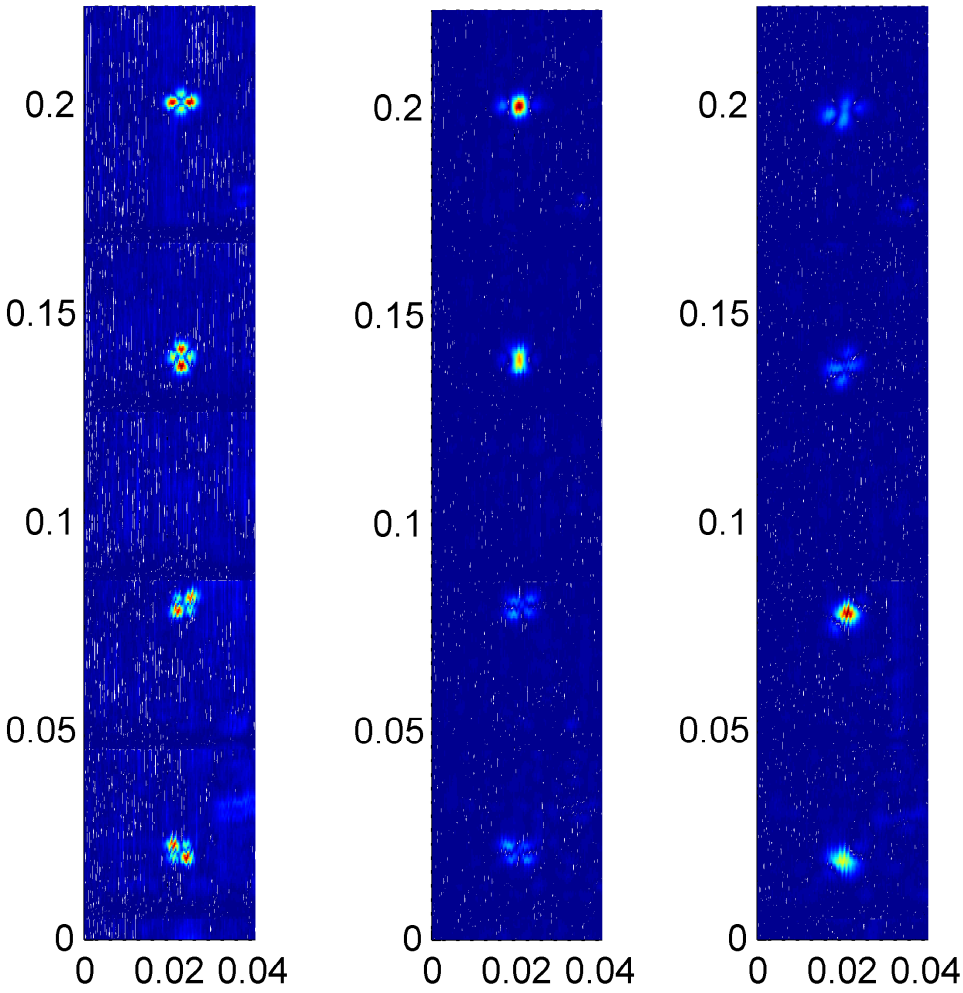

(a) monostatic (b) Horizontal (c) Diagonal

Figure 6.9: Preprocessed data for the 100 kHz signal and for different antenna pairs. Distances in this figure are expressed in meters.

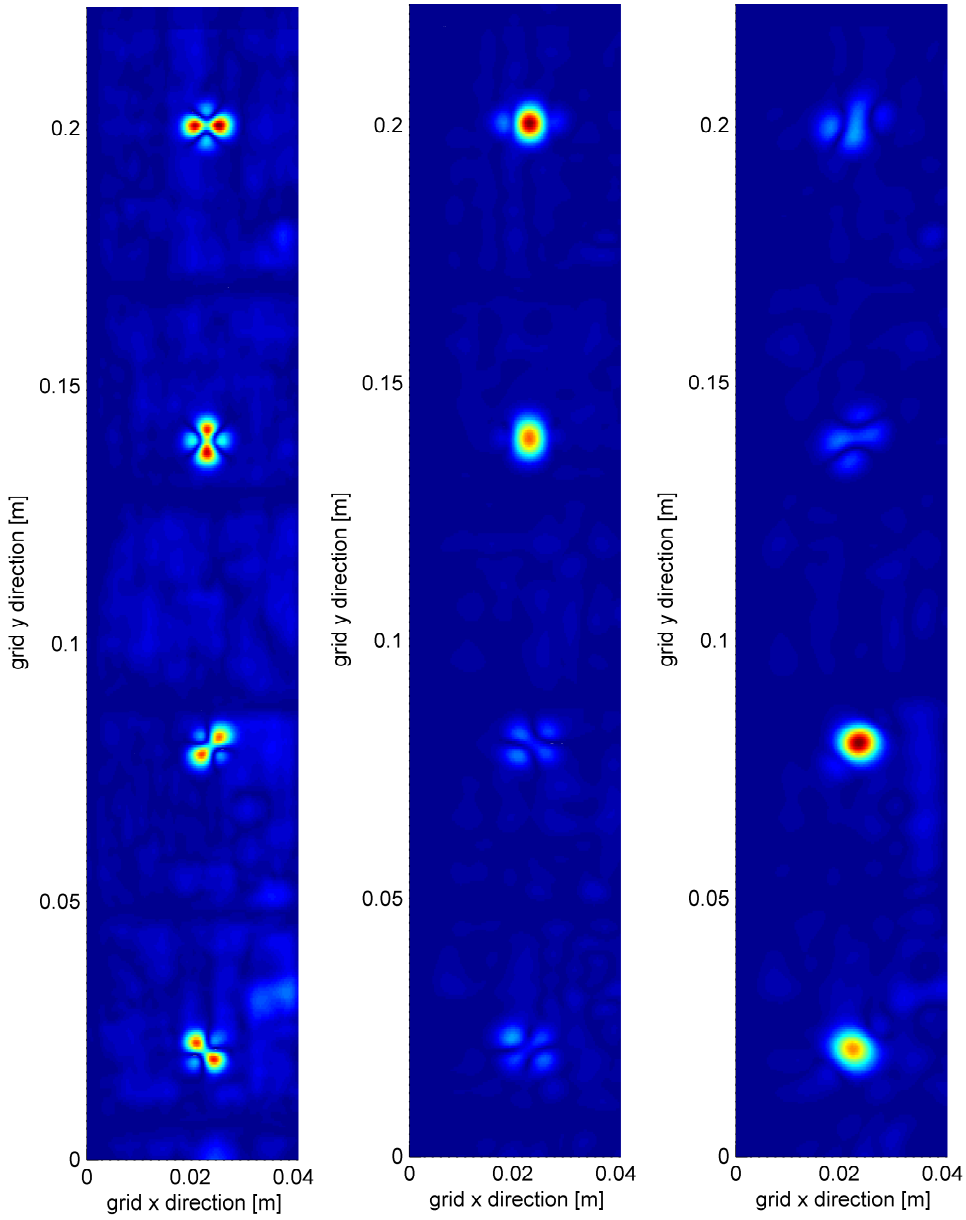

(a) monostatic (b) Horizontal (c) Diagonal

Figure 6.10: Imaging results for the different antenna pairs.

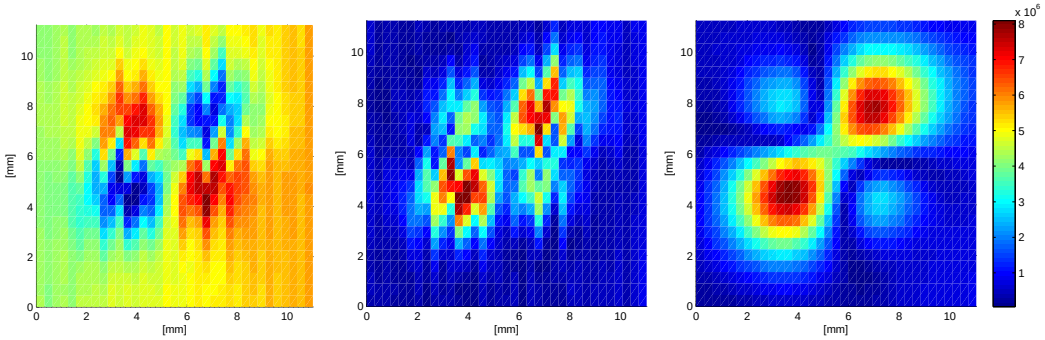

(a) Original (b) Preprocessed (c) Imaged

Figure 6.11: The original data (a), the preprocessed data (b), and the imaged data (c) are shown for the diagonally oriented crack in the first test roll.

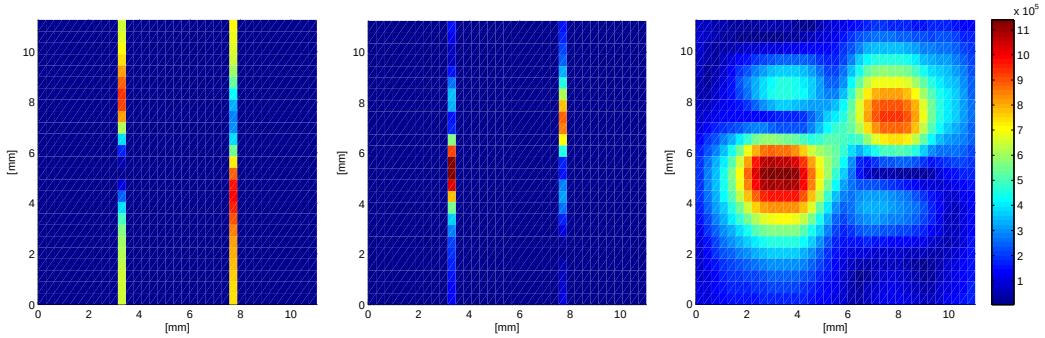

(a) Original (b) Preprocessed (c) Imaged

Figure 6.12: Every 4.5mm a sample is taken instead of every 0.3mm. The remaining data lines are close to the peaks of the original data.

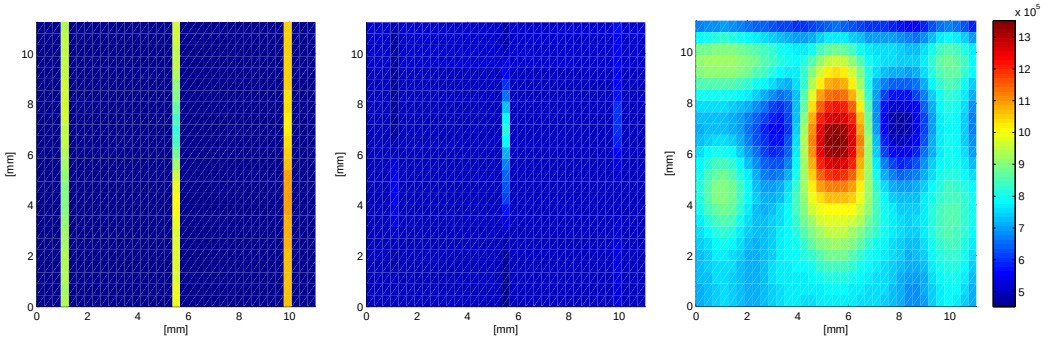

(a) Original (b) Preprocessed (c) Imaged

Figure 6.13: Every 4.5mm a sample is taken instead of every 0.3mm. The remaining data lines only pick up a small part of the crack.

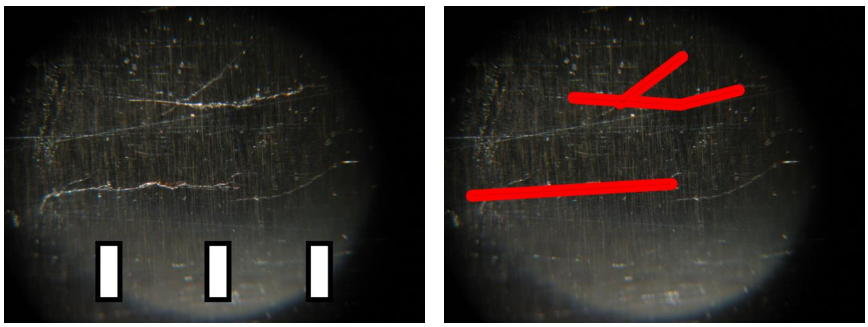

(a) (b)

Figure 6.14: In the roll a crack is located , the shape of this crack is seen in both figures. The left-hand side figure contains a mm-scale indication.

6.4.2 Roll with natural defects

The second roll which has been tested is the one with some natural defects. A photograph has been taken from a crack which is hardly visible to the naked eye and is depicted in Figure 6.14 (left) on a millimeter scale. In Figure 6.14 (right), the same crack is shown but now with the crack highlighted. Finally, the data that is acquired during the measurement is shown for the four receiving antennas in Figure 6.15, again for the absolute 100 kHz signal.

The imaging operator that we used is the same as the one before and the medium parameters were chosen to be the same as well. After the preprocessing of the data, the results as shown in Figure 6.16 are obtained. In these figures, we observe some large rectangular domains. These are caused by the preprocessing of the data as explained in Section 6.2. For a roll with so many deviations at the surface, this preprocessing has to be executed carefully in order not to subtract to much valuable scanning data. Otherwise, it could cause some artifacts as shown in Figure 6.16a.

We also notice some vague spots in the figures. These are induced by weak spots in the material, where the conductivity and permeability have changed a bit. This change can occur due the incidents during the rolling process. The red spots are most likely defects in the steel, such as our crack from the photograph which is seen in every figure. On the other hand, some red dots are visible in one figure while not in the others. This is because the imaging results depend on the orientation of the crack with respect to the antenna alignment (see Section 4.2).

Data reduction

We tested the performance of the imaging operator by disregarding almost 95% of the data as shown in Figure 6.17. We do this to simulate a faster axial scanning speed, of course. Using our imaging method, we obtain the results as shown in Figure 6.18. Clearly, most imperfections are found. We also repeated this experiment for different data-sets, as it is an arbitrary choice which 95% of the measured data in roll axial direction is discarded. All possibilities show similar outcomes, apart from some small deviations in the shape of the weak- and red spots.

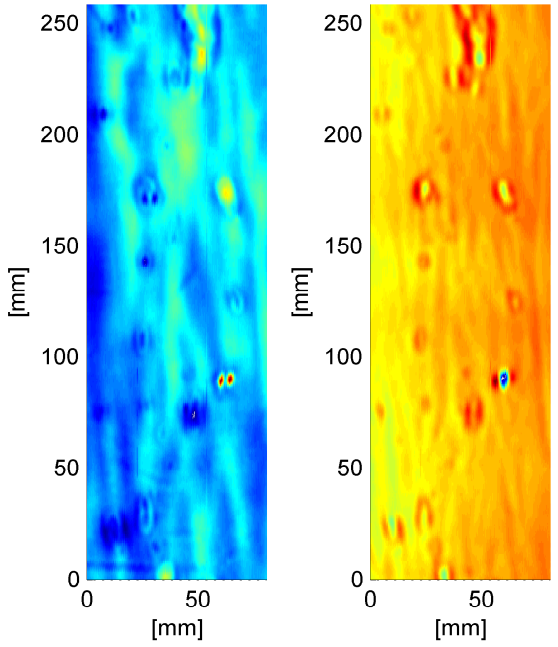

(a) monostatic (b) Horizontal

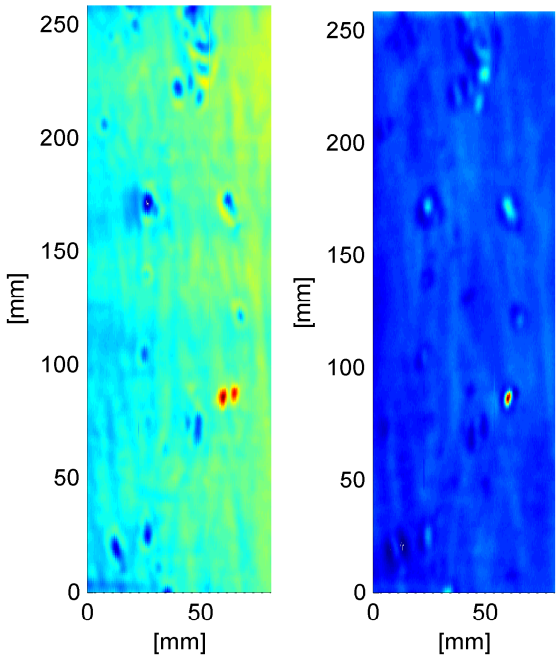

(c) Vertical (d) Diagonal

Figure 6.15: Measurement data for the four receive antennas on the natural damaged roll.

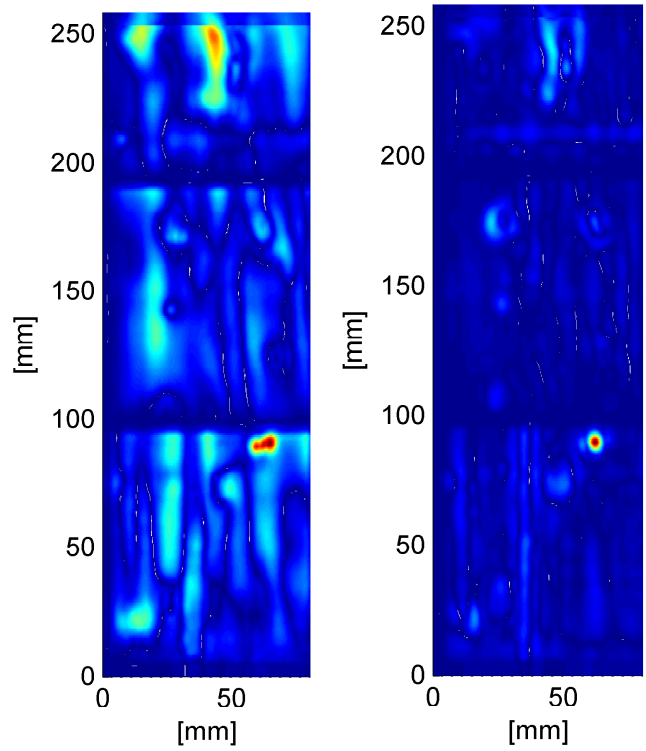

(a) monostatic

(b) Horizontal

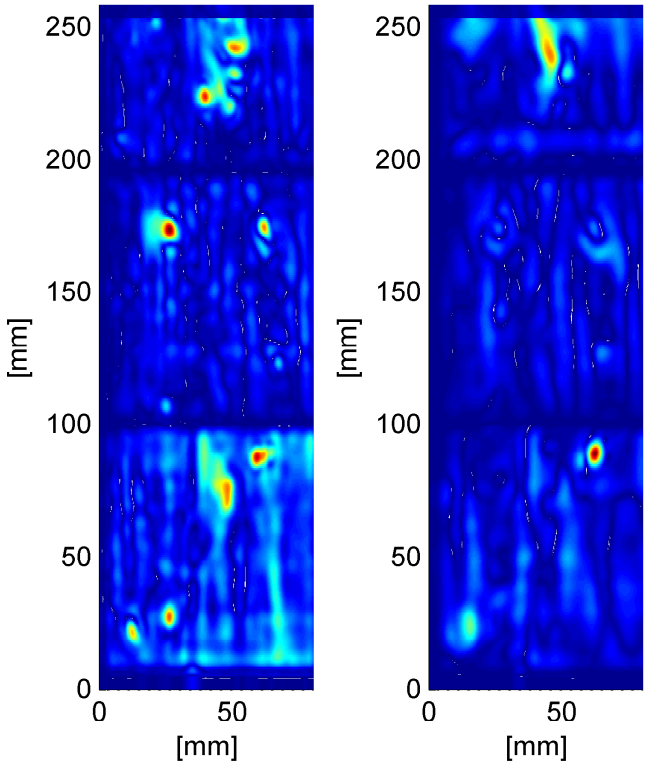

(c) Vertical

(d) Diagonal

Figure 6.16: Imaged data for the four receive antennas on the natural damaged roll.

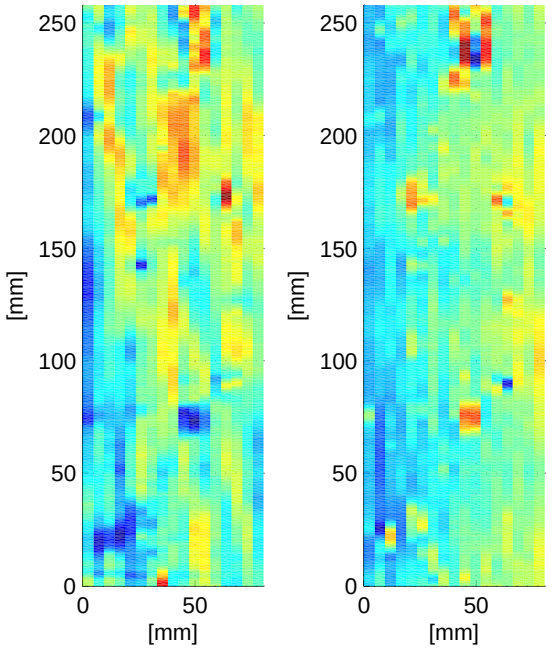

(a) monostatic (b) Horizontal

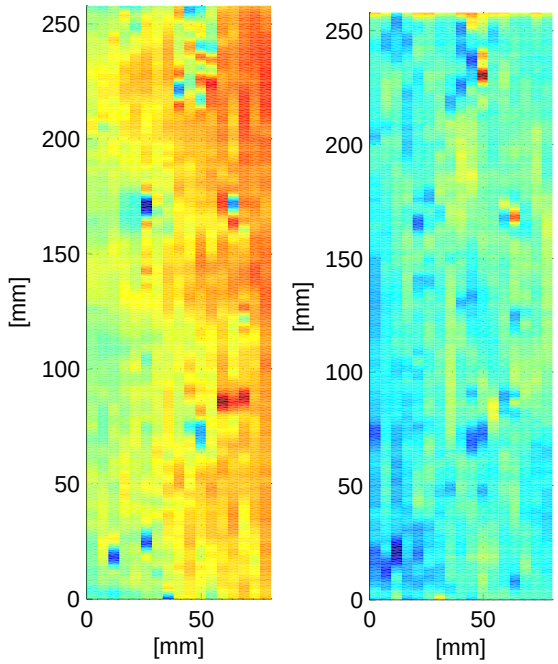

(c) Vertical (d) Diagonal

Figure 6.17: Measurement data for the four receive antennas on the natural damaged roll in case almost 95% of the original data is discarded.

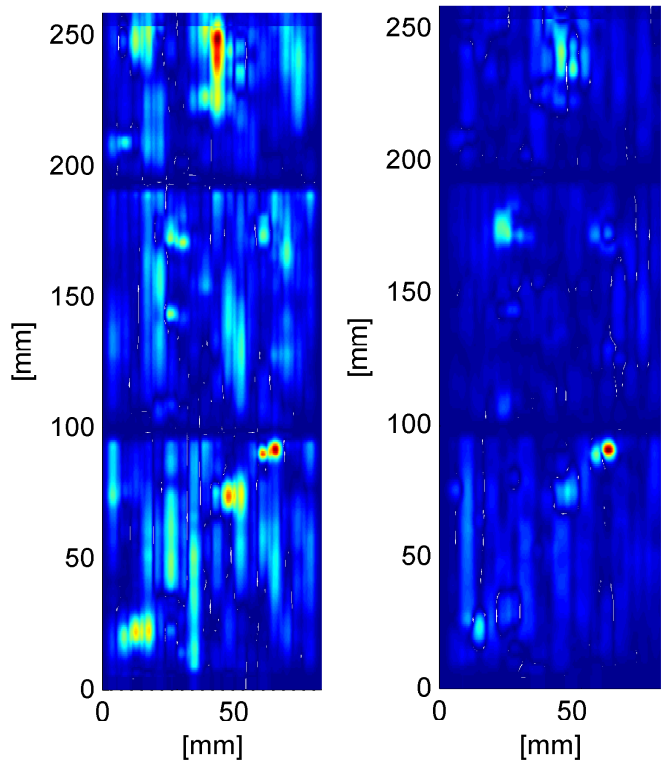

(a) monostatic

(b) Horizontal

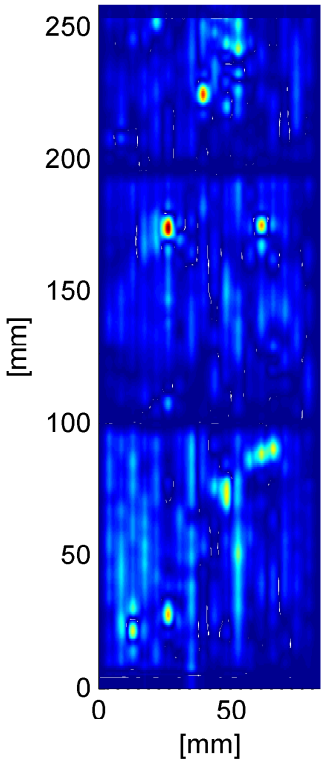

(c) Vertical

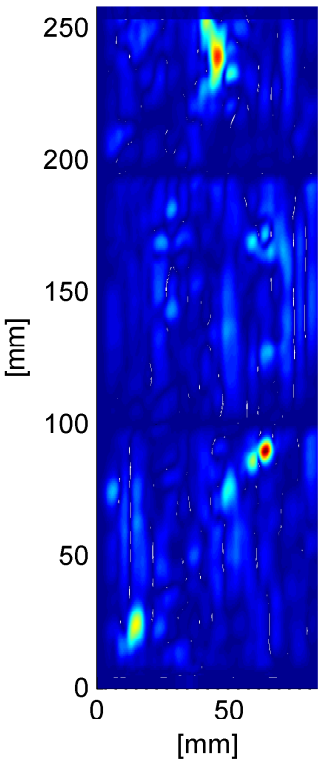

(d) Diagonal

Figure 6.18: Imaged data for the four receive antennas on the natural damaged roll in case almost 95% of the original data is discarded.

Chapter 7

Conclusions and discussion

In this thesis we have shown how induced currents in a roll can be modeled. We have also shown how defects in the roll disturb these currents and what the consequences are on the received signals in the measurement system of Lismar. These findings have been captured in one equation, which has been derived from various scientific literature. Furthermore, we were able to improve the signal processing of Lismar by the use of an imaging operator. This operator is used on real measurement data to locate defects inside a roll and it enabled faster scanning of a roll without loss of information.

Using Maxwell's equations, the electromagnetic fields in a roll have been derived. In order to obtain these fields, the roll has been modeled as a half-space, which is possible because the antennas are very close to the surface. The square loop antenna above this half space has been approximated by a magnetic dipole which excites in vertical direction, e.g. it excites perpendicular to the surface of the half space. By solving the inhomogeneous Helmholtz equation for this setup, we arrived at explicit expressions for the field inside the roll. These expressions have been validated with an equation for surface currents and with the use of the simulation program Comsol Multiphysics.

Making use of the reciprocity theorem, an expression was found for deviations in the impedance of the antennas caused by the defects. This expression is a function of the material contrasts and the electromagnetic fields inside the roll. By assuming that there is no contrast in permeability, the expression reduces to an impedance function that depends on electric field terms only. These fields were approximated by their quasi-static counterparts. Such an approach is legitimate since the size of the measurement domain is relatively small compared to the wavelength for low frequencies. The quasi-static fields provided us with a closed-form expression for the impedance change that can be used in practical measurement scenarios. Furthermore, we also studied the electric field in a defect by modeling the defect as a small spheroid with respect to the wavelength and assuming that it is placed in a uniform external field.

Using the last mentioned expression we simulated impedance variations for a number of spheroids in a conductive plate; various shapes, orientations, and contrasts have been tested. These scans were made for both monostatic and bistatic antennas configurations. The results clearly showed the shape and the orientation of the defects. We also demonstrated that the orientation of the cracks with respect to the direction of the eddy currents determines to what

extend the impedance deviates. For cracks oriented perpendicular to the eddy currents the highest change is obtained. Cracks which are in the same direction as the eddy currents and are in the shape of a needle, cause no change in the received signal.

These results have been compared with real measurement data on a roll with artificial defects which contains cracks in different orientations and shapes. Similar trends are found when the absolute signal of the measurement is compared with our simulated results. The absolute signal has been used since this one shows the most similarities. Some differences are found, however, probably caused by the assumption in our impedance model that there is no contrast in permeability. The derived theory in this work seems to fit the reality to a great extent, however.

Since the measurement data holds information about the location of the defects, an imaging operator has been introduced to locate these scattering sources. The different antennas in the measurement setup could not be combined to create one single image. This is caused by differences in phase and gain between the antennas introduced by the hardware. Therefore, the antennas could oppose each other in the imaging process instead of gaining one another. By the use of an introduced preprocessing method we were able to apply this operator on data from the scatterers only and good results were obtained for a roll with artificial defects and a roll with natural defects. Lismar tries to find defects as fast as possible. Therefore, we simulated an increase in axial scanning speed by discarding almost 95% of the measured data in roll axial direction, which is equivalent to taking a sample every 4.5 mm instead of 0.3 mm. The defects in the roll can still be found when the imaging operator is applied on this sparse data. The experiment has been repeated for several data-sets, each set containing another part of the original data-set. Up to some small deviations, we achieved similar outcomes for the different data-sets and the defects can still be found.

Based on our research and findings, several suggestions for future research are made. The first suggestion is to find the higher-order quasi-static expansion fields. A more accurate impedance formula may then be obtained and contrasts in the permeability can be taken into account as well.

The second suggestion is to apply a form of equalization on the received data. In this work, imaging is applied for each of the four antennas separately, while it would be desirable to combine these different antennas. This can be made possible with different hardware settings where all antennas have the same gain or with the use of signal processing, which tries to exclude the phases and different gains in the measurement setup introduced by the hardware. Furthermore, the contrasts in the roll can be found better using regularization techniques, which tries to suppress the noise in the received signal.

Another suggestion is that the square loop-antenna from the original measurement setup is modeled by multiple dipoles. In this work it has been modeled as a single dipole which has a different near field radiation pattern.

The fourth suggestion is that the derived background field is validated more thoroughly. In this thesis, we simulated a half space in two dimensions using Comsol Multiphysics. Instead, a better comparison could be made by a fully simulated 3D model.

In addition, the preprocessing in this work to compensate for height varia-

tions should be improved. Currently, this is done by finding clean parts of the roll by hand, and subtract these parts from the total signal. Off course, this is not a refined technique. Instead, a technique should be applied that detrends the acquired data in a professional manner.

The sixth suggestion is to optimize the transmitted signal. This signal contains three different frequencies which could be chosen such, that each received frequency by the antenna array holds the most independent information on the roll as possible. Then, the imaging operator uses more unique information which leads to better results.

The last suggestion is that the different shapes and sizes of the defects should be investigated. Within this research, defects have been modeled as small spheroids with respect to the wavelength. For further analysis on how certain cracks behave, the impedance deviations due to different cracks should be found, such as the influence of cracks with sharp edges on the change in the impedance.

Appendix A

Spectral-domain solution of Maxwell's equations in vacuum

The Fourier and Laplace transformed Maxwell's equations are given in Eqs. (3.5) and (3.6) and are repeated here for convenience. We have

$$-i\mathbf{k}\times\tilde{\mathbf{H}}+\eta_0\tilde{\mathbf{E}}=-\tilde{\mathbf{J}}, \tag{A.1}$$

and

$$i\mathbf{k}\times\tilde{\mathbf{E}}+\zeta_0\tilde{\mathbf{H}}=-\tilde{\mathbf{K}}. \tag{A.2}$$

These equations do not provide a solution for static fields and have to be extended in order to do so. To this end, the compatibility relations are used which state that

$$\eta_0\mathbf{k}^T\tilde{\mathbf{E}}=-\mathbf{k}^T\tilde{\mathbf{J}} \tag{A.3}$$

and

$$\zeta_0\mathbf{k}^T\tilde{\mathbf{H}}(\mathbf{k},s)=-\mathbf{k}^T\tilde{\mathbf{K}}. \tag{A.4}$$

We are now in a position to determine the elctromagnetic field. Specifically, if we eliminating the magnetic field strength $\tilde{\mathbf{H}}$ from Eqs. (A.1) and (A.2) and use the compatibility relation of Eq. (A.3), we obtain

$$\tilde{\mathbf{E}}(\mathbf{k},s)=\frac{1}{\gamma_0^2+\mathbf{k}^T\mathbf{k}}\left[-\left(\zeta_0\mathbb{I}+\frac{1}{\eta_0}\mathbf{k}\mathbf{k}^T\right)\tilde{\mathbf{J}}(\mathbf{k},s)-i\mathbf{k}\times\tilde{\mathbf{K}}(\mathbf{k},s)\right]. \tag{A.5}$$

Similarly, by eliminating the electric field strength and using the compatibility relation of Eq. (A.4), we find

$$\tilde{\mathbf{H}}(\mathbf{k},s)=\frac{1}{\gamma_0^2+\mathbf{k}^T\mathbf{k}}\left[-\left(\eta_0\mathbb{I}+\frac{1}{\zeta_0}\mathbf{k}\mathbf{k}^T\right)\tilde{\mathbf{K}}(\mathbf{k},s)+i\mathbf{k}\times\tilde{\mathbf{J}}(\mathbf{k},s)\right]. \tag{A.6}$$

Introducing now the electric- and magnetic vector potentials as

$$\tilde{\mathbf{A}} = \tilde{G}\tilde{\mathbf{J}} \quad \text{and} \quad \tilde{\mathbf{F}} = \tilde{G}\tilde{\mathbf{K}},$$

respectively, where

$$\tilde{G} = \frac{1}{\gamma_0^2 + \mathbf{k}^T\mathbf{k}} \tag{A.7}$$

is the spectral-domain scalar Green's function, we can write the spectral domain field quantities as

$$\tilde{\mathbf{E}}(\mathbf{k}, s) = -\left(\zeta_0 \mathbb{I} + \frac{1}{\eta_0}\mathbf{k}\mathbf{k}^T\right)\tilde{\mathbf{A}}(\mathbf{k}, s) - i\mathbf{k} \times \tilde{\mathbf{F}}(\mathbf{k}, s), \tag{A.8}$$

and

$$\tilde{\mathbf{H}}(\mathbf{k}, s) = -\left(\eta_0 \mathbb{I} + \frac{1}{\zeta_0}\mathbf{k}\mathbf{k}^T\right)\tilde{\mathbf{F}}(\mathbf{k}, s) + i\mathbf{k} \times \tilde{\mathbf{A}}(\mathbf{k}, s). \tag{A.9}$$

Appendix B

The electromagnetic field inside a two-layer configuration

To determine the vector potential $\tilde{F}_z$, it is required to determine the coefficients $\tilde{\mathrm{a}}^-$, $\tilde{\mathrm{b}}^-$, $\tilde{\mathrm{b}}^+$, and $\tilde{\mathrm{c}}^+$. Four equations are required to solve for these four coefficients. These equations follow from the source and boundary conditions that are required to hold at the planes $z = -h$ and $z = 0$, respectively.

Let us start with the source conditions at the plane $z = -h$. From Helmholtz's equation it immediately follows that $\tilde{F}_z$ should be continuous across the plane $z = -h$. In other words, we must have

$$\lim_{z\downarrow -h} \tilde{F}_z = \lim_{z\uparrow -h} \tilde{F}_z. \tag{B.1}$$

Furthermore, if we integrate Helmholtz's equation over a small interval symmetrically located around $z = -h$, we obtain

$$\lim_{\varepsilon\downarrow 0} \int_{z=-h-\varepsilon}^{-h+\varepsilon} (\partial_z^2 - \gamma_a^2)\tilde{F}_z dz = -\zeta_a \hat{m} \lim_{\varepsilon\downarrow 0} \int_{z=-h-\varepsilon}^{-h+\varepsilon} \delta(z+h) dz, \tag{B.2}$$

which simplifies to

$$\lim_{z\downarrow -h} \partial_z \tilde{F}_z - \lim_{z\uparrow -h} \partial_z \tilde{F}_z = -\zeta_a \hat{m}, \tag{B.3}$$

since $\tilde{F}_z$ is a bounded function of z. Equations (B.1) and (B.3) are the source conditions that should hold at the source plane $z = -h$. Repeating the above procedure at the interface $z = 0$, we arrive at the boundary conditions

$$\lim_{z\downarrow 0} \tilde{F}_z = \lim_{z\uparrow 0} \tilde{F}_z \tag{B.4}$$

and

$$\lim_{z\downarrow 0} \partial_z \tilde{F}_z = \lim_{z\uparrow 0} \partial_z \tilde{F}_z. \tag{B.5}$$

These boundary conditions tell us that $\tilde{F}_z$ and $\partial_z \tilde{F}_z$ should be continuous upon crossing the interface $z = 0$.

If we now substitute the general solutions for $\tilde{F}_z$ from Eqs. (3.51)-(3.53) in the above source and boundary conditions, we obtain the 4-by-4 system

$$\tilde{\mathrm{b}}^{+} e^{\gamma_\mathrm{a} h} + \tilde{\mathrm{b}}^{-} e^{-\gamma_\mathrm{a} h} = \tilde{\mathrm{a}}^{-} e^{-\gamma_\mathrm{a} h}, \tag{B.6}$$

$$-\gamma_\mathrm{a} \tilde{\mathrm{b}}^{+} e^{\gamma_\mathrm{a} h} + \gamma_\mathrm{a} \tilde{\mathrm{b}}^{-} e^{-\gamma_\mathrm{a} h} - \gamma_\mathrm{a} \tilde{\mathrm{a}}^{-} e^{-\gamma_\mathrm{a} h} = -\tilde{\zeta}_\mathrm{a} \tilde{m}, \tag{B.7}$$

$$\tilde{\mathrm{c}}^{+} = \tilde{\mathrm{b}}^{+} + \tilde{\mathrm{b}}^{-}, \tag{B.8}$$

and

$$-\gamma_\mathrm{b} \tilde{\mathrm{c}}^{+} = -\gamma_\mathrm{a} \tilde{\mathrm{b}}^{+} + \gamma_\mathrm{a} \tilde{\mathrm{b}}^{-}, \tag{B.9}$$

and the coefficients are found as

$$\tilde{\mathrm{a}}^{-} = \frac{\zeta_\mathrm{a} \tilde{m}}{2\gamma_\mathrm{a}} [e^{\gamma_\mathrm{a} h} + \frac{\gamma_\mathrm{a} - \gamma_\mathrm{b}}{\gamma_\mathrm{a} + \gamma_\mathrm{b}} e^{-\gamma_\mathrm{a} h}], \tag{B.10}$$

$$\tilde{\mathrm{b}}^{-} = \frac{\zeta_\mathrm{a} \tilde{m}}{2\gamma_\mathrm{a}} \frac{\gamma_\mathrm{a} - \gamma_\mathrm{b}}{\gamma_\mathrm{a} + \gamma_\mathrm{b}} e^{-\gamma_\mathrm{a} h}, \tag{B.11}$$

$$\tilde{\mathrm{b}}^{+} = \frac{\zeta_\mathrm{a} \tilde{m}}{2\gamma_\mathrm{a}} e^{-\gamma_\mathrm{a} h}, \tag{B.12}$$

and

$$\tilde{c}^{+} = \frac{\zeta_\mathrm{a} \tilde{m}}{2\gamma_\mathrm{a}} \frac{2\gamma_\mathrm{a}}{\gamma_\mathrm{a} + \gamma_\mathrm{b}} e^{-\gamma_\mathrm{a} h}. \tag{B.13}$$

Substituting these coefficients in Eqs. (3.51)-(3.53), we arrive at the solutions

$$\text{Region I} \qquad \tilde{F}_z = \frac{\zeta_\mathrm{a} \tilde{m}}{2\gamma_\mathrm{a}} [e^{\gamma_\mathrm{a}(z+h)} + R e^{\gamma_\mathrm{a}(z-h)}], \tag{B.14}$$

$$\text{Region II} \qquad \tilde{F}_z = \frac{\zeta_\mathrm{a} \tilde{m}}{2\gamma_\mathrm{a}} [e^{-\gamma_\mathrm{a}(z+h)} + R e^{\gamma_\mathrm{a}(z-h)}], \tag{B.15}$$

and

$$\text{Region III} \qquad \tilde{F}_z = \frac{\zeta_\mathrm{a} \tilde{m}}{2\gamma_\mathrm{a}} T e^{-\gamma_\mathrm{a} h} e^{-\gamma_\mathrm{b} z}, \tag{B.16}$$

where R and T are the reflection and transmission coefficients given by

$$R = \frac{\gamma_\mathrm{a} - \gamma_\mathrm{b}}{\gamma_\mathrm{a} + \gamma_\mathrm{b}} \quad \text{and} \quad T = \frac{2\gamma_\mathrm{a}}{\gamma_\mathrm{a} + \gamma_\mathrm{b}},$$

respectively.

To return to real space, the inverse Fourier transform from Eq. (3.45) should be applied. Since we are not interested in the electromagnetic field in Region I,

only Regions II and III are considered. Starting with the former, we have

$$\begin{aligned}\hat{F}_z(x,y,z,\omega) &= \frac{1}{4\pi^2}\int_{k_x=-\infty}^{\infty}\int_{k_y=-\infty}^{\infty}\tilde{F}_z(k_x,k_y,z,\omega)e^{i(k_x x+k_y y)}\mathrm{d}k_x\mathrm{d}k_y,\\ &= \frac{\zeta_\mathrm{a}\hat{m}}{8\pi^2}\int_{k_x=-\infty}^{\infty}\int_{k_y=-\infty}^{\infty}\frac{1}{\gamma_\mathrm{a}}[e^{-\gamma_\mathrm{a}(z+h)}+Re^{\gamma_\mathrm{a}(z-h)}]e^{i(k_x x+k_y y)}\mathrm{d}k_x\mathrm{d}k_y.\end{aligned} \tag{B.17}$$

To simplify this expression, it is convenient to use polar coordinates, which is possible since our configuration is cylindrically symmetric with respect to the center of the source. This can be done for both spaces (k- and x-domain) using the following transformations

(k_x,k_y)-space	(x,y)-space
$k_x = \lambda\cos(\psi)$	$x = \rho\cos(\theta)$
$k_y = \lambda\sin(\psi)$	$y = \rho\sin(\theta)$
$\lambda = (k_x^2+k_y^2)^{\frac{1}{2}}$	$\rho = (x^2+y^2)^{\frac{1}{2}}$
$\psi = \tan^{-1}(\frac{k_x}{k_y})$	$\theta = \tan^{-1}(\frac{x}{y})$
$0 \le \lambda < \infty$	$0 \le \rho < \infty,$

and

$0 \le \psi < 2\pi$	$0 \le \theta < 2\pi.$

Consequently, we have

$$k_x x + k_y y = \lambda\rho[\cos(\psi)\cos(\theta)+\sin(\psi)\sin(\theta)] = \lambda\rho\cos(\psi-\theta), \tag{B.18}$$

$$k_x^2 + k_y^2 = \lambda^2[\cos^2(\psi)+\sin^2(\psi)] = \lambda^2, \tag{B.19}$$

$$\gamma_\mathrm{a} = (\lambda^2 - k_\mathrm{a}^2)^{\frac{1}{2}}, \tag{B.20}$$

and

$$\gamma_\mathrm{b} = (\lambda^2 - k_\mathrm{b}^2)^{\frac{1}{2}}. \tag{B.21}$$

Finally, the integration parameters can be changed with the use of the Jacobian determinant as

$$\begin{aligned}\det(J(\lambda,\psi)) &= \det\begin{bmatrix}\frac{\partial k_x}{\partial\lambda} & \frac{\partial k_x}{\partial\psi}\\ \frac{\partial k_y}{\partial\lambda} & \frac{\partial k_y}{\partial\psi}\end{bmatrix},\\ &= \det\begin{bmatrix}\cos(\psi) & -\lambda\sin(\psi)\\ \sin(\psi) & \lambda\cos(\psi)\end{bmatrix} = \lambda.\end{aligned} \tag{B.22}$$

Then, $\mathrm{d}k_x\mathrm{d}k_y = \lambda\mathrm{d}\lambda\mathrm{d}\psi$ and Eq. (B.17) can be written as

$$\hat{F}_z(\rho,z,\omega) = \frac{\zeta_\mathrm{a}\hat{m}}{8\pi^2}\int_{\lambda=0}^{\infty}\int_{\psi=0}^{2\pi}\frac{1}{\gamma_\mathrm{a}}[e^{-\gamma_\mathrm{a}(z+h)}+Re^{\gamma_\mathrm{a}(z-h)}]e^{i\lambda\rho\cos(\psi-\theta)}\lambda\mathrm{d}\psi\mathrm{d}\lambda. \tag{B.23}$$

The latter part of this equation is recognized as the zeroth order Bessel function of the first kind. Specifically, we have

$$\int_{\psi=0}^{2\pi} e^{i\lambda\rho\cos(\psi-\theta)}\mathrm{d}\psi = 2\pi J_0(\lambda\rho) \tag{B.24}$$

and Eq. (B.23) becomes

$$\hat{F}_z(\rho,z,\omega) = \frac{\zeta_\mathrm{a}\hat{m}}{4\pi}\int_{\lambda=0}^{\infty}\frac{\lambda}{\gamma_\mathrm{a}}[e^{-\gamma_\mathrm{a}(z+h)} + Re^{\gamma_\mathrm{a}(z-h)}]J_0(\lambda\rho)\mathrm{d}\lambda. \tag{B.25}$$

This is the vector potential $\hat{F}_z$ in Region II, that is, for $-h < z < 0$.

A similar procedure can be followed for Region III. Applying the inverse Fourier transform to

$$\tilde{F}_z = \frac{\zeta_\mathrm{a}\tilde{m}}{2\gamma_\mathrm{a}}Te^{-\gamma_\mathrm{a}h}e^{-\gamma_\mathrm{b}z} \tag{B.26}$$

and switching to polar coordinates, we obtain

$$\hat{F}_z(x,y,z,\omega) = \frac{\zeta_\mathrm{a}\hat{m}}{4\pi}\int_{\lambda=0}^{\infty}\frac{\lambda}{\gamma_\mathrm{a}}Te^{-\gamma_a h}e^{-\gamma_\mathrm{b}z}J_0(\lambda\rho)\mathrm{d}\lambda, \tag{B.27}$$

where we again used Eq. (B.24). This is the vector potential in Region III, that is, for $z > 0$.

Having found the vector potential in Regions II and III, we can finally determine the electromagnetic field in these regions using Eqs. (3.38)-(3.43).

Starting with Region II, we have for the x-component of the electric field strength

$$\begin{aligned}
\hat{E}_x &= -\partial_y\hat{F}_z = -\frac{y}{\rho}\frac{\partial}{\partial\rho}\hat{F}_z,\\
&= -\frac{y}{\rho}\frac{\zeta_\mathrm{a}\hat{m}}{4\pi}\int_{\lambda=0}^{\infty}\frac{\lambda}{\gamma_\mathrm{a}}[e^{-\gamma_\mathrm{a}(z+h)} + Re^{\gamma_\mathrm{a}(z-h)}]\frac{\partial}{\partial\rho}J_0(\lambda\rho)\mathrm{d}\lambda,\\
&= \frac{y}{\rho}\frac{\zeta_\mathrm{a}\hat{m}}{4\pi}\int_{\lambda=0}^{\infty}\frac{\lambda^2}{\gamma_\mathrm{a}}[e^{-\gamma_\mathrm{a}(z+h)} + Re^{\gamma_\mathrm{a}(z-h)}]J_1(\lambda\rho)\mathrm{d}\lambda,
\end{aligned} \tag{B.28}$$

where we have used

$$\frac{\partial}{\partial\rho}J_0(\lambda\rho) = -\lambda J_1(\lambda\rho).$$

Similarly, the y-component of the electric field strength follows as

$$\hat{E}_y = -\frac{x}{\rho}\frac{\zeta_\mathrm{a}\hat{m}}{4\pi}\int_{\lambda=0}^{\infty}\frac{\lambda^2}{\gamma_\mathrm{a}}[e^{-\gamma_\mathrm{a}(z+h)} + Re^{\gamma_\mathrm{a}(z-h)}]J_1(\lambda\rho)\mathrm{d}\lambda, \tag{B.29}$$

while $\hat{E}_z = 0$.

For the x-component of the magnetic field strength in Region II, we obtain

$$\begin{aligned}\hat{H}_x &= \zeta_{\mathrm{a}}^{-1}\partial_x\partial_z\hat{F}_z \\ &= -\frac{\hat{m}}{4\pi}\partial_x\int_{\lambda=0}^{\infty}[e^{-\gamma_{\mathrm{a}}(z+h)} - Re^{\gamma_{\mathrm{a}}(z-h)}]\lambda J_0(\lambda\rho)\mathrm{d}\lambda, \\ &= -\frac{\hat{m}}{4\pi}\frac{x}{\rho}\int_{\lambda=0}^{\infty}[e^{-\gamma_{\mathrm{a}}(z+h)} - Re^{\gamma_{\mathrm{a}}(z-h)}]\lambda\frac{\partial}{\partial\rho}J_0(\lambda\rho)\mathrm{d}\lambda, \\ &= \frac{\hat{m}}{4\pi}\frac{x}{\rho}\int_{\lambda=0}^{\infty}[e^{-\gamma_{\mathrm{a}}(z+h)} - Re^{\gamma_{\mathrm{a}}(z-h)}]\lambda^2 J_1(\lambda\rho)\mathrm{d}\lambda. \end{aligned} \tag{B.30}$$

Following similar steps as above, we obtain for the y-component of the magnetic field strength

$$\hat{H}_y = \frac{\hat{m}}{4\pi}\frac{y}{\rho}\int_{\lambda=0}^{\infty}[(e^{-\gamma_{\mathrm{a}}(z+h)} - Re^{\gamma_{\mathrm{a}}(z-h)}]\lambda^2 J_1(\lambda\rho)\mathrm{d}\lambda. \tag{B.31}$$

Finally, the z-component of the magnetic field strength can be found from

$$\hat{H}_z = \zeta_{\mathrm{a}}^{-1}(\partial_z^2 + k_{\mathrm{a}}^2)\hat{F}_z. \tag{B.32}$$

Working out this expression gives

$$\begin{aligned}\hat{H}_z &= \frac{\hat{m}}{4\pi}\int_{\lambda=0}^{\infty}\frac{\lambda}{\gamma_{\mathrm{a}}}[(\gamma_{\mathrm{a}}^2 + k_{\mathrm{a}}^2)e^{-\gamma_{\mathrm{a}}(z+h)} + R(\gamma_{\mathrm{a}}^2 + k_{\mathrm{a}}^2)e^{\gamma_{\mathrm{a}}(z-h)}]J_0(\lambda\rho)\mathrm{d}\lambda, \\ &= \frac{\hat{m}}{4\pi}\int_{\lambda=0}^{\infty}\frac{\lambda^3}{\gamma_{\mathrm{a}}}[e^{-\gamma_{\mathrm{a}}(z+h)} + Re^{\gamma_{\mathrm{a}}(z-h)}]J_0(\lambda\rho)\mathrm{d}\lambda, \end{aligned} \tag{B.33}$$

where Eq. (B.20) is used in the last step. All field quantities in Region II are now completely determined.

For Region III the same process is followed and we merely state the results. For the electric field strength, we obtain

$$\hat{E}_x(\rho,z,\omega) = \frac{y}{\rho}\frac{\zeta_{\mathrm{a}}\hat{m}}{4\pi}\int_{\lambda=0}^{\infty}\frac{\lambda^2}{\gamma_{\mathrm{a}}}Te^{-\gamma_{\mathrm{a}}h}e^{-\gamma_{\mathrm{b}}z}J_1(\lambda\rho)\mathrm{d}\lambda, \tag{B.34}$$

and

$$\hat{E}_y(\rho,z,\omega) = -\frac{x}{\rho}\frac{\zeta_{\mathrm{a}}\hat{m}}{4\pi}\int_{\lambda=0}^{\infty}\frac{\lambda^2}{\gamma_{\mathrm{a}}}Te^{-\gamma_{\mathrm{a}}h}e^{-\gamma_{\mathrm{b}}z}J_1(\lambda\rho)\mathrm{d}\lambda, \tag{B.35}$$

and

$$\hat{E}_z(\rho,z,\omega) = 0, \tag{B.36}$$

while for the magnetic field strength we have

$$\hat{H}_x(\rho, z, \omega) = \frac{\zeta_\mathrm{a}}{\zeta_\mathrm{b}} \frac{x}{\rho} \frac{\hat{m}}{4\pi} \int_{\lambda=0}^{\infty} \lambda^2 \frac{\gamma_\mathrm{b}}{\gamma_\mathrm{a}} T e^{-\gamma_\mathrm{a} h} e^{-\gamma_\mathrm{b} z} J_1(\lambda\rho) \mathrm{d}\lambda, \tag{B.37}$$

$$\hat{H}_y(\rho, z, \omega) = \frac{\zeta_\mathrm{a}}{\zeta_\mathrm{b}} \frac{y}{\rho} \frac{\hat{m}}{4\pi} \int_{\lambda=0}^{\infty} \lambda^2 \frac{\gamma_\mathrm{b}}{\gamma_\mathrm{a}} T e^{-\gamma_\mathrm{a} h} e^{-\gamma_\mathrm{b} z} J_1(\lambda\rho) \mathrm{d}\lambda, \tag{B.38}$$

and

$$\hat{H}_z(\rho, z, \omega) = \frac{\zeta_\mathrm{a}}{\zeta_\mathrm{b}} \frac{\hat{m}}{4\pi} \int_{\lambda=0}^{\infty} \frac{\lambda^3}{\gamma_\mathrm{a}} T e^{-\gamma_\mathrm{a} h} e^{-\gamma_\mathrm{b} z} J_0(\lambda\rho) \mathrm{d}\lambda. \tag{B.39}$$

The background field is now completely derived and all the results are summarized in Table 3.1.

Appendix C

The surface current for a perfectly conducting roll

A perfect electric conductor is by definition a material with $\sigma \to \infty$. Such an object is electrically impenetrable and all the currents are concentrated at the surface. For waves approaching the surface the relevant boundary conditions are

$$\boldsymbol{\nu} \times \mathbf{E} \to 0 \quad \text{and} \quad \boldsymbol{\nu} \cdot \mathbf{B} \to 0. \tag{C.1}$$

Here, $\boldsymbol{\nu}$ is a unit vector perpendicular to the surface of the perfect conductor. In words, the tangential electric field component goes to zero, as does the normal component of the magnetic flux density. The tangential components of the magnetic field strength, however, build up the current at the surface of the perfect conductor. More precisely, we have

$$\mathbf{J}_{\mathrm{s}} = \boldsymbol{\nu} \times \mathbf{H}, \tag{C.2}$$

where $\mathbf{J}_{\mathrm{s}}$ is the surface current expressed in A/m.

To find this current, it it necessary to find the magnetic field at the surface. This can be done by the method of images as depicted in Figure C.1. In this

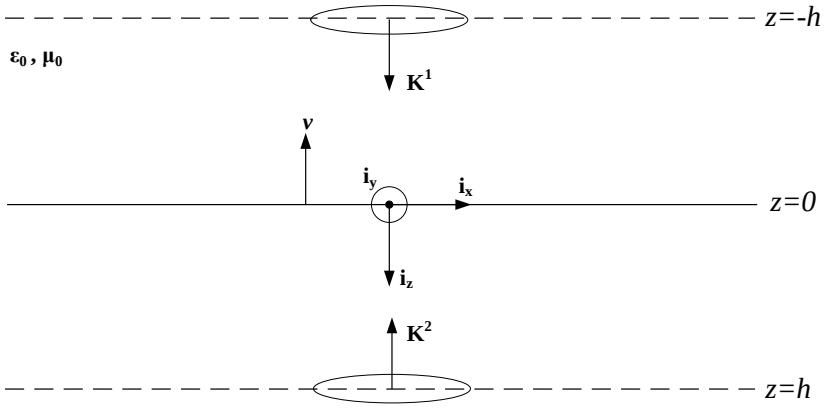

Figure C.1: Magnetic dipole and its mirror. At $z = 0$ the boundary conditions for a perfect conductor should hold.

method, the conductor is removed from the configuration and a second source is placed in the lower halfspace $z > 0$ such that the boundary conditions of Eq. (C.1) are satisfied. The resulting field in the upper halfspace $z > 0$ is then equal to the field that is present above the perfect conductor.

In particular, if $\mathbf{E}^1$ denotes the electric field strength generated by the dipole source at $z = -h$ and $\mathbf{E}^2$ is the field generated by the mirror source, then this mirror source should be chosen such that at the interface $z = 0$

$$\boldsymbol{\nu} \times \left(\mathbf{E}^1 + \mathbf{E}^2\right) = 0. \tag{C.3}$$

In order for this to be true, the second source should be positioned at the mirror location $z = +h$ and it should be equal to the negative of the first source, i.e. $\mathbf{K}^2 = -\mathbf{K}^1$ [30]. The surface current can now be calculated as follows:

$$\mathbf{J}_s = \boldsymbol{\nu} \times \left(\mathbf{H}^1 + \mathbf{H}^2\right), \tag{C.4}$$

where $\mathbf{H}^1$ is the magnetic field due to $\mathbf{K}^1$ and $\mathbf{H}^2$ is the magnetic field due to $\mathbf{K}^2$.

From Chapter 3, we know that the magnetic field due to a general $\hat{\mathbf{K}}$ source is given by

$$\hat{\mathbf{H}}^{\text{inc}}(\mathbf{x}, s) = \int_{\mathbf{x}' \in \mathbb{D}^s} \frac{1}{4\pi|\mathbf{x} - \mathbf{x}'|^3}(3\mathbb{Q} - \mathbb{I})\frac{1}{s\zeta_0}\hat{\mathbf{K}}(\mathbf{x}, s)\delta(\mathbf{x}^s - \mathbf{x}')\mathrm{d}V. \tag{C.5}$$

Taking $\hat{\mathbf{K}}$ to be a magnetic dipole of the form $\hat{\mathbf{K}} = s\mu_0\hat{I}(s)A\delta(\mathbf{x}^s - \mathbf{x})\mathbf{n}$ in which A is the area of the loop and $\mathbf{n}$ is a unit vector indicating the excitation direction of the antenna, the incident field equation gives

$$\hat{\mathbf{H}}(\mathbf{x}, s) = \frac{1}{4\pi|\mathbf{x} - \mathbf{x}^s|^3}(3\mathbb{Q} - \mathbb{I})\hat{\mathbf{K}}'. \tag{C.6}$$

Here, $\mathbf{K}' = I(s)A\mathbf{n}$. Using this fields in Eq. (C.4) gives

$$\mathbf{J}_{\text{s}} = \frac{1}{4\pi|\mathbf{x} - \mathbf{x}^s|^3}\boldsymbol{\nu} \times \left((3\mathbb{Q}^1 - \mathbb{I})\hat{\mathbf{K}}^{1'} - (3\mathbb{Q}^2 - \mathbb{I})\hat{\mathbf{K}}^{1'}\right), \tag{C.7}$$

with $z = 0$. In this expression, the projection matrices $\mathbb{Q}^1$ and $\mathbb{Q}^2$ are given by

$$\mathbb{Q}^1 = \tfrac{1}{d^2}\begin{bmatrix} x^2 & xy & -xh \\ yx & y^2 & -yh \\ -hx & -hy & h^2 \end{bmatrix} \quad \text{and} \quad \mathbb{Q}^2 = \tfrac{1}{d^2}\begin{bmatrix} x^2 & xy & xh \\ yx & y^2 & yh \\ hx & hy & h^2 \end{bmatrix},$$

where x and y are the coordinates of the evaluated point, h is the height of the antenna, and $d = |\mathbf{x} - \mathbf{x}^s|$ with $z = 0$. Working out $(3\mathbb{Q}^1 - \mathbb{I})\hat{\mathbf{K}}^{1'}$ and taking into account that $\hat{\mathbf{K}}^{1'}$ has a z-component only, we obtain

$$\hat{\mathbf{A}}^{1} := \begin{bmatrix} \frac{3x^2}{d^2} - 1 & \frac{3xy}{d^2} & \frac{-3xh}{d^2} \\ \frac{3yx}{d^2} & \frac{3y^2}{d^2} - 1 & \frac{-3yh}{d^2} \\ \frac{-3hx}{d^2} & \frac{-3hy}{d^2} & \frac{3h^2}{d^2} - 1 \end{bmatrix} \begin{bmatrix} 0 \\ 0 \\ \hat{K}_z^{1'} \end{bmatrix} = \begin{bmatrix} \frac{-3xh}{d^2} \\ \frac{-3yh}{d^2} \\ \frac{3h^2}{d^2} - 1 \end{bmatrix} \hat{K}_z^{1'} \tag{C.8}$$

with $z = 0$. Similarly,

$$\hat{\mathbf{A}}^{2} = \begin{bmatrix} \frac{3xh}{d^2} \\ \frac{3yh}{d^2} \\ \frac{3h^2}{d^2} - 1 \end{bmatrix} \hat{K}_z^{1'} \tag{C.9}$$

and Eq. (C.7) can be written as

$$\hat{\mathbf{J}}_s = \frac{1}{4\pi|\mathbf{x}-\mathbf{x}^s|^3}\left(v \times \hat{\mathbf{A}}^{\,1} - v \times \hat{\mathbf{A}}^{\,2}\right) \quad \text{with } z = 0. \tag{C.10}$$

The final expression for the surface current is found when these cross products are computed, which leads to

$$\hat{\mathbf{J}}_s(x,y) = \begin{bmatrix} 6yh \\ -6xh \\ 0 \end{bmatrix} \frac{\hat{K}_z^1}{4\pi|\mathbf{x}-\mathbf{x}^s|^5} \quad \text{with } z = 0, \tag{C.11}$$

and $\hat{K}_z^1 = I(s)A$.

Appendix D

Impedance variations due to cracks using static fields

For a defect showing no contrast in the permeability, the change in the mutual impedance between the transmitting and receiving antenna is given by

$$\delta\hat{Z} = -\int_{\mathbf{x}\in\mathbb{D}^{\mathrm{d}}} \delta\sigma\, \hat{\mathbf{e}}_s^{\mathrm{bg}} \cdot \hat{\mathbf{e}}_r^{\mathrm{bg}} \mathrm{d}V, \tag{D.1}$$

where we have applied the Born approximation as well, since we are usually looking for small defects (cracks). The background fields are required to evaluate this expression. However, computing these fields for different scanning scenarios may be a computationally intensive task. We therefore follow a quasi-static field approach resulting in an approximate but closed-form expression for the change in the mutual impedance.

We start with the upper halfspace $z < 0$. In this domain, Maxwell's equations are given by

$$-\nabla \times \hat{\mathbf{H}} + s\varepsilon_0 \hat{\mathbf{E}} = 0, \tag{D.2}$$

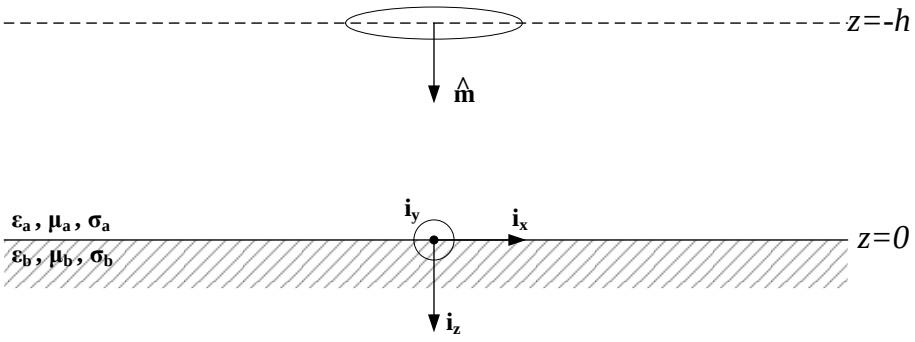

Figure D.1: Half-space with a magnetic dipole at height $z = -h$ above the roll which occupies the domain $z > 0$. Both layers have their own medium properties ε, σ and μ.

and

$$\nabla \times \hat{\mathbf{E}} + s\mu_0 \hat{\mathbf{H}} = -\hat{\mathbf{K}}^{\text{ext}}, \tag{D.3}$$

whereas the compatibility relations are

$$\nabla \cdot \hat{\mathbf{E}} = 0 \quad \text{and} \quad s\mu_0 \nabla \cdot \hat{\mathbf{H}} = -\nabla \cdot \hat{\mathbf{K}}^{\text{ext}}. \tag{D.4}$$

The lower halfspace ($z > 0$) is occupied by the roll. Since there is no source present inside this roll and since the conduction currents dominate the displacement currents, we have

$$-\nabla \times \hat{\mathbf{H}} + \sigma^{\text{roll}} \hat{\mathbf{E}} = 0, \tag{D.5}$$

and

$$\nabla \times \hat{\mathbf{E}} + s\mu^{\text{roll}} \hat{\mathbf{H}} = 0, \tag{D.6}$$

for $z > 0$. Furthermore, the compatibility relations in this halfspace are given by

$$\nabla \cdot \hat{\mathbf{E}} = 0 \quad \text{and} \quad \nabla \cdot \hat{\mathbf{H}} = 0. \tag{D.7}$$

To arrive at a quasi-static field approximation, we now expand the electromagnetic field quantities in a power series in s. Specifically, we write

$$\hat{\mathbf{E}} = \sum_{k=0}^{\infty} s^k \mathbf{E}^{[k]} \qquad \text{and} \qquad \hat{\mathbf{H}} = \sum_{k=0}^{\infty} s^k \mathbf{H}^{[k]}, \tag{D.8}$$

and refer to $\{\mathbf{E}^{[k]}, \mathbf{H}^{[k]}\}$ as the kth order expansion field. To obtain the equations that govern these fields, we substitute the power series of Eq. (D.8) in Maxwell's equations and the corresponding compatibility relations and collect all terms which have an equal power in s. This is the general procedure of obtaining the equations for the expansion fields. In our quasi-static field approach, however, we are only interested in the zero-order field $\{\mathbf{E}^{[0]}, \mathbf{H}^{[0]}\}$. Furthermore, only the zero-order electric expansion vector is required, since the electric field strength contributes to the change in the impedance if the defect exhibits no contrast in the permeability.

By following the above mentioned procedure, we obtain for the zero-order electric expansion vector the equations

$$\nabla \times \hat{\mathbf{E}}^{[0]} = -\hat{\mathbf{K}}^{\text{ext}} \quad \text{and} \quad \nabla \cdot \hat{\mathbf{E}}^{[0]} = 0,$$

which hold in the upper halfspace, while in the lower halfspace we have

$$\nabla \times \hat{\mathbf{E}}^{[0]} = 0 \quad \text{and} \quad \nabla \cdot \hat{\mathbf{E}}^{[0]} = 0.$$

Combining these two sets of equations, we have

$$\nabla \times \hat{\mathbf{E}}^{[0]} = -\hat{\mathbf{K}}^{\text{ext}} \quad \text{and} \quad \nabla \cdot \hat{\mathbf{E}}^{[0]} = 0, \tag{D.9}$$

for all $\mathbf{x} \in \mathbb{R}^3$.

To solve the above two equations, first note that the zero-order electric field strength is automatically divergence-free if we write

$$\hat{\mathbf{E}}^{[0]} = \nabla \times \hat{\mathbf{G}}^{[0]}, \tag{D.10}$$

where $\hat{\mathbf{G}}^{[0]}$ is a vector potential. This potential is required to satisfy the gauge condition (Coulomb gauge)

$$\nabla \cdot \hat{\mathbf{G}}^{[0]} = 0.$$

If we now substitute Eq. (D.10) in the first equation of (D.9), we obtain

$$\nabla \times \nabla \times \hat{\mathbf{G}}^{[0]} = -\hat{\mathbf{K}}^{\text{ext}},$$

and this equation can be written as

$$\nabla\nabla \cdot \hat{\mathbf{G}}^{[0]} - \nabla^2 \hat{\mathbf{G}}^{[0]} = -\hat{\mathbf{K}}^{\text{ext}}.$$

Finally, using the gauge condition, we arrive at

$$\nabla^2 \hat{\mathbf{G}}^{[0]} = \hat{\mathbf{K}}^{\text{ext}}$$

and the solution of this equation is given by

$$\hat{\mathbf{G}}^{[0]}(\mathbf{x}, s) = -\int_{\mathbf{x}' \in \mathbb{D}^{\text{s}}} \frac{\hat{\mathbf{K}}^{\text{ext}}(\mathbf{x}', s)}{4\pi|\mathbf{x} - \mathbf{x}'|} \mathrm{d}V. \tag{D.11}$$

Having found the vector potential, we can now determine the zero-order electric expansion field. In particular, substituting Eq. (D.11) in Eq. (D.10), we obtain

$$\hat{\mathbf{E}}^{[0]}(\mathbf{x}, s) = \int_{\mathbf{x}' \in \mathbb{D}^{\text{s}}} \frac{1}{4\pi|\mathbf{x} - \mathbf{x}'|^2} \left[\mathbf{n} \times \hat{\mathbf{K}}^{\text{ext}}(\mathbf{x}', s)\right] \mathrm{d}V, \tag{D.12}$$

where

$$\mathbf{n} = \frac{\mathbf{x} - \mathbf{x}'}{|\mathbf{x} - \mathbf{x}'|}$$

is a unit vector pointing in the $\mathbf{x} - \mathbf{x}'$ direction.

Now to compute the mutual impedance between the transmitting and receiving loop antenna, we need the vectors $\hat{\mathbf{e}}_s^{\text{bg}}$ and $\hat{\mathbf{e}}_r^{\text{bg}}$. To obtain the former, we model the small transmitting loop antenna by a magnetic dipole as

$$\mathbf{K}^{\text{ext}}(\mathbf{x}, s) = s\mu_0 A \hat{I}_s^{\text{bg}}(s) \delta(\mathbf{x} - \mathbf{x}_s) \boldsymbol{\nu}_s,$$

where A is the area of the loop and $\mathbf{x}_s$ is the position vector of the center of the loop. Substitution of this expression in Eq. (D.12) gives

$$\hat{\mathbf{E}}^{[0]}(\mathbf{x}, s) = \hat{\mathbf{e}}_s^{\text{bg}} \hat{I}_s^{\text{bg}},$$

where

$$\hat{\mathbf{e}}_s^{\text{bg}} = s\mu_0 A \frac{1}{4\pi|\mathbf{x} - \mathbf{x}_s|^2} \mathbf{n}_s \times \boldsymbol{\nu}_s \quad \text{and} \quad \mathbf{n}_s = \frac{\mathbf{x} - \mathbf{x}_s}{|\mathbf{x} - \mathbf{x}_s|}.$$

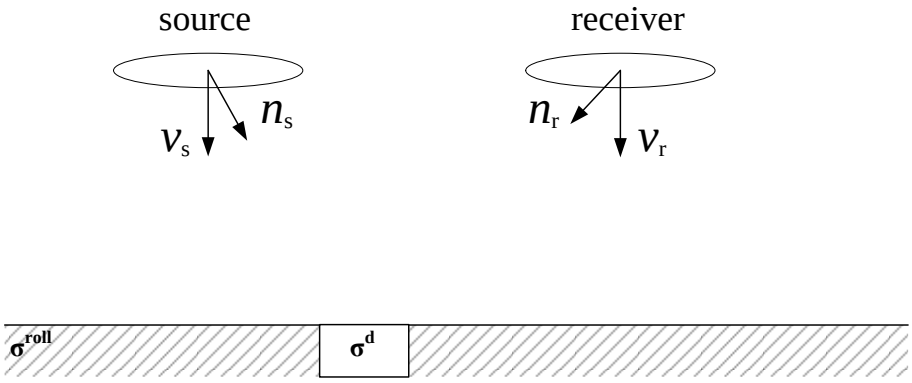

Figure D.2: Two antennas above a roll. The unit vectors $\boldsymbol{\nu}_{\mathrm{n}}$ and $\mathbf{n}_{\mathrm{n}}$ are shown as well. The former is a unit vector orthogonal to the surface of the loop, the latter is a unit vector pointing towards the defect.

Similarly, to obtain $\hat{\mathbf{e}}_r^{\mathrm{bg}}$, we take

$$\mathbf{K}^{\mathrm{ext}}(\mathbf{x}, s) = s\mu_0 A \hat{I}_r^{\mathrm{bg}}(s)\delta(\mathbf{x} - \mathbf{x}_r)\boldsymbol{\nu}_r,$$

where $\mathbf{x}_r$ is the center of the receiving antenna. The corresponding field is found as

$$\hat{\mathbf{E}}^{[0]}(\mathbf{x}, s) = \hat{\mathbf{e}}_r^{\mathrm{bg}} \hat{I}_r^{\mathrm{bg}},$$

where

$$\hat{\mathbf{e}}_r^{\mathrm{bg}} = s\mu_0 A \frac{1}{4\pi|\mathbf{x} - \mathbf{x}_r|^2} \mathbf{n}_r \times \boldsymbol{\nu}_r \quad \text{and} \quad \mathbf{n}_r = \frac{\mathbf{x} - \mathbf{x}_r}{|\mathbf{x} - \mathbf{x}_r|}.$$

All unit vectors used in the above derivation are shown in Figure D.2.

Substituting the expressions for $\hat{\mathbf{e}}_s^{\mathrm{bg}}$ and $\hat{\mathbf{e}}_r^{\mathrm{bg}}$ in Eq. (D.1) gives

$$\delta\hat{Z} = -(s\mu_0 A)^2 \int_{\mathbf{x}\in\mathbb{D}^d} \frac{\delta\sigma}{16\pi^2|\mathbf{x} - \mathbf{x}_r|^2|\mathbf{x} - \mathbf{x}_s|^2} (\mathbf{n}_r \times \boldsymbol{\nu}_r) \cdot (\mathbf{n}_s \times \boldsymbol{\nu}_s)\, \mathrm{d}V \quad \text{(D.13)}$$

and using the rule

$$(\mathbf{a} \times \mathbf{b}) \cdot (\mathbf{c} \times \mathbf{d}) = (\mathbf{a} \cdot \mathbf{c})(\mathbf{b} \cdot \mathbf{d}) - (\mathbf{a} \cdot \mathbf{d})(\mathbf{b} \cdot \mathbf{c})$$

we can also write the change in the impedance as

$$\delta\hat{Z} =$$
$$-(s\mu_0 A)^2 \int_{\mathbf{x}\in\mathbb{D}^d} \frac{\delta\sigma}{16\pi^2|\mathbf{x} - \mathbf{x}_r|^2|\mathbf{x} - \mathbf{x}_s|^2} \left[(\mathbf{n}_s \cdot \mathbf{n}_r)(\boldsymbol{\nu}_s \cdot \boldsymbol{\nu}_r) - (\mathbf{n}_s \cdot \boldsymbol{\nu}_r)(\boldsymbol{\nu}_s \cdot \mathbf{n}_r)\right] \mathrm{d}V.$$

Finally, if we operate in steady-state at an angular frequency ω ($s = -i\omega$) the above formula becomes

$$\delta\hat{Z} =$$
$$(\omega\mu_0 A)^2 \int_{\mathbf{x}\in\mathbb{D}^d} \frac{\delta\sigma}{16\pi^2|\mathbf{x} - \mathbf{x}_r|^2|\mathbf{x} - \mathbf{x}_s|^2} \left[(\mathbf{n}_s \cdot \mathbf{n}_r)(\boldsymbol{\nu}_s \cdot \boldsymbol{\nu}_r) - (\mathbf{n}_s \cdot \boldsymbol{\nu}_r)(\boldsymbol{\nu}_s \cdot \mathbf{n}_r)\right] \mathrm{d}V.$$

Bibliography

[1] N.V. Budko, "Electromagnetic Radiation, Scattering and Imaging", Class notes for Electromagnetics, Delft University of Technology, 2004

[2] J. Bladel, *Electromagnetic Fields*, 2nd ed. Wiley-IEEE Press, 2007

[3] C.A. Balanis , "Loop antennas," in *Antenna Theory: Analysis and Design*, 3th ed. New Jersey: Wiley and Sons, 2005, pp. 237

[4] H. Ward, G.W. Hohmann, "Electromagnetic Theory for Geophysical Applications," in *Electromagnetic Methods in Applied Geophysics*, Vol 1, no. 3, Society of Exploration Geophysicists, Oklahoma, 2008, ch. 4

[5] J. Tang, A.K. Tieu, Z. Jiang. "Modelling of the Development of Initial Crack under Hot Rolling condition," in *Materials Science Forum,* vols.505-507, pp. 1291-1296, Jan. 2006

[6] J.G. Lenard, "Flat Rolling - A general Discussion," in *Primer on Flat Rolling*, 1st ed., London: Elsevier, 2007

[7] J.T. Davis, B.P. Charles. "Multi frequency eddy current test apparatus with intermediate frequency processing." U.S. Patent, No. 4,467,281. 21 Aug. 1984.

[8] U. Hanoglu, Seminar, Topic: "Mathematical and Physical Modeling of the Flat Rolling Process," University of Nova Gorica, Slovenia, Sept. 24, 2009

[9] J.E. Burke, D. Turnbull. "Recrystallization and grain growth," in *Progress in Metal Physics*, vol. 3, pp. 220-244, 1952

[10] Krautkramer Australia, "Principles of Eddy Current Testing" http://www.krautkramer.com.au/Hocking/Wall%20Chart.pdf, 2005 [Jun. 20, 2013]

[11] Eddy Current Technology Incorporated, "Conductivity of Metals Sorted By Resistivity," http://eddy-current.com/conductivity-of-metals-sorted-by-resistivity/, May 17, 2013 [May 25, 2013]

[12] J.M. Louritioz et al. *Photonic Crystals: Towards Nanoscale Photonic Devices*, Springer, 2005, pp. 121

[13] J.M. Buckley, Hocking NDT. "An introduction to Eddy Current Testing theory and technology," in *technical paper eddyc. pdf available from the internet at http://joe.buckley.net/papers*, Vol. 8, pp. 8, Sept. 2003

[14] H.L. Libby, *Introduction to electromagnetic nondestructive test methods* Wiley and Sons, New York, 1971

[15] C. Dodd, CV, W.E. Deeds. "Analytical Solutions to Eddy-Current Probe-Coil Problems." *Journal of applied physics*, vol. 39, pp. 2829-2838, 1968

[16] C. Dodd, W.E. Deeds. "Induction coils coaxial with an arbitrary number of cylindrical conductors." *Journal of applied physics*, vol. 45, pp. 638, 1974

[17] J.R. Bowler, S.A. Jenkins, L.D. Sabbagh and H.A. Sabbagh, "Eddycurrent probe impedance due to a volumetric flaw," *Journal of applied physics*, vol. 70, no. 5, pp. 1107-1114, Aug 1991.

[18] J.R. Bowler, "Eddycurrent interaction with an ideal crack. I. The forward problem," *Journal of applied physics*, vol.75, no.12, pp.8128,8137, Jun 1994

[19] J. Pavo, K. Miya, "Reconstruction of crack shape by optimization using eddy current field measurement," *IEEE Transactions on Magnetics*, vol.30, no.5, pp.3407-3410, Sep 1994

[20] G. Birnbaum, G.M. Free, "Investigation into the Depth of Pulsed Eddy-Current Penetration," in *Eddy-current Characterization of Materials and Structures: A Symposium* ASTM International, 1981, pp. 374

[21] J. blitz, T.S. Peat "The application of multifrequency eddy current to testing ferromagnetic metals," *NDT International,* vol. 14, pp.15-17, 1981

[22] A. Sophian, G.Y. Tian, D. Taylor, J. Rudlin, "A feature extraction technique based on principal component analysis for pulsed Eddy current NDT," *NDT & E International* vol. 36, no. 1, pp. 37-41, Jan 2003

[23] S.M. Berg, "Modeling and inversion of Pulsed Eddy Current Data," University of Technology Delft, Netherlands, Dec 2003

[24] K.W.A. Dongen, "A directional borehole radar system for subsurface imaging," University of Technology Delft, Netherlands, Jun 2002

[25] E. vd Elzen, "Inhoudelijk eindverslag VENDT Wervelstroomonderzoek," Lismar Engineering, Ouderkerk aan de Amstel, Netherlands, Jun 2011

[26] E. vd Elzen, "Handleiding VENDT Wervelstroominstrument" Lismar Engineering, Ouderkerk aan de Amstel, Netherlands, Jul 2011

[27] A.T De Hoop, "Chapter 28: Electromagnetic reciprocity theorems and their applications," in *Handbook of Radiation and Scattering of Waves*, 1th ed. London: Academic Press, 1995, pp. 807

[28] A.T De Hoop, "Chapter 30: Interference and shielding of electromagnetic systems accessible via low-frequency terminations. ElectroMagnetic Compatibility (EMC)," in *Handbook of Radiation and Scattering of Waves*, 1th ed. London: Academic Press, 1995, pp. 943

[29] M.D. Verweij, P.M. van den Berg, H. Blok, "One-dimensional Electromagnetic Waves," in *Electromagnetic Waves: An Introductory Course* 2nd ed. DUP Blue Print, 2001, pp. 59

[30] L.D. Landau, E.M. Lifshitz, "Methods of solving problems in electrostatics," in *Electrodynamics of Continuous Media, Volume 8 of Course of Theoretical Physics* 2nd ed. Pergamon Press, 1963, pp. 9

[31] L.A. Apresyan, D.V. Vlasov, "On the Depolarization Factors for Anisotropic Ellipsoids in Anisotropic Media," *arXiv preprint, Cornell University Library* Mar 2013

[32] C.F. Bohren, D.R. Huffman, "Chapter 5: Particles Small Compared with the Wavelength" in *Absorption and Scattering of Light by Small Particles* Wiley-VCH Verlag GmbH, 2007, pp. 130-157

[33] L.W. Couch , *Digital and Analog Communication Systems*, 7th ed. New Jersey: Pearson Prentice Hall, 2007

[34] B. Helifa, A. Oulhadj, A. Benbelghit, I.K. Lefkaier, F. Boubenider, D. Boutassouna, "Detection and measurement of surface cracks in ferromagnetic materials using eddy current testing," *NDT & E International* Vol 39, Issue 5, July 2006, pp. 384-390

[35] S.T. Sijher, A.K. Ahmed, "Antenna modeling by infinitesimal dipoles using genetic algorithms." *Progress In Electromagnetics Research* Vol 52 2005 pp. 225-254.

[36] F.E. Neumann, "Allgemeine Gesetze der inducirten elektrischen Strme," Abhandlungen der Kniglichen Akademie der Wissenschaften zu Berlin, 1845 pp. 187